CRL INTERNAL REPORT SERIES - NO. CRL 92

RESEARCH AND EVALUATION OF THE PERFORMANCE OF DIGITAL MODULATIONS IN SATELLITE COMMUNICATIONS SYSTEMS

by

S.B. Kesler and D.P. Taylor

COMMUNICATIONS RESEARCH LABORATORY

FACULTY OF ENGINEERING

McMASTER UNIVERSITY

HAMILTON, ONTARIO, CANADA

Checked 11

CRL INTERNAL REPORT SERIES - NO. CRL 92

(2)

RESEARCH AND EVALUATION OF THE PERFORMANCE OF DIGITAL MODULATIONS IN SATELLITE COMMUNICATIONS SYSTEMS

by

(1)

S.B. Kesler and D.P. Taylor

October 1981

This is the final report on DSS Contract No. 06SV.36001-0-3193 Serial No. 0SV80-00038 performed on behalf of the Communications Research Centre, Department of Communications.

Communications Research Laboratory
Faculty of Engineering
McMaster University
Hamilton, Ontario, Canada, L8S 4L7

CONTENTS

1. INTRODUCTION

1.1 General

This study concerns the performance evaluation of various digital modulations in satellite communications systems. The satellite channel consists of the cascade combination of up-link filters, an amplifying transponder and down-link filters. Also there is additive thermal noise on both the up-link and down-link. At high bit-rates both the up-link and down-link filters, as well as pulse shaping filters (PSF) in the transmitter and receiver cause time spreading of the signal resulting in intersymbol interference (ISI) which causes a corresponding degradation in system performance. In addition, the transmitter output high-power amplifier (HPA), and the satellite transponder, which in most cases are travelling-wave tube (TWT) amplifiers, are nonlinear devices causing both amplitude compression or limiting of signals, and incidental phase modulation as a function of the input amplitude (AM/PM conversion). These nonlinear effects can lead to significant signal distortion and a corresponding degradation in system performance.

Further causes of system impairment are different sources of interference. In addition to the intersymbol interference (ISI), mentioned above, cochannel interference (CCI) and adjacent channel interference (ACI) effects cause degradations in system performance. Inaccuracies in carrier phase and symbol timing recovery for coherent modulation systems are further sources of performance degradation.

The objective of this study is to analyze by means of simulation the performance of various modulation systems taking into account as many of the above effects as possible. In particular, the following effects are included:

(a) Intersymbol interference (ISI) due to time-spreading of filter responses.

(b) Additive thermal noise.

(c) Nonlinear effects (amplitude compression and AM/PM conversion) of:

(1) the TWT transponder in satellite,

(2) the transmitter output HPA.

(d) Effects of the pulse shaping filters (PSF) each consisting of a cascade combination of:

(1) Nyquist cosine rolloff filter,

(2) x/sin (x) aperture equalizer, and

(3) group delay equalizer.

(e) Cochannel interference (CCI)

(f) Adjacent channel interference (ACI)

(g) Carrier recovery and symbol timing inaccuracies.

The effects of (a), (b) and (c1) have been analyzed in previous work [1-3] by the authors. The present study consists essentially of the extension of this work, which includes more detailed analysis of these and the remaining effects on satellite channel performance.

In recent years, considerable effort has been devoted to analytically evaluating the combined effects of Gaussian noise and interference on digitally modulated signals [4-6]. In most of these cases, however, this analytical work has beeen confined to the case where the transmission channel may be represented as a combination of linear filters, and no attempt has been made to consider any nonlinear effects in the channel.

Because of the mathematical difficulties encountered in analyzing nonlinear channels, little analytical work has been done, and what has been done has considered only simple limiter-type channels [7,8] which do not take into account AM/PM conversion effects. Because of this, the study of satellite channels and their effects has been by means of computer simulation [9-14]. Most of these simulations have been limited in scope in that they have considered either a small number of modulation types, or have dealt with only a limited number of the above mentioned effects.

The subject of the present study is to develop a general purpose computer simulation program for evaluating the performance of a wide range of digital modulation systems on satellite channels. The previous simulation package [1] is to be extended to include as many effects as possible in order to provide a useful tool for assessing and predicting the expected performance of digital modulations on satellite and radio channels.

1.2 Overall Description of the System Being Simulated

In the study described in this report, we have employed digital computer simulation to evaluate system performance degradation due to pulse shaping with Nyquist cosine rolloff filter with all-pass delay equalizer, nonlinear effects of HPA characteristics, cochannel (CCI) and adjacent channel (ACI) interferences, and inaccuracies in carrier and symbol timing recovery. The evaluation is performed for the digital modulation schemes listed below:

(1) coherent 2-phase PSK (2-CPSK)

(2) coherent 4-phase PSK (4-CPSK)

(3) coherent 8-phase PSK (8-CPSK)

(4) coherent 2-phase PSK, differentially encoded

(5) coherent 4-phase PSK, differentially encoded

(6) coherent 8-phase PSK, differentially encoded

(7) differential 2-phase PSK (2-DPSK)

(8) offset PSK (OPSK)

(9) fast FSK (FFSK)

In this study a unified approach has been taken which facilitates performance comparisons of different modulation types under a wide class of operating conditions.

High-frequency signals can, in all cases of interest, be investigated using pre-envelope functions of the form

$$s(t) = u(t)e^{j\omega_c t} = [x(t) + jy(t)]e^{j\omega_c t} \tag{1.1}$$

The actual transmitted signal is then just the real part of s(t):

$$\mathrm{Re}\{s(t)\} = x(t)\cos\omega_c t - y(t)\sin\omega_c t \tag{1.2}$$

where ω_c is the angular carrier frequency. The information to be transmitted is entirely contained in the real baseband signals x(t) and y(t), and thus, with no loss of generality, the modulation systems under study may be investigated by means of the complex baseband signals x(t) + jy(t). This is a basic philosophy behind our simulation which is carried out entirely in complex baseband form. The baseband signals x(t) and y(t) are referred to as in-phase and quadrature signals, respectively.

A general block diagram of the system being simulated is shown in

Figure 1.1. The main portions of the signal path are modelled in complex baseband form. They include transmitter PSF, nonlinear HPA, transmit (including uplink) filter, nonlinear satellite transponder (TWT), receive (including downlink) filter, and receiver PSF. These portions of the simulation program are written as a self-contained set of subroutines, and are used in simulating all of the various modulation schemes.

In order to simulate digital data sources, long repetitive pseudo-noise (PN) sequences of length 2047 were used. In order to study the effects of ISI, all possible patterns of consecutive transmitted digits should be present with equal frequency. In practice, of course, this requirement depends directly on the group-delay characteristics of the filters in the channel. We found it sufficient to ensure only equal representation of all possible singlet, doublet, and triplet patterns of digits.

The signal generation portion of the program converts the input PN sequences into the quadrature baseband signals $x(t)$ and $y(t)$ according to the desired modulation law. Fast Fourier transform techniques are used to convert the complex baseband signal $x(t) + jy(t)$ to the frequency domain form $X(f) + jY(f)$. Filtering is performed by multiplying $X(f) + jY(f)$ by the complex baseband transfer function of the transmitter PSF. This time-frequency-time conversion is performed whenever a filter is encountered in the signal path.

The time-domain output of the PSF is processed by the nonlinear HPA, which may be represented as the combination of two nonlinear effects, namely,

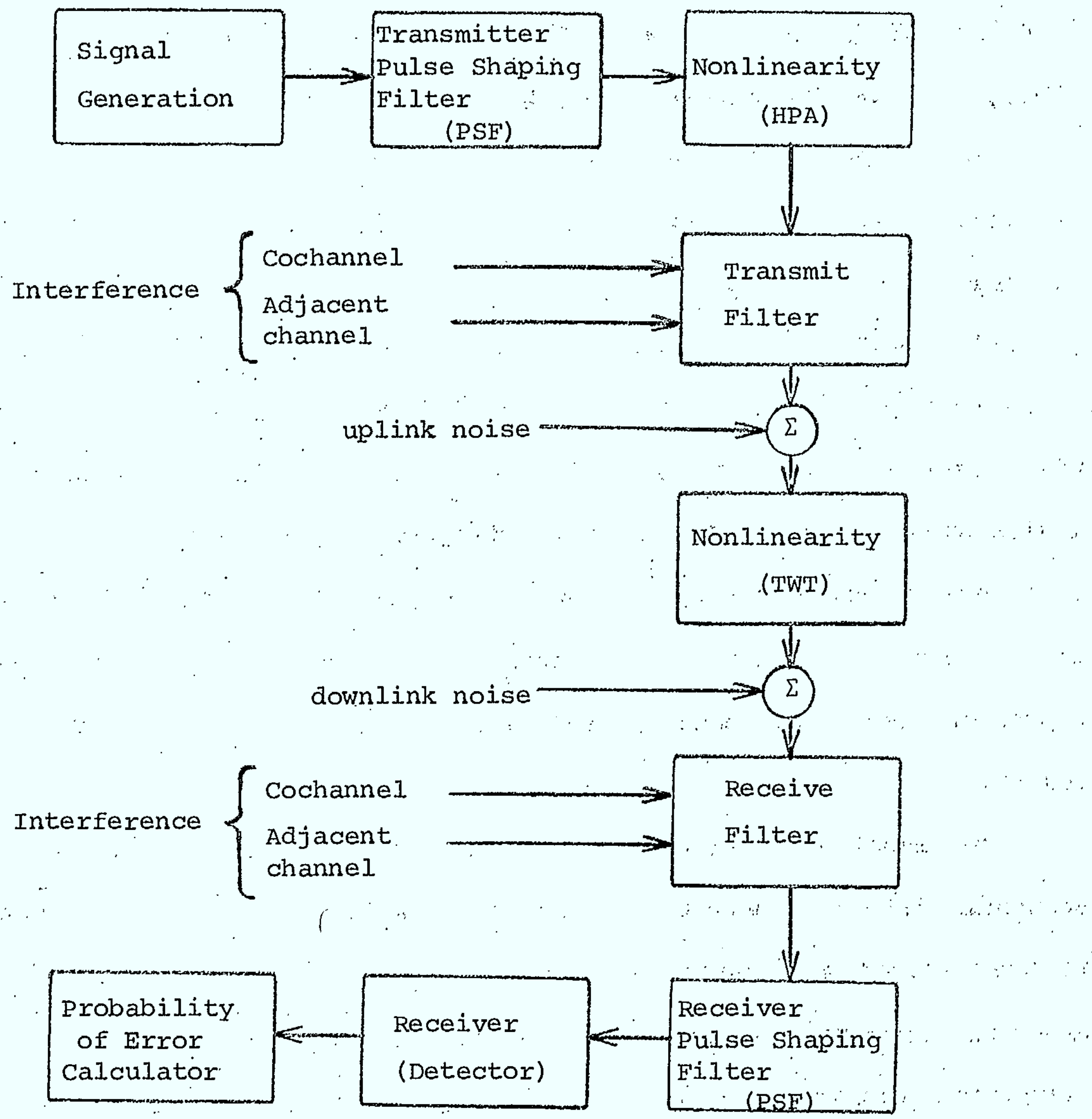

Fig. 1.1 Basic block diagram of system simulation.

(a) an amplitude compression or soft-limiting effect often referred to as AM/AM conversion.

(b) a nonlinear amplitude-dependent phase-shift often referred to as AM/PM conversion.

For simulation, the HPA is modelled in quadrature form, combining AM/AM and AM/PM. The output signal is then obtained by piecewise curve fitting.

After processing by the HPA, the signal is transformed to the frequency-domain and passed through the transmit filter. The time-domain output of this filter is processed by a nonlinear satellite TWT transponder in a similar manner to that described above for the HPA. Receiver filtering and PSF is then performed as discussed above, and the time-domain version of the signal is passed through the receiver.

The receiver portion of the simulation is modulation-dependent and the separate option is provided for each type of modulation. The quadrature components of the received signal are demodulated and the energy of each received symbol is evaluated.

Rather than actually simulating the downlink additive noise, we may account for its effect by computing the noise power at the output of the receiver PSF, where in this case we assume white additive Gaussian noise at the input of the downlink filter. The calculated noise power is then used in conjunction with the received symbol energy to calculate the probability of error for each symbol. The uplink noise cannot be handled in this way since it is passing through the nonlinear transponder. Simulating of uplink noise samples is not performed in this study because of limitations on computer time. The average of calculated probabilities of error over the entire transmitted symbol sequence then forms our estimate of error probability for the given simulated system.

This probability of error is the basic measure of performance which we use in comparing the various modulation schemes. Other measures of performance, namely the signal power spectra and eye diagrams may also be used and are particularly useful in making comparisons of different systems.

Inclusion of the effects of pulse shaping filters, cochannel and adjacent channel interferences, as well as synchronization errors is optional, so that each of these effects can be included either separately or in conjunction with any other effect. Such a program configuration is highly versatile, enabling various modes of system analysis.

2. REVIEW OF VARIOUS MODULATION SCHEMES

We now present a brief review of the modulation schemes analyzed in this study. A much more detailed review can be found in some classical texts, e.g. [15-17].

2.1 Coherent Phase-Shift Keying (CPSK)

At high transmission rates phase-shift keying (PSK) techniques are the most widely used of all digital modulation methods. This is so because they are efficient from the point of view of

(a) conservation of bandwidth

(b) the possibilities of using very simple techniques for transmission and reception.

As a result, the use of PSK techniques has been widely studied. We begin by reviewing CPSK for the additive noise channel [15-17]. These results, which in many cases can be expressed in closed form serve as bounds on PSK performance over more complex channels.

For the additive noise channel there is no interference between signals in adjacent bauds and we may consider reception in a single baud interval without reference to any other. For an M-ary PSK system, where $M=2^L$, $L=1,2,\ldots$, the transmitted signal in any baud, say the zeroth, may be written in the form

$$s_i(t) = \begin{cases} \sqrt{\dfrac{2E_s}{T}}\, g(t)\cos(\omega_c t + \phi_i), & 0 \leq t \leq T \\ 0, \text{ elsewhere} \end{cases} \qquad i = 1,2,\ldots,M \tag{2.1}$$

where

E_s is the signal energy

$g(t)$ is a unit energy pulse, which in the additive noise case may be conveniently taken to be rectangular,

ω_c is the carrier frequency which is assumed to be a fixed multiple of $2\pi/T$ where T^{-1} is the baud rate,

ϕ_i is the transmitted phase and has one of the values $2\pi i/M$, $i=1,2,\ldots,M$.

Assuming the i-th symbol or phase has been transmitted, the received signal may be written as

$$x(t) = s(t) + n(t), \quad i=1,2,\ldots,M \tag{2.2}$$

where $n(t)$ is narrowband additive white Gaussian noise which may be written as

$$n(t) = n_1(t)\cos\omega_c t + n_2(t)\sin\omega_c t \tag{2.3}$$

and

$$E\{n^2(t)\} = E\{n_1^2(t)\} = E\{n_2^2(t)\} = N_0$$

$$E\{n_1(t) \circ n_2(t)\} = 0. \tag{2.4}$$

The received signal may then be written as

$$x(t) = \sqrt{\frac{2E_s}{T}}\, g(t)\cos(\omega_c t + \phi_i) + n_1(t)\cos\omega_c t + n_2(t)\sin\omega_c t, \quad i=1,2,\ldots,M. \tag{2.5}$$

Assuming as usual that ϕ_i is equally likely to have any one of the M possible values $2\pi i/M$, $i=1,2,\ldots,M$, demodulation is readily accomplished by forming the quantities:

$$X = \sqrt{\frac{2}{T}} \int_0^T x(t) \cos\omega_c t \, dt$$

$$Y = \sqrt{\frac{2}{T}} \int_0^T x(t) \sin\omega_c t \, dt \qquad (2.6)$$

which are then sampled and passed at time T to a decision device or slicer which makes a decision on which value of ϕ_i has been transmitted. A block diagram of this receiver is shown in Fig. 2.1.

The decision variables X and Y may readily be written as

$$X = \sqrt{E_s} \cos\phi_i + \eta_1,$$

$$Y = -\sqrt{E_s} \sin\phi_i + \eta_2, \qquad i=1,2,...M, \qquad (2.7)$$

where

$$\eta_1 = \frac{1}{\sqrt{2T}} \int_0^T n_1(t) \, dt$$

$$\eta_2 = \frac{1}{\sqrt{2T}} \int_0^T n_2(t) \, dt \qquad (2.8)$$

X and Y may be shown to be uncorrelated and Gaussian with means $\sqrt{E_s}\cos\phi_i$ and $\sqrt{E_s}\sin\phi_i$, respectively, and common variance $N_o/2$. Their joint probability density function may be written as

$$p(X,Y) = \frac{1}{\pi N_o} \exp[-\frac{(X-\sqrt{E_s}\cos\phi_i)^2}{N_o} - \frac{(Y-\sqrt{E_s}\sin\phi_i)^2}{N_o}] \qquad (2.9)$$

and, by making the transformations

$$X = r\sqrt{N_o} \cos\theta, \qquad Y = r\sqrt{N_o} \sin\theta \qquad (2.10)$$

it may be written in polar form as

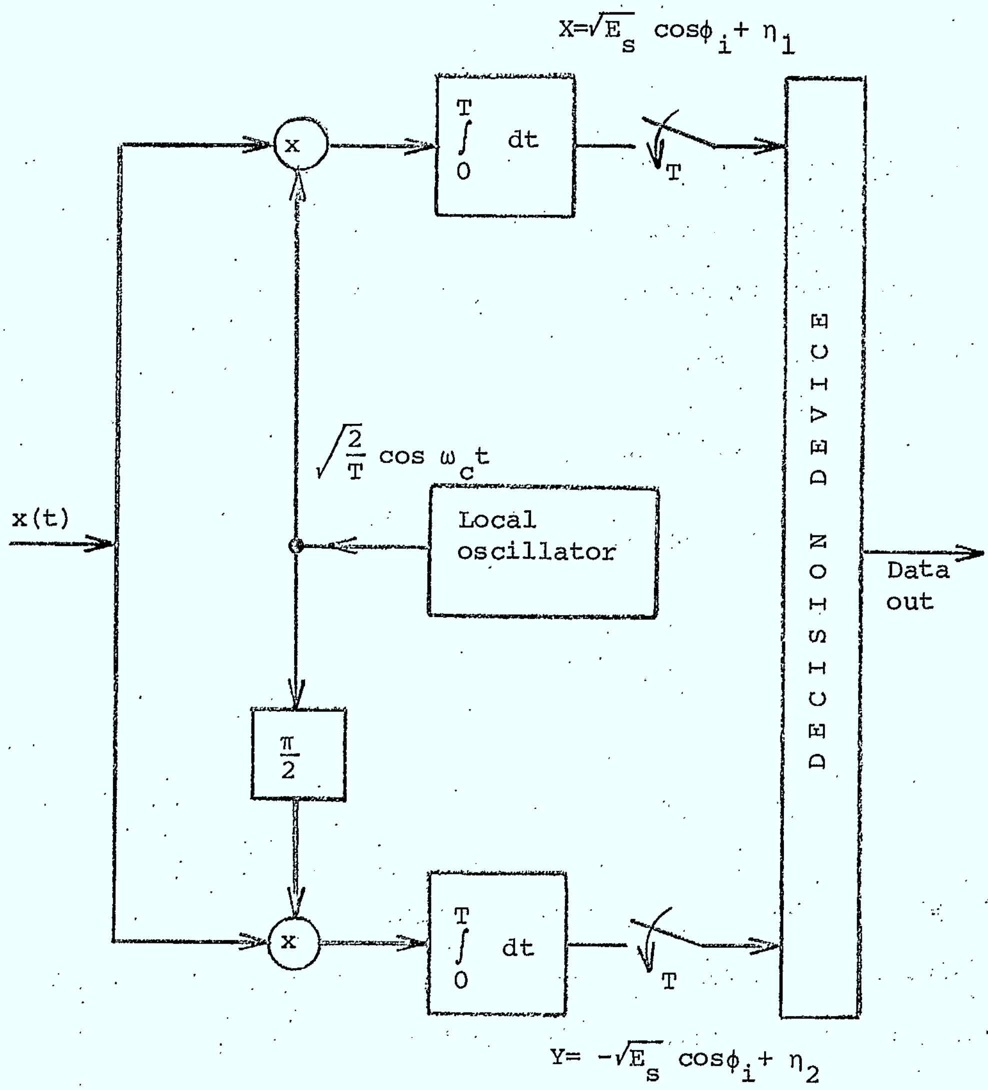

Fig. 2.1 Block diagram of basic CPSK receiver.

$$p(r,\theta) = \frac{r}{\pi} \exp\{-[r^2-2r\sqrt{\frac{E_s}{N_o}}\cos(\theta-\phi_i) + \frac{E_s}{N_o}]\} ,$$

$$i=1,2,\ldots,M. \qquad (2.11)$$

Now the probability of symbol error $P_e(M)$ for an M-ary CPSK system may be seen to be 1 minus the probability that the received signal point with coordinates (X,Y) or (r,θ) lies in the region

$$0 \leq r < \infty$$

$$-\frac{2\pi i}{M} - \frac{\pi}{M} \leq \theta < -\frac{2\pi i}{M} + \frac{\pi}{M} \qquad (2.12)$$

For equally likely symbols this probability is independent of i and may be written as

$$P_e(M) = 1 - \int_{-\pi/M}^{\pi/M} p(\theta)\, d\theta = 1 - \int_0^{\infty} \int_{-\pi/M}^{\pi/M} p(r,\theta) d\theta\, dr. \qquad (2.13)$$

Using (2.11), Eq. (2.13) can be written as

$$P_e(M) = 1 - \frac{2}{\pi} \int_0^{\infty} e^{-(u-\rho)^2} [\int_0^{u\tan(\pi/M)} e^{-v^2} dv] du \qquad (2.14)$$

where $\rho=\sqrt{E_x/N_o}$. In the case of binary symbols (M=2) this reduces to the well known result

$$P_e(2) = \frac{1}{2} [1 - \mathrm{erf}(\sqrt{\frac{E_s}{N_o}})] = \frac{1}{2} \mathrm{erfc}(\sqrt{\frac{E_s}{N_o}}) \qquad (2.15)$$

where erfc(x) = 1-erf(x) is the complementary error function, and for quaternary symbols (M=4), we obtain the result

$$P_e(4) = \frac{3}{4} - \frac{1}{2}\,\mathrm{erf}\left(\sqrt{\frac{E_s}{N_o}}\right) - \frac{1}{4}\,\mathrm{erf}^2\left(\sqrt{\frac{E_s}{N_o}}\right). \qquad (2.16)$$

For higher values of M, it is not possible to evaluate Eq. (2.14) in closed form.

The above rather simple results for CPSK systems unfortunately represent the situation only when the channel is the idealized additive noise channel of Fig. 2.1. In any real system, however, interference due to filter effects and to the presence of other signals is likely to be the major source of performance degradation. The interference due to filter effects is known as intersymbol interference, that due to other signals falling into the same frequency band as the desired signal is known as cochannel interference, and that due to partial overlapping of the neighbouring channels frequency bands is known as adjacent channel interference.

In order to evaluate these interference effects numerous analyses have been carried out. The problem of evaluating system performance in a combination of ISI and additive Gaussian noise has been considered in [5,18-20]. In [5,18,19] bounds are derived on the probability of error. In [20], Shimbo et al., carry out one exact analysis, which although complicated, gives excellent results.

The effects of a combination of ISI, CCI and additive noise on system performance have been analyzed in [4,6]. Also, the works presented in [6,10] dealt to some extent with the ACI effects. In this report we present some computer simulation results on the combined effects of ISI, CCI, ACI and additive noise.

Coherent phase-shift-keyed systems can be implemented by encoding input data either coherently or differentially. We shall now briefly outline a general detection procedure for both types of modulations.

2.1.1 Coherently Encoded CPSK

Consider the DECISION DEVICE block in Fig. 2.1. Its inputs in the l-th transmitted baud are X and Y. The estimate $\hat{\phi}$ of the transmitted phase is first computed as

$$\hat{\phi} = -\tan^{-1}\frac{Y}{X} \tag{2.17}$$

and then subtracted from each of the possible phases $\phi_i = 2\pi i/M$ $i=1,2,\ldots,M$. The absolute values of the differences are then compared and the decision is made that the particular ϕ_i was transmitted for which $|\phi_i-\hat{\phi}|$ is minimum. The block diagram of the decision devise for coherently encoded M-ary CPSK is given in Fig. 2.2(a). Probability of error is computed by using formulas (2.14) to (2.16).

2.1.2 Differentially Encoded CPSK

When the signal is differentially encoded at the transmitter, it is the phase difference between the adjacent symbols that contains the desired information. Coherent detection of such a signal is presented in Fig. 2.2(b). The estimate $\hat{\phi}_\ell$ of the phase of the ℓ-th transmitted baud is processed in the same way as in 2.2(a), until the estimate ϕ_i^ℓ is obtained. This estimate is then subtracted modulo 2π from the corresponding estimate obtained from the previous, $(\ell-1)$th, baud and the difference $\hat{\phi}_i$ is taken as an estimate of the transmitted ℓth baud.

For this type of M-ary CPSK, the probability of error can be readily shown to be [15]

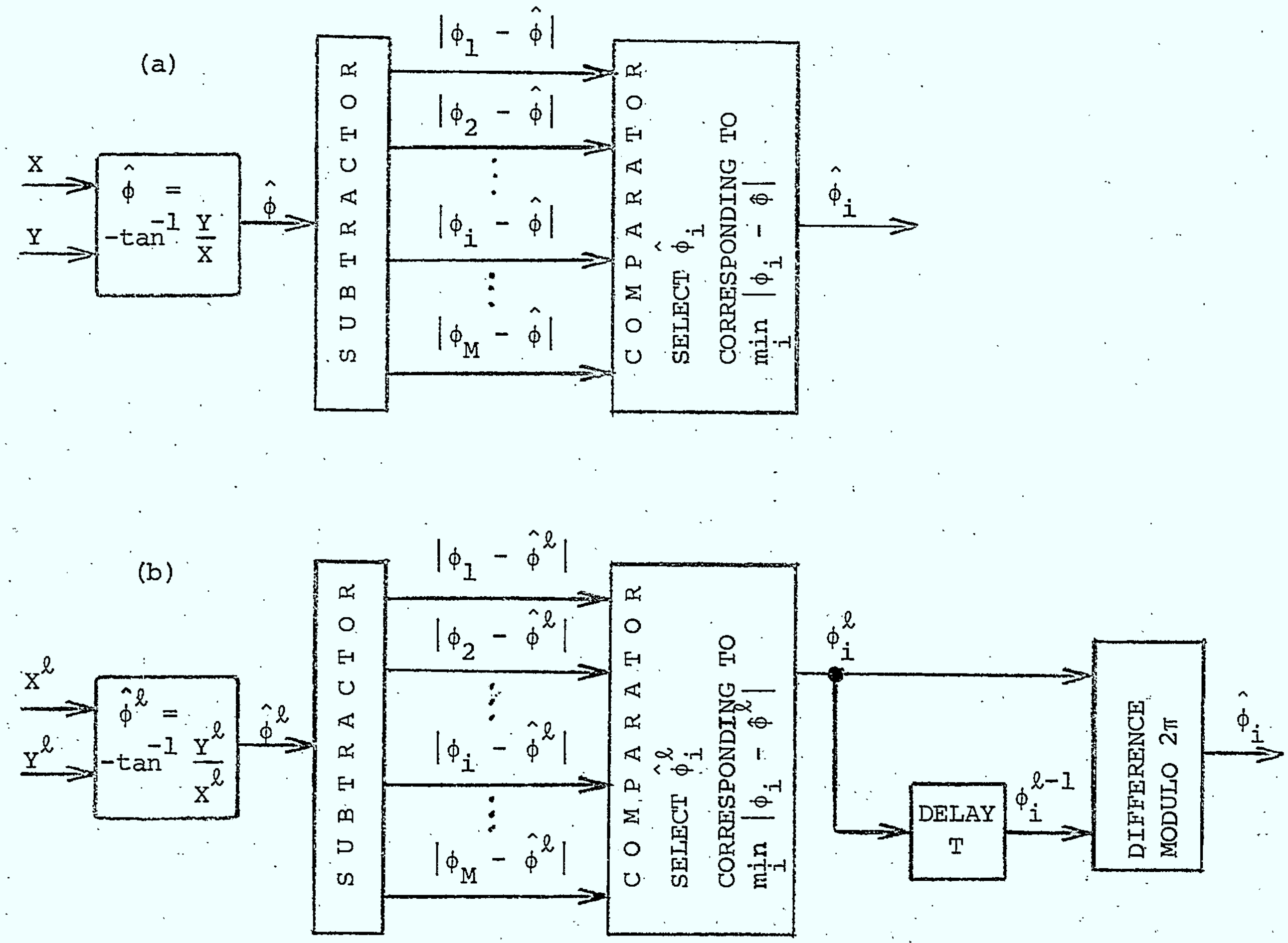

Fig. 2.2 (a) Coherent detection of coherently encoded CPSK,
(b) Coherent detection of differentially encoded CPSK.

$$P_e = 2P'_e - P'^2_e \tag{2.18}$$

where P'_e is the corresponding probability of error for the coherently encoded CPSK.

The case of differentially coherent detection of differentially encoded CPSK (usually referred to as Differential Phase-Shift-Keying or DPSK) is reviewed in the next section.

2.2 Differential Phase-Shift-Keying (DPSK)

One way to avoid the necessity of providing a phase-coherent local oscillator at the CPSK receiver is to perform a differentially coherent detection of differentially encoded CPSK. A block diagram of the detector of such a DPSK system is shown in Fig. 2.3. The phase difference is estimated directly rather than by estimating previous and current absolute phases. A decision procedure is then applied to obtain the correct transmitted phase. This way, the possible ambiguity in the transmitted absolute phase is eliminated.

The performance analysis of DPSK system is in general considerably more complex than that of CPSK system. This occurs because we must evaluate the statistics of the phase changes across two baud intervals.

A fairly detailed analysis is presented in the previous report [1] and references quoted therein, and we will not repeated it here. We only give the result for the probability of error which is used in the actual simulation.

If Ψ is the displacement (due to ISI) of the phase differential

$$\Delta\theta = \theta_2 - \theta_1 \tag{2.19}$$

obtained by taking the difference between two successive symbol phases

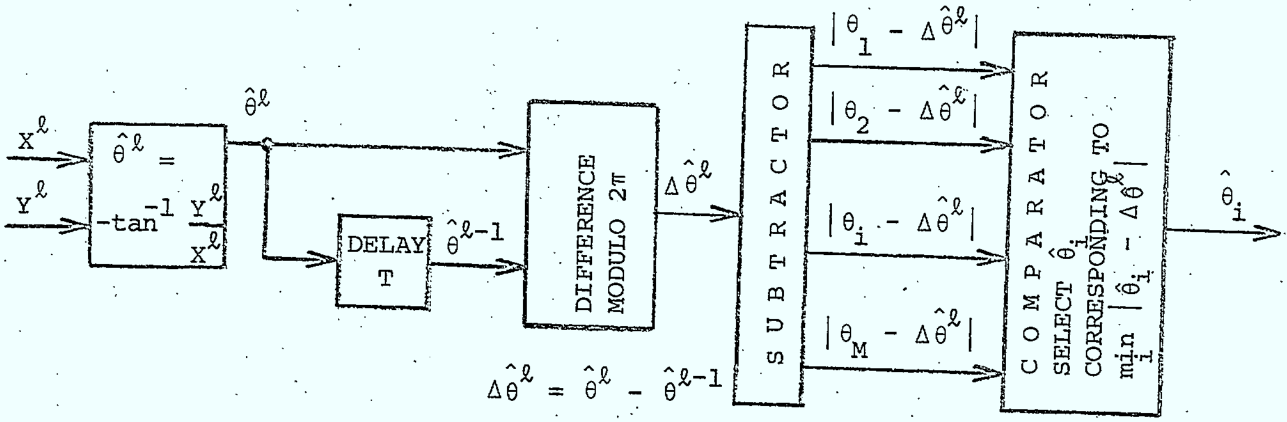

Fig. 2.3 Block diagram of a DPSK detector.

θ_1 and θ_2, the correct decision region boundaries will be $-\frac{\pi}{M} - \Psi$ and $\frac{\pi}{M} - \Psi$. The probability of error will then be given by

$$P_e = 1 - \int_{-\frac{\pi}{M}-\Psi}^{\frac{\pi}{M}-\Psi} P(\Delta\theta)\, d(\Delta\theta) \tag{2.20}$$

where $P(\Delta\theta)$ is the probability density function of the phase differential, and is given by

$$p(\Delta\theta) = \int_{-\pi}^{\pi} \left[\frac{\exp(-\rho_1)}{2\pi} + \frac{\sqrt{\rho_1}}{\pi} \cos\theta \exp(-\rho_1 \sin^2\theta) \operatorname{erfc}(-\sqrt{\rho_1}\cos\theta)\right] x$$

$$x\left[\frac{\exp(-\rho_2)}{2\pi} + \frac{\sqrt{\rho_2}}{\pi} \cos(\theta+\Delta\theta) \exp(-\rho_2 \sin^2(\theta+\Delta\theta)) \operatorname{erfc}(-\sqrt{\rho_2}\cos(\theta+\Delta\theta))\right]\} \, d\theta. \tag{2.21}$$

where

$$\rho_1 = A_1^2/2\sigma^2$$
$$\rho_2 = A_2^2/2\sigma^2 \tag{2.22}$$

and σ^2 is noise power while A_1 and A_2 are the amplitudes of the adjacent received symbols s_1 and s_2.

In our simulation we are primarily interested in the performance analysis of 2-phase DPSK, although the program provides the option for the analysis of 4-phase DPSK as well.

2.3 Offset Phase-Shift Keying (OPSK)

In the OPSK a binary sequence is split into two parts. By feeding alternate (even and odd) bits into the I and Q channels respectively, one obtains the OPSK signal. The OPSK signal is similar to a 4-phase CPSK signal, but phase transitions of 180° are eliminated. This tends to reduce the signal spectrum spread and ISI. A pair of PN sequences is generated by a shift register array to represent the signal information, in exactly the same manner as for 4-phase CPSK. The Q-channel sequence is then shifted by half a symbol (16 complex samples) to the left to form an offset-PSK sequence. This way there is no simultaneous transition in both channels, and no phase transitions greater then 90° will result in the modulated signal. The resulting I and Q signals have their bit transitions staggered in time by $\frac{1}{2}$ a symbol period or baud.

2.4 Fast Frequency-Shift Keying (FFSK)

Normally, FSK systems are different from PSK systems and their simulation cannot be carried out in the same manner. However, the FFSK, having a frequency deviation index $h = 0.5$, is a special case. It employs coherent phase detection. Except for the actual pulse shape, the baseband signal is very similar to that of the OPSK.

It was shown in [1] that the I and Q components of the FFSK baseband signal can be writted as

$$x(t) = A\cos(\pm \frac{\pi t}{2T}) \qquad 0 \leq t \leq T \qquad (2.23)$$

$$y(t) = A\sin(\pm \frac{\pi t}{2T}) \qquad 0 \leq t \leq T \qquad (2.24)$$

where T is the symbol duration, and signs are chosen according to the values of dibits or pairs of data bits.

As can be seen, the I and Q components of the baseband signal, $x(t)$ and $y(t)$ are of half cosine (sine) shape as opposed to the rectangular shapes of the M-ary CPSK waves. As in the OPSK case, there are no phase transitions greater than 90°. In fact, for FFSK it can be shown that 90° phase transitions occur linearly in time over the duration of a bit.

3. CHANNEL CHARACTERISTICS

The channel consists of both transmit and receive filters as well as any nonlinear devices present in the signal path. It is simulated in identical manner in all cases. For convenience of presentation we include in this section the treatment of the ground station or transmit HPA nonlinearity, transmiter and receiver PSF's, CCI and ACI. Again, the simulation of all these effects (except for the ACI) are identical for all modulation schemes.

Due to channel nonlinearities, signals passing through them must be simulated in baseband time-domain. Filtering of signals, however, is performed in the baseband frequency-domain using the discrete Fourier transform (DFT). The filter transfer functions must be sampled in the frequency-domain. We present below a brief review of the DFT.

3.1 Discrete Fourier Transform (DFT)

If a continuous time function g(t) is sampled at intervals $n\Delta T$, $n=0,1,\ldots,N-1$, over a finite time interval $T = N\Delta T$, the discrete Fourier transform of the sampled data function $g(n\Delta T)$ is defined by

$$G(k\Delta f) = \sum_{n=0}^{N-1} g(n\Delta T)e^{-j2\pi nk/N}, \quad k=0,1,\ldots N-1 \qquad (3.1)$$

and the inverse transform (IDFT) is defined by

$$g(n\Delta T) = \frac{1}{N}\sum_{k=0}^{N-1} G(k\Delta f)e^{j2\pi nk/N}, \quad n=0,1,\ldots,N-1 \qquad (3.2)$$

In the above equations Δf is the frequency sampling interval, related to the time sampling interval Δt by

$$N \cdot \Delta t \cdot \Delta f = 1, \tag{3.3}$$

and the frequency band occupied by one period of $G(k\Delta f)$ is

$$f_B = N\Delta f = \frac{1}{\Delta t} . \tag{3.4}$$

The quantity f_B is termed the "simulation bandwidth" in the preceding work [1], and the criteria for determining it, are described there. In the present simulation, this and related parameters are specified in a slightly different manner, so that the comparative analysis is somewhat more general than in the previous case. This was enabled by the use of a computer with much larger memory than in the case of the original simulation presented in [1].

In our simulation, the number of complex samples per symbol is fixed to a value of LSAMPL = 32, which is sufficient for an accurate detection in all modulation schemes. The number of time/frequency complex samples for the use in the discrete Fourier transformation is selected to be N = 4096. (N is designated NH in the simulation program.) With the values of LSAMPL and N thus specified, the simulation bandwidth exceeds the filters' 3dB bandwidths by at least ten times in all cases considered.

Another advantage of a wide simulation bandwidth is that it is possible to specify a BT-product, without explicitly specifying its "components", i.e. the filter bandwidth and symbol rate. Thus by selecting the BT to be, say, 1.2 we imply that the filter 3dB bandwidth in Hertz is 20 percent larger than the symbol rate in symbols/second. In this way, the comparison of different modulation systems can be made more general.

3.2 Equivalent Baseband Representation

Consider a modulated signal

$$s(t) = A(t) \cos[\omega_c t + \phi(t)] \tag{3.5}$$

where ω_c is the angular carrier frequency, and A(t) and/or $\phi(t)$ contain the modulating information. Equation (3.5) can be expanded to give

$$s(t) = x(t)\cos\omega_c t - y(t)\sin\omega_c t \tag{3.6}$$

where

$$x(t) = A(t) \cos\phi(t) \tag{3.7a}$$

$$y(t) = A(t) \sin\phi(t) \tag{3.7b}$$

Next, consider the pre-envelope function

$$s'(t) = u(t)e^{j\omega_c t} \tag{3.8}$$

where u(t) is the complex baseband function

$$u(t) = x(t) + jy(t) \tag{3.9}$$

and x(t) and y(t) are low-pass functions defined as in Eq. (3.7). It is clear from Eqs. (3.6) to (3.9) that

$$s(t) = \text{Re}\{s'(t)\}. \tag{3.10}$$

It is well known that the analysis or simulation of bandpass communications systems can be carried out in equivalent baseband. Thus, in the simulation of the modulated signals, the complex baseband function u(t) is actually simulated, and all bandpass filter characteristics are translated to baseband in the same manner and are represented by equivalent complex low-pass filters centered at zero frequency. The product of the DFT of the complex baseband signal u(t) and the filter transfer function will give the filter output in the frequency-domain. In order to pass signals through a nonlinear device, the output of each filter is inverse transformed back to the time-domain.

3.3 Channel Nonlinearities

Amplification of signals in satellite channels is performed using nonlinear, active microwave devices, usually travelling-wave tubes (TWT). They are characterized by two types of distortion of signals passing through them. First, we have amplitude compression, termed the AM/AM conversion and second, there is amplitude dependent phase shift, usually referred to as AM/PM conversion. Both output AM/AM and AM/PM conversion characteristics of any particular TWT are provided by the manufacturer. For example, the AM/AM and AM/PM characteristics of the INTELSAT IV TWT Hughes 261-H is shown in Figure 3.1a.

To incorporate the TWT characteristics into a baseband simulation model we need to convert them into quadrature output characteristics which preserve the quadrature components of the signal after it is passed through the TWT nonlinearity. If we denote the AM/AM and AM/PM characteristics in Fig. 3.1a as $R(v)$ and $\theta(v)$, respectively, the output in-phase, $p'(v)$, and quadrature, $q'(v)$, characteristics are given by

$$p'(v) = R(v) \cos[\theta(v)] \tag{3.11}$$

$$q'(v) = R(v) \sin[\theta(v)]. \tag{3.12}$$

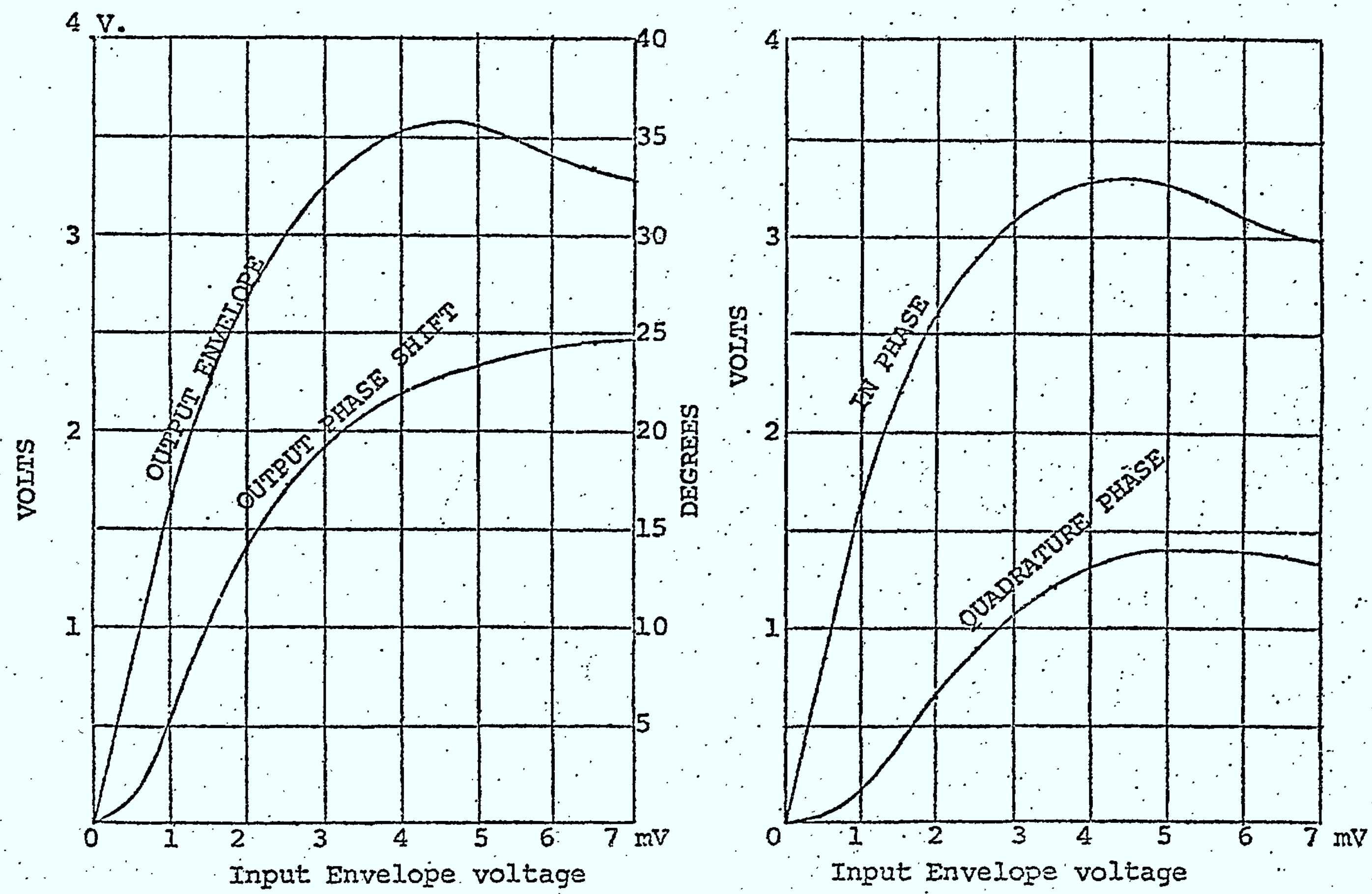

(a) Output envelope and phase shift/ Input envelope curves

(b) Quadrature representation of curves in (a)

Figure 3.1 Single carrier transfer characteristics of a Hughes 261-H TWT.

They are shown in Fig. 3.1b as functions of the input voltage v.

Let the input signal to a TWT be represented by (Eq. 3.5)

$$v_i'(t) = A(t)\cos(\omega_c t + \phi(t)) = \mathrm{Re}\{[x(t) + jy(t)]e^{j\omega_c t}\} \tag{3.13}$$

where A(t) and $\phi(t)$ are the envelope and phase functions, respectively, and x(t) and y(t) are the real and imaginary parts, respectively, of the complex baseband function u(t), as given by Eq. (3.7). Since the TWT is a nonlinear device, the output signal contain harmonics of the fundamental frequency. However, the bandpass characteristics of the TWT and the filters following it will remove these higher frequency components from the output. Therefore, only the component of the TWT output signal centered at the carrier frequency ω_c needs to be considered.

The output signal of the TWT, after band-pass filtering, may be represented by

$$v_o'(t) = R[A(t)]\cos\{\omega_c t + \Theta[A(t)] + \phi(t)\} \tag{3.14}$$

where R[•] and Θ[•] are the AM/AM and AM/PM characteristics of the TWT. Since the simulation is performed at baseband we need a complex baseband equivalent of Eq. (3.14). Expanding (3.14) we obtain

$$\begin{aligned} v_o'(t) &= \{R(A)\cos[\Theta(A)]\cos\phi - R(A)\sin[\Theta(A)]\sin\phi\}\cos\omega_c t \\ &\quad - \{R(A)\sin[\Theta(A)]\cos\phi + R(A)\cos[\Theta(A)]\sin\phi\}\sin\omega_c t \end{aligned} \tag{3.15}$$

where the dependence on time has been omitted for simplicity. From Eq. (3.15) the complex baseband output signal is readily identified as

$$v_o(t) = \{R(A)\cos[\theta(A)]\cos\phi - R(A)\sin[\theta(A)]\sin\phi\}$$

$$+ j\{R(A)\sin[\theta(A)]\cos\phi + R(A)\cos[\theta(A)]\sin\phi\} \qquad (3.16)$$

Multiplying Eq. (3.13) by A(t) and dividing by A(t), the output complex baseband signal of the TWT can be written in normalized form as

$$v_o(t) = [p(t)x(t) - q(t)y(t)] + j[q(t)x(t) + p(t)y(t)] \qquad (3.14)$$

where p(t) and q(t) are normalized quantities p'(t) and q'(t) of Eqs. (3.11) and (3.12) and are given by

$$p(t) = \frac{p'(t)}{A(t)} = \frac{R[A(t)\cos\{\theta[A(t)]\}}{A(t)} \qquad (3.15)$$

$$q(t) = \frac{q'(t)}{A(t)} = \frac{R[A(t)]\sin\{\theta[A(t)]\}}{A(t)} \qquad (3.16)$$

and, from Eq. (3.7)

$$A^2(t) = x^2(t) + y^2(t) \qquad (3.17)$$

One way to compute the output of the TWT for a given input is to use a quadrature model of the nonlinearity as developed by Eric [21]. This model was used in a previous study. However, in this study, we use a simple interpolation of data points on the transfer characteristics. This method is somewhat more general, since the in-phase and quadrature nonlinearities in Fig. 3.1b can be obtained directly from available TWT characteristics as in Fig. 3.1a. On the other hand, to obtain a polynomial representation of the nonlinearities as required for the method presented in [21], an additional computation is required.

3.3.1 Travelling-Wave Satellite Transponder (TWT)

In our simulation, we used the same parameters for the TWT transponder as in the original report [1]. The tube used is an INTELSAT IV Hughes 261-H TWT. The transfer characteristics, shown in Fig. 3.1 are segmented into 7 parts and the interpolation between points is performed by a piecewise cubic fit. Values between 0 and 1 are obtained by a quadratic fit. If some other tube is considered, then all that is needed is to replace the particular tube parameters in the program.

3.3.2 High-Power Output Amplifier (HPA)

The simulation of the high-power transmitter output amplifier is performed in exactly the same way as that of the satellite transponder. The only difference is the type of TWT used. It is Varian helix TWT-VTC 6660 C2 Ser. 106 HPA whose characteristics are shown in Fig. 3.2. Since this tube's AM/PM characteristic varies more with input voltage than the Hughes 261-H's does, we segmented the transfer characteristics into 13 parts. Of course, this can also be easily changed if desired.

In our analysis we refer to the satellite transponder as the TWT although both transponder and the high-power amplifiers are travelling-wave tubes. This is done to keep the notation of the original study as much the same as possible. Consequently, we chose to refer to the transmit amplifier tube as the HPA.

3.4 Pulse Shaping Filter (PSK)

In the original work [1], all filtering operations are lumped into one uplink and one downlink filter. A Chebyshev filter of order four was used as an approximation to a cascade of the transmitter pulse

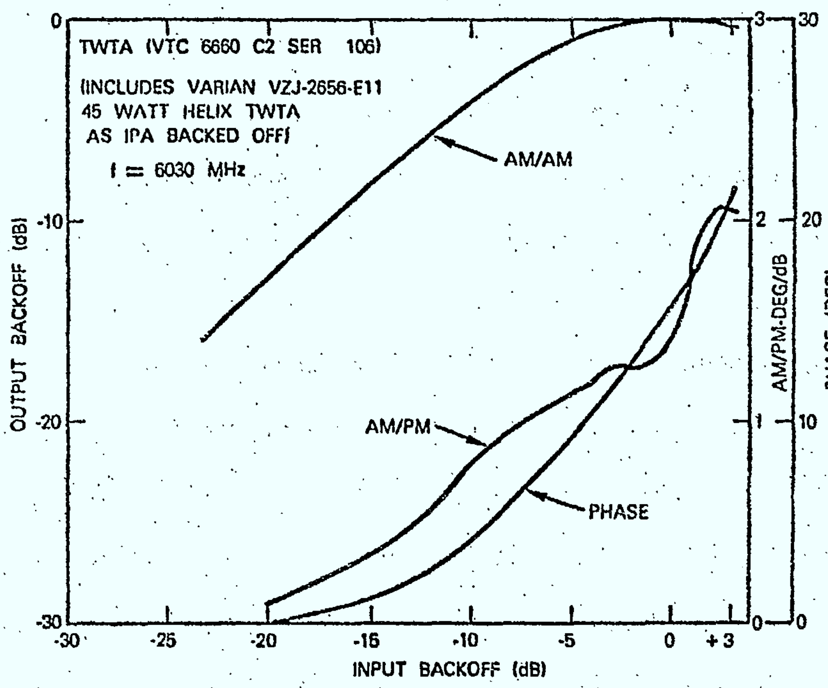

Fig. 3.2 Single carrier transfer characteristics of a HPA used in simulation.

shaping filter and the transponder band-pass filter before the nonlinearity. The same filter was used in the downlink path.

With the inclusion of an HPA nonlinearity, however, filtering actions in transmitter and transponder have to be separated. A fourth order Chebyshev filter is still used in the uplink (and downlink) path, between the HPA and the TWT transponder, while the transmitter (and receiver) pulse shaping filters were selected to be of the Nyquist cosine rolloff type. This filter has been extensively used in both hardware and computer simulations [13,22] of the satellite channel. Since a Nyquist filter is not physically realizable, we have approximated it by a fourth order Butterworth characteristic. At frequencies where the attenuations of the two filters are less than 30 dB, the responses differ by less than 1 dB. The details of the approximation are given in section 3.4.1.

To compensate for the sin (x)/x spectral shape of the rectangular transmitted pulses, an x/sin (x) type compensation is cascaded with the pulse shaping filter. After some analysis, it was found that this aperture equalizer characteristic is well-approximated by a two-pole resonant circuit.

Large variations of the group delay of the above described filters within the passband are compensated or equalized by an all-pass network. Since the inclusion of the x/sin (x) aperture equalizer in the simulation is optional, independent all-pass networks were designed for the case where the Butterworth filter only is used, and for the case when the latter is cascaded with an equalizer.

In what follows, we present the design of the pulse shaping filter components.

3.4.1 Nyquist Cosine Rolloff Filter

A Nyquist filter is an optimal pulse shaping filter in the presence of intersymbol interference (ISI), as demonstrated in [23]. The family of transfer functions, parameterized by a cosine rolloff factor α is given by

$$H_N'(\omega) = \begin{cases} T, & 0 \leq \omega \leq \frac{\pi}{T}(1-\alpha) \\ \frac{T}{2}\left[1 - \sin\left(\frac{\omega T-\pi}{2\alpha}\right)\right], & \frac{\pi}{T}(1-\alpha) \leq \omega \leq \frac{\pi}{T}(1+\alpha) \\ 0, & \text{elsewhere} \end{cases} \tag{3.18}$$

where T is the symbol interval. The cosine rolloff factor has value between 0 and 1. For $\alpha=0$ we have an ideal low-pass filter with one sided bandwidth equal to π/T. At the other limit, $\alpha=1$, the transfer function extends to $\omega=2\pi/T$. Transfer functions of the Nyquist filter for $\alpha=0$, 0.5, and 1 are shown in Fig. 3.3.

The normalized transfer function expressed in dB is given by

$$H_N(\omega_n)\ [\mathrm{dB}] = 20 \log \frac{H_N'(\omega_n)}{T}$$

$$= \begin{cases} 0, & -\frac{\pi}{\alpha} \leq \omega_n \leq -\pi \\ -6 + 20\log(1-\sin\frac{\omega_n}{2}), & -\pi \leq \omega_n \leq \pi \\ -\infty, & \text{elsewhere} \end{cases} \tag{3.19}$$

where

$$\omega_n = \frac{\omega T-\pi}{\alpha} \tag{3.20}$$

Figure 3.4 shows $H_N(\omega_n)$ in the range $\pi/20 \leq \omega_n \leq \pi$. Since the slope in the stopband is not constant, we determine the slope of the approximating Butterworth filter so as to fit the slope of the Nyquist filter at a sufficiently high value of attenuation, for example, the frequency

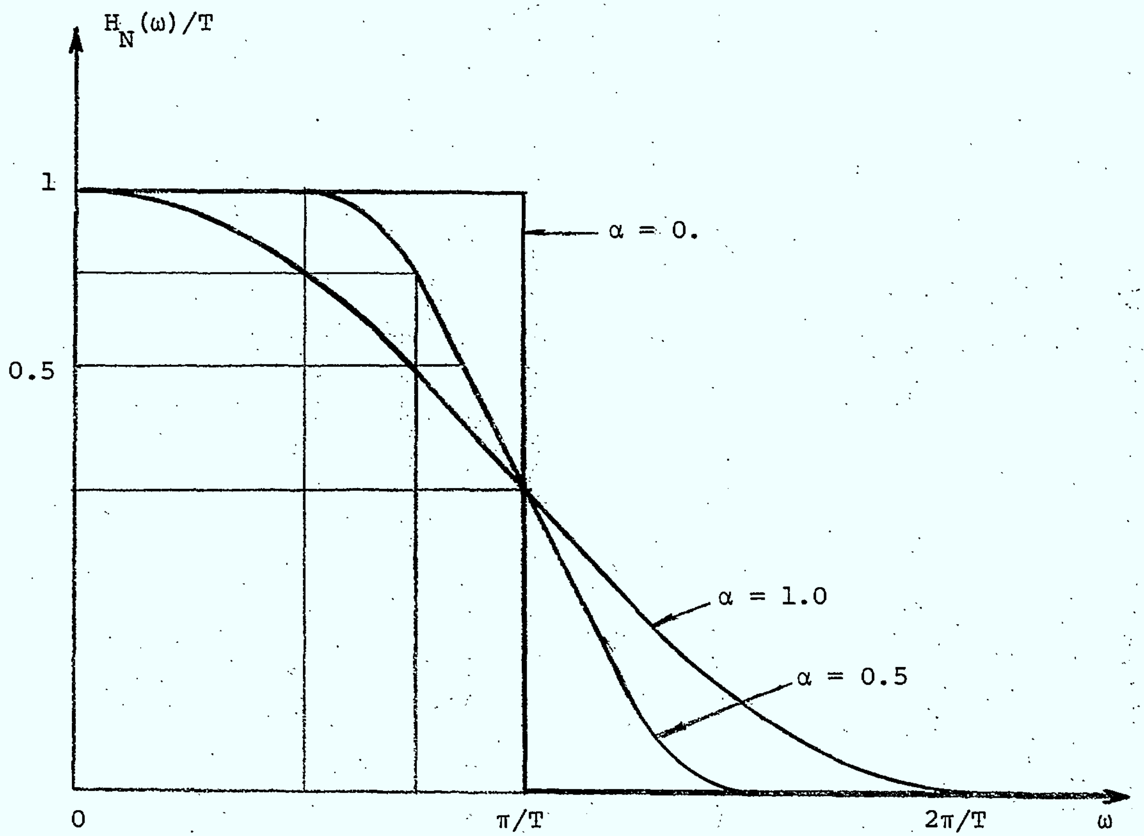

Fig 3.3 Transfer function of the Nyquist cosine rolloff filter for three values of rolloff factor α.

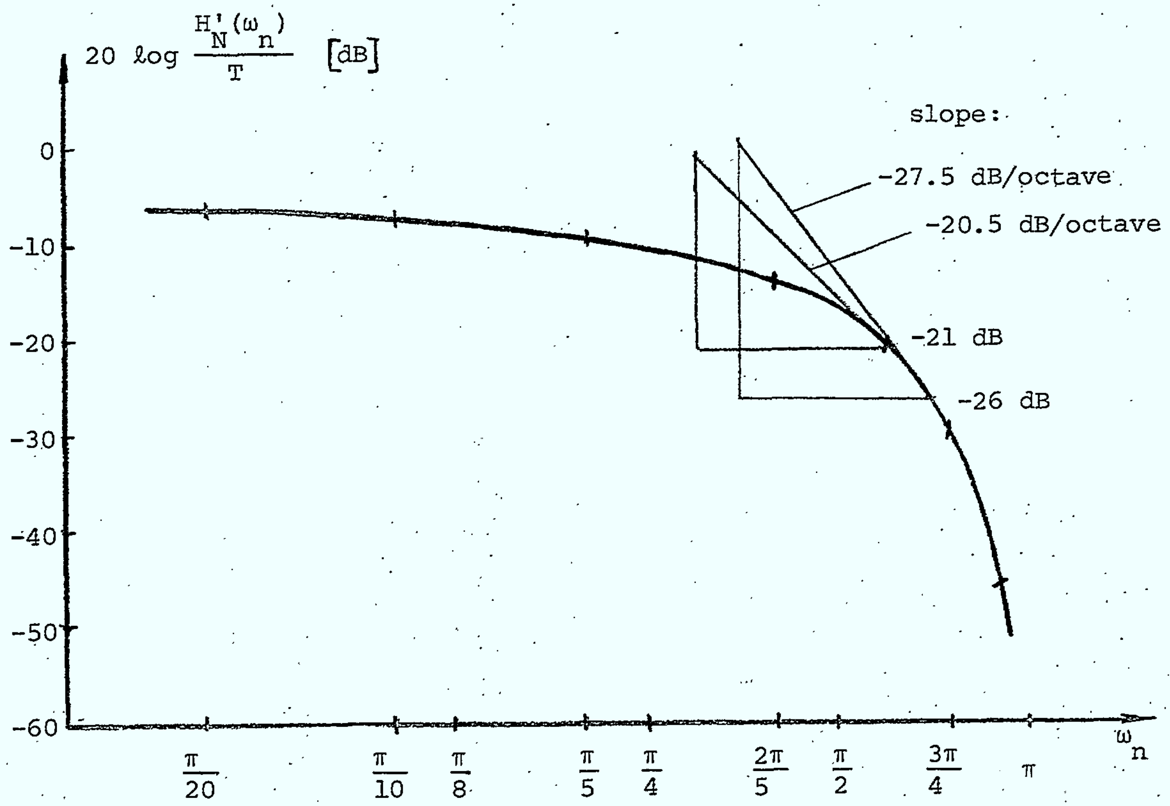

Fig. 3.4 Transfer function (in dB) of the normalized Nyquist cosine rolloff filter.

where the transfer function of the Nyquist filter is down to, say, 20 dB below the passband level. At that point ($\omega_{nc} \approx 7\pi/10$) the slope of the Nyquist characteristics is about 27.5 dB/octave as can be seen in Fig. 3.4. We thus select the Butterworth filter of fourth order (yielding the slope of $6n = 24$ dB/octave) to best fit the Nyquist filter. The out of band slope of the Butterworth filter will be larger than that of the Nyqist filter for all $\omega_n < \omega_{nc}$.

Once the order of the fitting Butterworth filter is determined we need to specify its absolute frequency scaling so that it can be simulated. The 3 dB frequency ω_{3bn} will be chosen so as to match the normalized 3 dB frequency of the cosine rolloff filter ω_{3rn}, which is given by

$$\frac{T}{2}\left(1 - \sin \frac{\omega_{3rn}}{2}\right) = \frac{T}{\sqrt{2}} \tag{3.21}$$

Solving Eq. (3.21) for ω_{3rn}, we get

$$\omega_{3rn} = 2 \sin^{-1}(1 - \sqrt{2}) = -0.854 = -0.272\ \pi \tag{3.22}$$

Using Eqs. (3.20) and (3.22) we find the unnormalized 3 dB frequency of the cosine rolloff filter as

$$\omega_{3r} = (1 - 0.272\ \alpha)\pi/T \tag{3.23}$$

By equating ω_{3b} with the value given by Eq. (3.23) we normalize the scaling of the fitting Butterworth filter in a way that its 3 dB frequency always matches the 3 dB frequency of the cosine rolloff factor for any chosen value of rolloff factor α.

3.4.2 The x/sin (x) Equalizer

The Nyquist filters described in the foregoing are designed to provide optimal performance for data transmission under the assumption that their input signals consist of a weighted train of impulses. The purpose then of the x/sin (x) aperture equalizer is to compensate with the filter passband for the rectangular pulse shapes of the actual transmitted signals, in such a way as to make them appear as impulse inputs to the shaping filters. In practice, this equalizer is easily realized as a second order resonant circuit with its resonant frequency chosen to be approximately located at the first zero of the transmitted signal spectrum.

The amplitude response and pole-zero pattern are shown in Fig. 3.5a and b. The poles are given by

$$p_{e\ 1,2} = -\rho \cos \theta \pm j\rho \sin \theta \tag{3.24}$$

The transfer function is given by

$$H_e(s) = \frac{K}{(s-p_1)(s-p_2)} = \frac{K}{s^2 + s2\rho\cos\theta + \rho^2} \tag{3.25}$$

We select $K=\rho^2$ so that $H_e(0)=1$. The squared magnitude response at $s=j\omega$ is given by

$$|H_e(j\omega)|^2 = \frac{\rho^4}{|-\omega^2 + j\omega 2\rho \cos\theta + \rho^2|^2} = \frac{\rho^4}{(\rho^2-\omega^2)^2 + 4\omega^2\rho^2\cos^2\theta}$$

$$= \frac{\rho^4}{\omega^4 + 2\omega^2\rho^2\cos(2\theta) + \rho^4} = \frac{N}{D(\omega^2)} \tag{3.26}$$

the resonant frequency, ω_e, is that at which $|H_e(j\omega)|^2$ is maximum, or equivalently, where $D(\omega^2)$ is minimum. Thus, we have the extremity

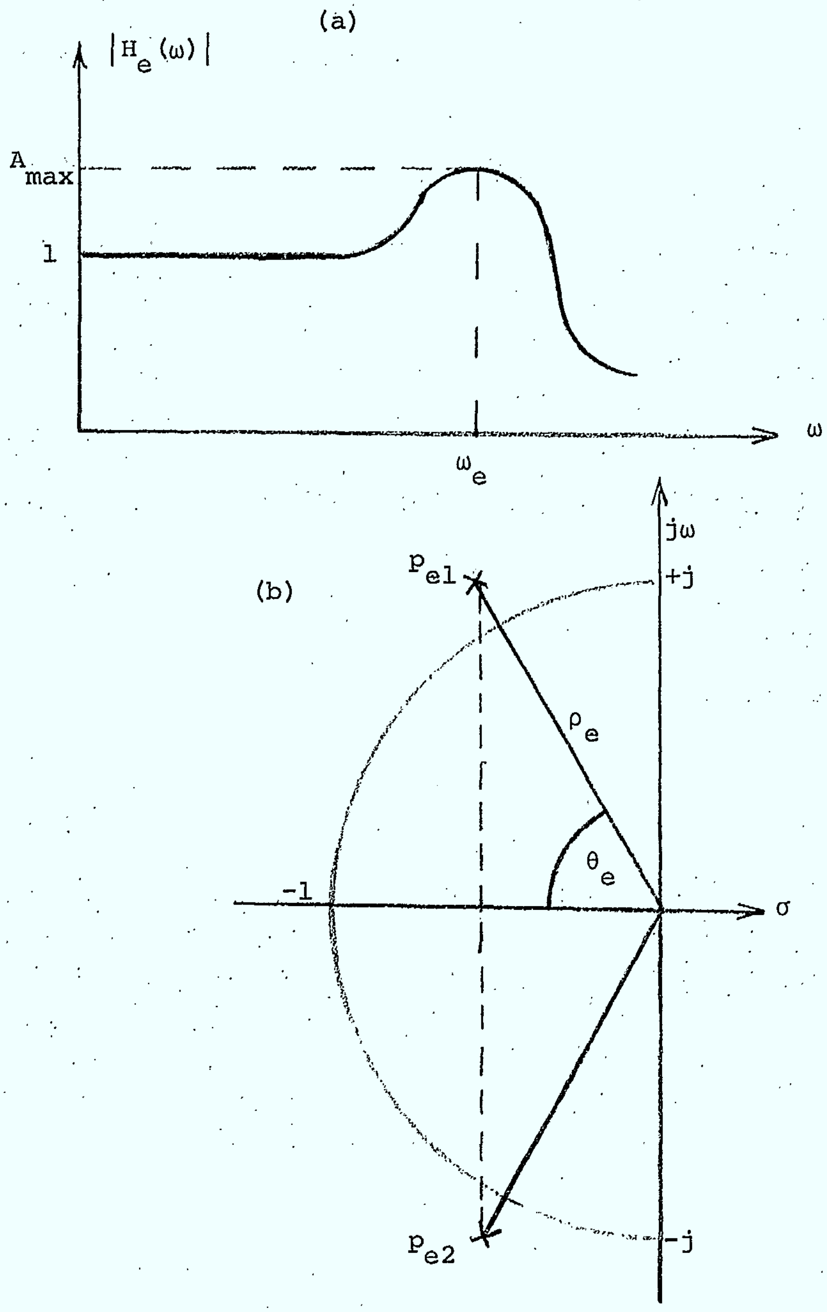

Fig. 3.5 Two-pole resonant circuit;
(a) amplitude response,
(b) pole-zero pattern.

condition

$$\frac{dD(\omega^2)}{d(\omega^2)} = 2\omega_e^2 + 2\rho_e^2\cos(2\theta_e) = 0 \tag{3.27}$$

which yields

$$\omega_e^2 = -\rho_e^2 \cos(2\theta_e) \tag{3.28}$$

or

$$\omega_e = \rho_e\sqrt{-\cos(2\theta_e)} \tag{3.29}$$

In order for ω_e to be real, we have that $\cos(2\theta_e) \leq 0$ which, together with the stability condition (all poles in the left half-plane) gives the allowable range for θ_e, $45^\circ \leq \theta_e \leq 90^\circ$.

Inserting Eq. (3.28) into (3.26) we have for the peak value, A_{max}^2, of the squared magnitude response

$$A_{max}^2 = |H_e(j\omega_e)|^2$$

$$= \frac{\rho_e^4}{\rho_e^4\cos^2(2\theta_e) - 2\rho_e^4\cos^2(2\theta_e) + \rho_e^4}$$

$$= \frac{1}{1 - \cos^2(2\theta_e)} = \frac{1}{\sin^2(2\theta_e)} \tag{3.30}$$

Thus, from Eqs. (3.29) and (3.30) we can find ρ_e and θ_e for given values of A_{max} and ω_e as

$$\theta_e = \frac{1}{2}\sin^{-1}(1/A_{max}) \qquad \frac{\pi}{4} \leq \theta_e \leq \frac{\pi}{2} \tag{3.31}$$

$$\rho_e = \frac{\omega_e}{\sqrt{-\cos(2\theta)}} = \frac{\omega_e}{\sqrt[4]{1 - 1/A_{max}^2}} \, . \tag{3.32}$$

For the purposes of our simulation we chose ω_e to be exactly at the first zero position of the ideal low-pass filter, $\omega_e = 1$ and A_{max} to be

2 dB over the zero frequency value, $A_{max} = 1.259$. Of course, if any other values are desired, a simple change in program parameters is necessary. With these values, we find from Eqs. (3.31) and (3.32) that $\theta_e = 63.7^o$ and $\rho_e = 1.283$.

The two-pole resonant circuit described above, is cascaded with the Butterworth filter in both the transmitter and the receiver. The group delay characteristic of the cascade is highly nonlinear which causes the phase of the transmitted signal to deviate signficantly. Even the Butterworth filter alone has an unacceptably nonlinear group delay characteristic. Therefore, we need to compensate for the nonlinearity by adding an all-pass network with its group delay characteristic being nearly inverse to that of the PSF.

3.4.3 Group Delay Compensation with an All-Pass Filter

Design of an all-pass network with prespecified group delay characteristics is generally a very difficult problem [24]. However, there is a simplified procedure for designing a second-order all-pass network which utilizes a double series expansion of the group delay characteristics, which is very accurate for up to 95 percent of the filter passband [25]. We note that, in principle, higher order networks can also be designed using this method, but the underlying transcendental equations become impractically cumbersome.

3.4.3.1 Series Method for Group Delay Equalization

The design procedure is based on a power series expansion for the phase shift and group delay caused by a conjugate pair of poles (or zeros). A pair of poles $p_{1/2} = \rho\cos\theta \pm j\rho\sin\theta$ contributes to a phase shift by an amount given by

$$\phi(\omega) = -\tan^{-1}\frac{2\rho\omega\cos\theta}{\rho^2-\omega^2} = -\tan^{-1}\frac{2\frac{\omega}{\rho}\cos\theta}{1-(\frac{\omega}{\rho})^2}, \tag{3.33}$$

We first expand $\tan^{-1} x$ in the series

$$\tan^{-1} x = \sum_{k=1}^{\infty}\frac{(-1)^{k-1}x^{2k-1}}{2k-1}, \tag{3.34}$$

and then expand each of the terms $[1-(\omega/\rho)^2]^{-(2k-1)}$ into the binomial series

$$\begin{aligned}[1-(\frac{\omega}{\rho})^2]^{-(2k-1)} &= (1-\omega_n^2)^{-(2k-1)} \\ &= 1-(2k-1)\omega_n^2+\frac{(2k-1)2k}{2!}\omega_n^4-\frac{(2k-1)2k(2k+1)}{3!}\omega_n^6+\ldots\end{aligned} \tag{3.35}$$

where $\omega_n = \omega/\rho$. After this is done, like powers of ω_n of the double expansion are collected, and the first few terms are found to be of the form

$$\phi(\omega) = -2(\omega_n\cos\theta-\frac{\omega_n^3\cos 3\theta}{3}+\frac{\omega_n^5\cos 5\theta}{5}-\ldots). \tag{3.36}$$

The general k-th term in Eq. (3.36) is given by

$$-\frac{2(-1)^{k-1}\omega_n^{2k-1}\cos(2k-1)\theta}{2k-1}, \tag{3.37}$$

and the proof is given in [25]. Differentiating Eq. (3.36) with respect to ω we obtain the group delay as

$$\tau_g(\omega) = -\frac{d\phi(\omega)}{d\omega} = -\frac{1}{\rho}\frac{d\phi(\omega)}{d\omega_n}$$

$$= \frac{2}{\rho}\sum_{k=1}^{\infty}(-1)^{k-1}\,\omega_n^{2(k-1)}\cos(2k-1)\theta. \qquad (3.38)$$

For a single real pole $p_1 = -\sigma_1$ the above procedure is simplified in that the expansion given by Eq. (3.34) suffices, since $x=\omega$ in this case.

For a network of arbitrary complexity, the contributions of the real poles and zeros and the conjugate pairs of complex poles and zeros to the total phase shift or group delay simply add up, so that the total group delay, for example, is the summation of the series of the type given by Eq. (3.38).

3.4.3.2 PSF Delay Compensation

We can use the expansion of Eq. (3.38) to design an all-pass network which provides very good equalization within the passband of the filter. Compensation is performed in the following way: an all-pass network of predetermined order is cascaded with the network to be compensated. Total group delay is obtained in the form of Eq. (3.38) as

$$\tau_{gt}(\omega) = T_o + T_1\omega_n^2 + T_2\omega_n^4 + T_3\omega_n^6 + \ldots \qquad (3.39)$$

Now, the all-pass network parameters are chosen such that as many coefficients T_i (i=1,2,...) as possible are set to zero. We see that this procedure approximates the design of a maximally flat group delay network.

The number of coefficients T_i that can be cancelled obviously depends on the number of degrees of freedom (i.e. poles) of the all-pass network. So, with one conjugate pair of complex poles (and accompanying zeros) we can cancel T_1 and T_2, with 3 poles we can also set T_3 to zero, and so on. For our purposes it suffices to cancel T_1 and T_2, since the resulting group delay is then constant within 4 percent over 95 percent of the filter passband, as will be shown later. Besides, the resulting equations for the orders higher than two are very difficult to solve, even numerically.

We now apply the above technique to compensate the group delay of:

(a) a four-pole Butterworth filter (pulse shaping in the receiver) and

(b) a four-pole Butterworth filter cascaded with a two-pole resonant circuit (approximating an x/sin(x) equalizer in the transmitter).

The overall pole-zero pattern for the filters and compensating network is shown in Fig. 3.6. Subscripts to the pole and zero locations correspond to the type of filter: B-Butterworth, E-(aperture) equalizer, and A-all-pass filter.

(a) The overall transfer function of the Butterworth and all-pass is given by an expression of the form

$$H_{BA}(s) = H_B(s)H_A(s) = \frac{1}{1 + b_1 s + b_2 s^2 + b_3 s^3 + b_4 s^4} \, \frac{a_o - a_1 s + s^2}{a_0 + a_1 s + s^2} \tag{3.40}$$

In terms of pole-zero locations, the transfer function, evaluated on the $j\omega$-axis is given by

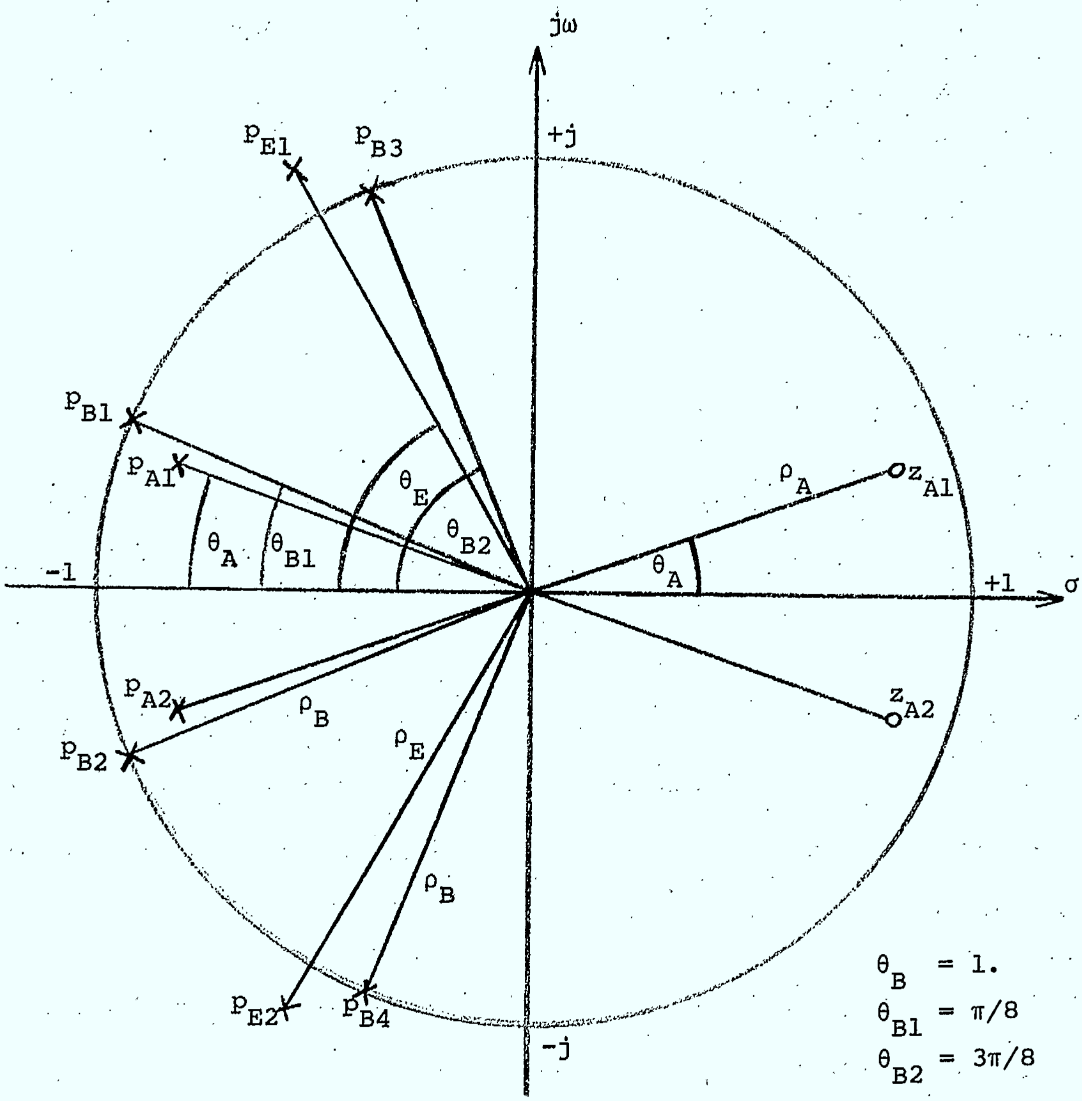

Fig. 3.6 Pole-zero locations for 4-pole Butterworth (B), 2-pole resonant equalizer (E), and second-order all-pass (A).

$$H_{BA}(j\omega) = \frac{(1 - \omega^2 - j2\omega\cos\theta_{B1})(1 - \omega^2 - j2\omega\cos\theta_{B2})}{[(1-\omega^2)^2 + 4\omega^2\cos^2\theta_{B1}][(1-\omega^2)^2 + 4\omega^2\cos^2\theta_{B1}]}$$

$$\times \frac{(\rho_A^2 - \omega^2 - j2\rho_A\omega\cos\theta_A)^2}{(\rho_A^2 - \omega^2)^2 + 4\rho_A^2\omega^2\cos^2\theta_A} \qquad (3.41)$$

where $\theta_{B1} = \pi/8$, $\theta_{B2} = 3\pi/8$, and we have used the fact that $\rho_B = 1$. The other parameters are indicated in Fig. 3.6.

Using the power series expansion for group delay given by Eq. (3.38) we have

$$\tau_{BA}(\omega) = \tau_B(\omega) + \tau_A(\omega)$$

$$= 4\left\{\frac{\cos(\pi/8)}{\sqrt{2}} + \frac{\cos(3\pi/8)}{\sqrt{2}}\omega^2 - \frac{\cos(5\pi/8)}{\sqrt{2}}\omega^4 - \frac{\cos(7\pi/8)}{\sqrt{2}}\omega^6 + \ldots\right\}$$

$$+ 4\left\{\frac{\cos\theta_A}{\rho_A} - \frac{\cos(3\theta_A)}{\rho_A^3}\omega^2 + \frac{\cos(5\theta_A)}{\rho_A^5}\omega^4 - \frac{\cos(7\theta_A)}{\rho_A^7}\omega^6 + \ldots\right\} \qquad (3.42)$$

For maximally flat group delay the coefficients of the second and fourth powers of ω should be zero which gives the conditions

$$(\cos 3\theta_A)/\rho_A^3 = \cos(3\pi/8)/\sqrt{2} \qquad (3.43)$$

and

$$(\cos 5\theta_A)/\rho_A^5 = \cos(5\pi/8)/\sqrt{2}\ , \qquad (3.44)$$

or numerically,

$$\cos 3\theta_A = 0.2706\ \rho_A^3 \qquad (3.45)$$

$$\cos 5\theta_A = 0.2706\ \rho_A^5\ . \qquad (3.46)$$

The set of equations (3.45) and (3.46) can be solved iteratively by first expressing ρ_A from (3.46) as

$$\rho_A = \frac{\sqrt[5]{-\cos 5\theta_A}}{0.2706} \tag{3.47}$$

and substituting into (3.45). The iterative formula for $\theta_A^{(n+1)}$ is

$$\theta_A^{(n+1)} = \frac{1}{3}\cos^{-1}[0.5928\ \sqrt[5]{-\cos 3\theta_A^{(n)}}]. \tag{3.48}$$

From the conditions $\theta_A \in [0,90^{\circ}]$ and $\rho_A > 0$ we find from Eqs. (3.45) and (3.46) that $18^{\circ} \leq \theta_A \leq 54^{\circ}$, and the initial condition, $\theta_A^{(0)}$, for the iteration of Eq. (3.48) has to be chosen from this interval. The solution is

$$\rho_A = 1.095 \quad \text{and} \quad \theta_A = 23.05^{\circ} \tag{3.49}$$

which gives the pole locations

$$p_{A1/2} = -1.00021 \pm j0.44679 \tag{3.50}$$

Cascading this network with the 4-pole Butterworth filter gives rise to a total group delay which for ω=0.9 is not more than 5 percent higher than at ω=0.

(b) The x/sin(x) aperture equalizer is approximated by a 2-pole resonant with the resonant frequency ω_e chosen to be 1. The amplitude response at ω=0 is unity and is 2 dB higher at $\omega=\omega_e$. With this characteristic, we find that the pole locations are determined by

$$\rho_E = 1.2830 \quad \text{and} \quad \theta_E = 63.7^{\circ} \tag{3.51}$$

or

$$p_{E1/2} = -0.56839 \pm j\ 1.15024 \tag{3.52}$$

The total group delay is now given by Eq. (3.42) plus the series corresponding to the delay introduced by the aperture equalizer. After some algebraic manipulations we obtain the set of equations

$$\cos 3\theta_A = 0.5029\ \rho_A^3 \tag{3.53}$$

$$\cos 5\theta_A = 0.3783\ \rho_A^5 \tag{3.54}$$

The solutions for Eqs. (3.53) and (3.54) are

$$\rho_A = 0.95172 \quad \text{and} \quad \theta_A = 21.44^\circ \tag{3.55}$$

with the corresponding pole locations

$$p_{A1/2} = -0.88588 \pm j0.34782. \tag{3.56}$$

Again $\tau_{gt}(0.9)/\tau_{gt}(0) < 0.05\ \tau_{gt}(0)$ as in the case of compensating the Butterworth filter alone. In the simulation both options (a) and (b) are provided.

3.5 Cochannel Interference (CCI)

Unwanted signals emanating from the same or a nearby satellite transmitter are usually termed as cochannel interference (CCI). There has been an effort to model the CCI and to obtain analytical results on its effect on channel performance [6,11,26-30]. In these references, CCI is modeled as one or more sinusoids at various frequences, various amplitudes, and random phases uniformly distributed between 0 and 2π.

To obtain the analytical results on the receiver performance in the presence of CCI, characteristic functions of its components were used [6,11,26,28]. In some cases, lower [11], and upper [11,29] error bounds were developed for the cases of K interfering sinusoids.

For our simulation purposes, we generate up to 10 sinusoids with random phases and add them to the signal at the appropriate points in the channel. Two options are provided as illustrated in Fig. 1.1: (1) adding them to the signal at the input of transmit or uplink (Chebyshev) filter, and (2) adding them to the signal at the output of the receiver or downlink filter. The number of CCI signals, as well as their positions in the passband are prespecified by the user. Positions are specified in terms of the fraction of the signal energy in the frequency band, so that they are independent of the absolute value of the passband. In other words, the specified position F1=0.2 for the first CCI signal means that it is positioned at the frequency f_1 specified by

$$\int_{-f_1}^{f_1} |X(f)|^2 df = 0.2\, E_X \tag{3.57}$$

where E_X is the total signal energy.

Because of the way the CCI sinusoids and their frequencies are specified, the addition to the useful signal is performed in the frequency domain, i.e., when it is Fourier transformed for multiplication with the uplink filter transfer function (or, for the other option, when it is multiplied with downlink filter transfer function).

The strength of the CCI signal is prespecified in terms of the parameter SCCIR which is the ratio of the signal power to the total CCI power. For the K CCIs, each has the same power equal to 1/K of the total power. In this way, the number of input parameters, specifying the CCI field, is kept to a minimum. This makes it very simple to modify the program to provide for the specification of the power for each CCI component, if desired by the user.

3.6 Adjacent Channel Interference (ACI)

In modern satellite communications systems there is a growing demand for passing more and more channels through the same transponder. The separation between channels becomes smaller and a lot of effort has been expanded recently on developing bandwidth-efficient modulation schemes (e.g., [31]).

If, for any reason, the carrier frequency of one channel drifts from its nominal vlue, a portion of the signal spectrum will leak into a neighbouring channel, thus causing an adjacent channel interference (ACI). The ACI can also occur because of spectral spread due to channel nonlinearities, and because of finite transition region in frequency responses of neighbouring channel filters. The occurrence of the ACI will cause the degradation of the system performance particularly when the channel nonlinearities are not negligible.

The usual way to model the ACI is to assume that both the adjacent channels on each side of the wanted channel employ the same type of modulation as the main one [6,12,27,30]. We can assume any separation between the carrier frequencies. In order to enable a general comparison for different modulation schemes, we decided to specify a normalized channel separation as a fraction of the total simulation bandwidth which is constant, independent of the modulation type, as explained in section 3.1 Another simulation parameter is the ratio of the total ACI power to the signal power. The parameter is recomputed in the program after the ACI has passed through the main channel filters, and given as an output parameter. An independent BT product is specified in the simulation (BTINT) and can be chosen to be either the same or not the same as the main channel BT product. Again, as in the CCI case, options are provided for adding the ACI signals in either uplink and downlink path, as shown in Fig. 1.1.

Generation of the ACI, and its processing up to the mixing point in the channel is the same as for the main channel, except that the random sequence (PN) generator is shifted by a half of its length, so as to avoid significant correlation with the main channel signal. Empirical investigations have shown that the use of a different PN sequence generator for the ACI does not significantly change the correlatedness between two symbol streams, so the same generator is used for computational simplicity. In the simulation program the ACI is first generated, processed up to the mixing point, and stored in the frequency domain. The main signal is then generated, processed, the ACI is added to it, and the summation is then further processed up to the probability of error calculator.

Figure 3.7 illustrates how the ACI spectrum is rearranged before it is added to the main signal spectrum. The dotted curves in diagrams (a), (b) and (c) represent the real part of the main signal amplitude spectrum in the way it appears in the FFT (real) array. The abscissa is labeled in indices of this array and it is 4096 points long for all modulation types. The solid line in diagram (a) is a prescribed position of the neighbouring channel's spectra where the channel separation is chosen to be CHSEP = 1408 frequency samples (which amounts to 11/16-ths of the simulation bandwidth). As mentioned above, the ACI spectrum is generated so that it occupies the same frequency region as the main spectrum. We now shift the "lower" half of the ACI spectrum into the right on the frequency axis to obtain two sections of the ACI spectrum, shown by solid lines in Fig. 3.7(b). Similarly, we then shift the "upper" half of the spectrum toward the left and thus obtain the solid line sections in Fig. 3.7(c). The total ACI spectrum in the FFT array is obtained by summing the solid segments in Figs. 3.7(b) and (c). The result is the solid spectrum in Fig. 3.7(a).

If we transpose the upper half of the spectrum into the negative frequency domain, we obtain the baseband representation of the main signal spectrum and both adjacent channel spectra, i.e., the portions of these spectra which appear in the simulation bandwidth as shown in Fig. 3.7(d). After the channel filtering, only the parts of ACI spectra which overlap with the main signal spectrum, affect the channel performance.

What is said about the rearrangement of the real part of the ACI spectrum obviously holds for the imaginary part too, since the processing illustrated in Fig. 3.7 is, in fact, performed for real and imaginary parts of the spectrum simultaneously.

The allowable range for the parameter CHSEP is one half of the simulation bandwidth, that is, $CHSEP_{max}$ = 2048, while the lower limit is 1, thereby permitting total overlap of the main and ACI spectra. We add that in the simulation, the actual value of the prescribed parameter is in the normalized range [0,1] where the value of 1 corresponds to 2048 frequency samples.

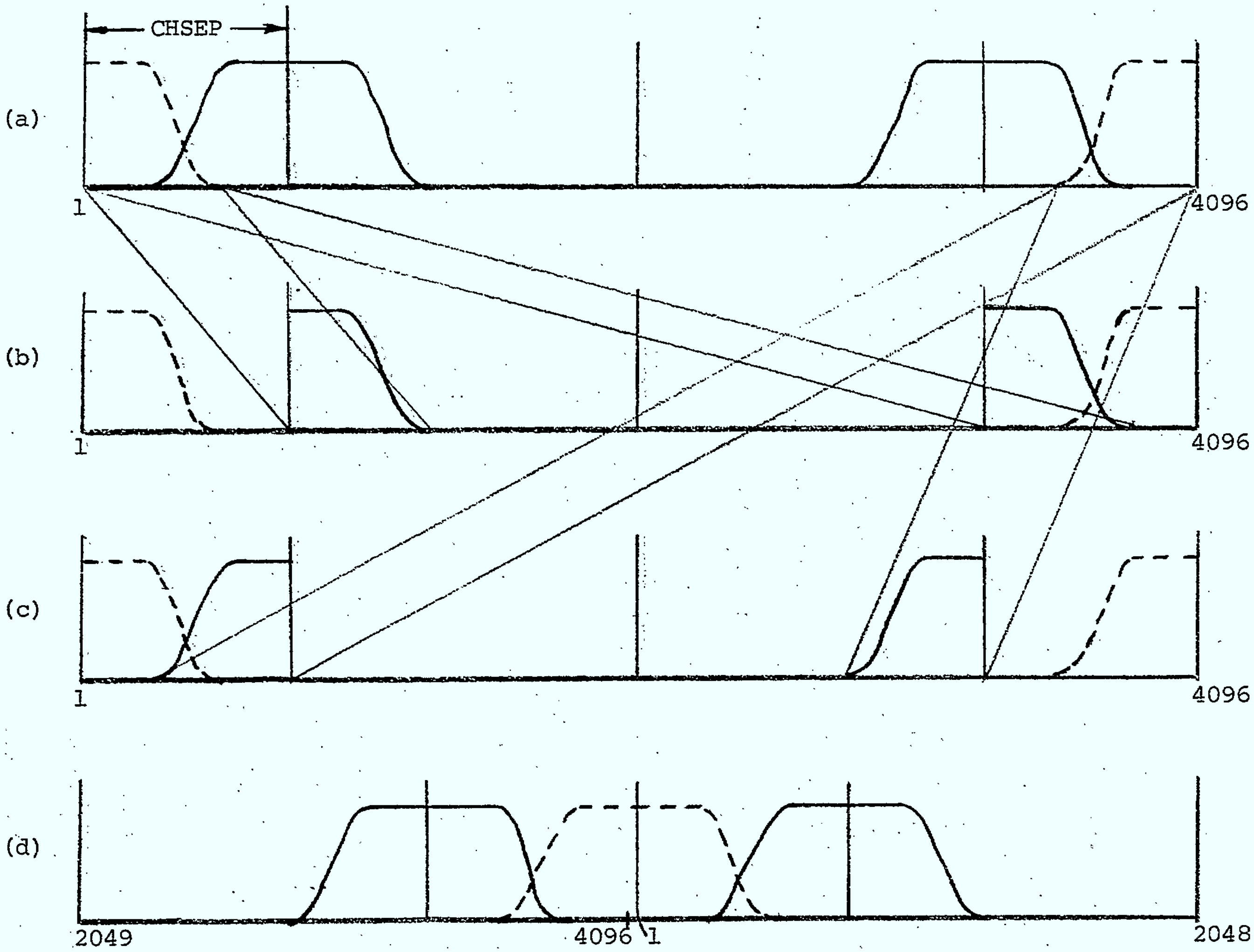

Fig. 3.7 Rearranging the position of the ACI spectrum: (----) main signal spectrum; (———) ACI spectrum.

4. RECEIVER STRUCTURES

4.1 Demodulation

At the input of the receiver, the modulated signal is represented as

$$s_r(t) = A(t)\cos[\omega_c t + \phi(t)] \tag{4.1}$$

where

$A(t)$ = signal amplitude

ω_c = angular carrier frequency

$\phi(t)$ = the received phase.

The first function of the demodulator is to separate the carrier from the information. This may be done by coherent detection or differential detection depending on how the information is encoded. In coherent detection, the incoming signal, given by Eq. (4.1) is multiplied by a local oscillator signal which is assumed to be ideally synchronized in frequency and phase to the received carrier. The effect of imperfect synchronization will be discussed later in this chapter.

The signal is multiplied by the local oscillator signal and its 90^o shifted version to obtain in-phase and quadrature components, as

$$s_r(t)\cos\omega_c t = \frac{A(t)}{2}\{\cos[2\omega_c t + \phi(t)] + \cos\phi(t)\} \tag{4.2}$$

and

$$s_r(t)\sin\omega_c t = \frac{A(t)}{2}\{\sin[2\omega_c t + \phi(t)] + \sin\phi(t)\} \tag{4.3}$$

After low-pass filtering, the in-phase and quadrature channel baseband signals are obtained as

$$x(t) = \frac{A(t)}{2} \cos\phi(t) \tag{4.4}$$

and

$$y(t) = \frac{A(t)}{2} \sin\phi(t) \tag{4.5}$$

In differential detection a delayed (by one symbol) replica of the incoming signal is multiplied by the incoming signal to obtain

$$[A(t)\cos(\omega_c t + \phi_m)][A(t-T)\cos(\omega_c t + \phi_{m-1})]$$

$$= \frac{A(t)A(t-T)}{2} [\cos(2\omega_c t + \phi_m + \phi_{m-1}) + \cos(\phi_m - \phi_{m-1})] \tag{4.6}$$

and

$$[A(t)\cos(\omega_c t + \phi_m)][A(t-T)\sin(\omega_c t + \phi_{m-1})]$$

$$= \frac{A(t)A(t-T)}{2} [\sin(2\omega_c t + \phi_m + \phi_{m-1}) + \sin(\phi_m - \phi_{m-1})]. \tag{4.7}$$

After low-pass filtering, the in-phase and quadrature channel baseband signals are obtained as,

$$x(t) = \frac{A(t)A(t-T)}{2} \cos(\phi_m - \phi_{m-1}) \tag{4.8}$$

$$y(t) = \frac{A(t)A(t-T)}{2} \sin(\phi_m - \phi_{m-1}). \tag{4.9}$$

The simulation does not include the carrier at any point. The complex baseband signal is processed through the channel with equivalent baseband filter characteristics. The signal at the input of the receiver is the signal after the carrier has been separated from the information, that is in the form of the Eqs. (4.4), (4.5) or (4.8), (4.9).

4.2 The Simulation of Noise

There are two possible approaches to the simulation of noise in a communications system, namely, 1 - Simulated noise,

2 - Computed noise.

In the simulated noise case, Gaussian noise is generated in both the in-phase and quadrature channels, for every sample of the signal. The variance of the noise is inversely proportional to the specified signal-to-noise ratio (SNR). The noise and the signal are added sample by sample, and passed through the simulated receiver. The output is demodulated and compared to the input signal. Symbols in error are counted, and the ratio of the number of received symbols in error to the total number of symbols simulated is the required average probability of error for the particular modulation system being simulated at the given SNR and bit rate.

With computed noise, the noise is moved to the output of the receiver filter. The equivalent noise power at the output of the filter is computed according to theory. The signal is simulated in the absence of noise. The probability of error for each signal symbol may be computed provided the symbol energy is known and the nominal SNR is specified. This is done for only a limited number of symbols which approximates the true distribution of signal symbols. The overall probability of error is an average over the signal distribution. The longer the signal sequence is, the better the approximation to the true error rate will be.

Due to a prohibitive amount of computer time needed for the simulated noise computation, it is concluded that computed noise be used in the simulation. Since theories on noise through nonlinear channels are difficult to apply, only the downlink noise is treated in the simulation.

4.3 The Receiver

The received modulated signal is passed through a bandpass filter and is converted to baseband by beating it with a local sinusoidal signal in synchronization with a carrier wave. In the DPSK case, the incoming signal is delayed by one baud. The signal and its delayed replica are then multiplied to obtain the baseband signal. In the simulation, only the baseband signal exists; it is assumed that the removal of carrier wave has been achieved. In order to determine which symbol has been sent in the presence of noise and ISI, the demodulator generally includes some sort of matched filter to maximize the SNR. For a rectangular signal pulse, the optimum detector is an integrate-and-dump filter (IDF). However, when the signal is subjected to a PSF with group delay equalizer, it was found that the peak value detector (PVD) yields somewhat better performance than the IDF. We shall, therefore, use both detectors in the simulation.

4.3.1 Integrate-and-Dump Filter (IDF)

Figure 4.1 depicts the receiver with the IDF in block diagram form. The signal alone is simulated, and the noise source is considered to be at the output of the IDF, as indicated in Fig. 4.2.

The effective noise power at the output of the IDF is computed according to theory. The simulated signal is integrated over one symbol interval. A sample is taken at the end of each symbol interval. The average symbol energy is estimated from the output of the IDF. With the nominal SNR specified, the actual bit energy to noise ratio E_B/N_o can be computed. The probability of error for this value can then be computed according to theory. This is done for the entire string of symbols in

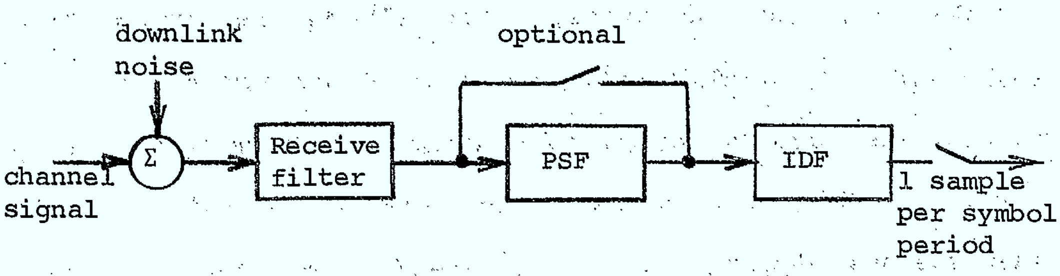

Fig. 4.1 General receiver block diagram.

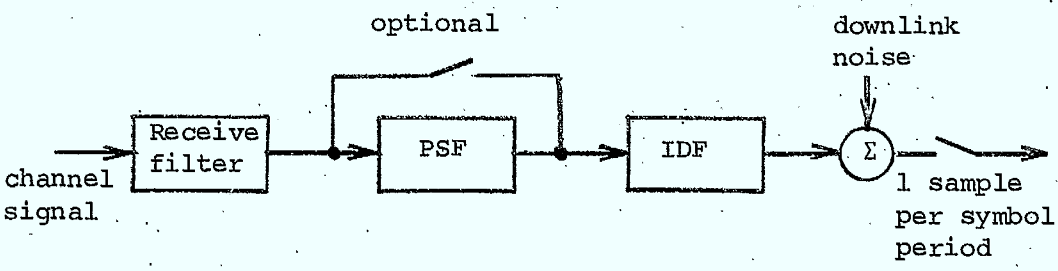

Fig. 4.2 Receiver block diagram as simulated.

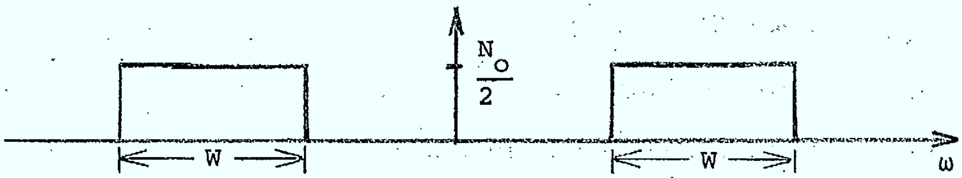

Fig. 4.3 Additive noise spectrum.

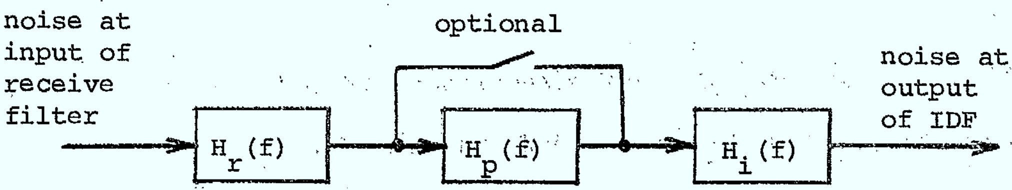

Fig. 4.4 Cascade of receive filter, PSF, and IDF in the frequency domain.

the sequence, and the average over all symbols processed is the representative probability of error curve of the system being simulated. The downlink noise is assumed to be Gaussian with zero mean and variance σ^2 where σ^2 is the noise power. The noise is assumed to be white with two-sided spectral density $N_o/2$ in the frequency band of interest, as shown in Fig. 4.3. The symbol probability of error is related to the SNR.

The definition of SNR may be stated as

$$\mathrm{SNR} = \frac{A^2}{2\sigma^2} = \frac{E_s}{N_o\ BT} = \frac{E_b}{N_o} \cdot \frac{1}{BT} \log_2 M \tag{4.10}$$

where

$A^2/2$	is the power of the RF signal
σ^2	is the noise power
E_s	is the symbol energy
T	is the symbol duration
E_b	is the bit energy
N_o	is the 1-sided noise power spectral density
B	is the signal 3 dB bandwidth
M	is the number of possible symbols in signal space.

In Chapter 6, we shall present all results in terms of the bit energy to noise ratio E_b/N_o.

Now let us calculate the effective noise power after it has passed through the receive filter, the PSF, and the IDF.

Let the transfer function of the receive filter be denoted by $H_r(f)$, the transfer function of the PSF be denoted by $H_p(f)$, and that of the IDF by $H_i(f)$ as indicated in Fig. 4.4. The input-output relationship of an IDF is given by

$$y(t) = \begin{cases} \frac{1}{T} \int_0^t x(u)\,du; & 0 < t \leq T \\ 0; & \text{otherwise.} \end{cases} \qquad (4.12)$$

Then, in the system being simulated the noise power at the output of the IDF is given by

$$\sigma_{N_o}^2 = \int_{-\infty}^{\infty} N_o \; |H_r(f)|^2 \; |H_p(f)|^2 \; |H_i(f)|^2 df \qquad (4.13)$$

If the PSF is not included, the term $|H_p(f)|^2$ is simply dropped from Eq. (4.13). This equation is readily implemented in discrete form.

4.3.2 Peak Value Detector (PVD)

As already mentioned, the IDF may not be the optimum detector when the signal is subjected to the PSF. We may then use the peak value detector (PVD) which simply seeks for the relative peak in each received symbol. The signs of the peak value in both I and Q channels determine which symbol was transmitted.

Treatment of the downlink noise and, accordingly, the computation of the SNR at the output of the PVD is exactly the same as in the case of the IDF, explained in the previous section. The IDFs in Figs. 4.1 and 4.2 need only be replaced by a circuit which discriminates the largest relative value of the symbol sample. In the equivalent noise power calculation, illustrated in Fig. 4.4, and presented by Eq. (4.13) the $H_i(f)$ should only be replaced by unity.

To make the comparison of both detection methods possible we provide both IDF and PVD options in the simulation by simply giving the corresponding value to the input parameter ISYNC. When ISYNC =0, the detection is provided by an IDF while ISYNC = 1 causes the symbol detection by a PVD. This way the choice is independent of the presence or the absence of the PSF.

4.4 Probability of Error Computation

The calculation of probability of error for received symbols in the presence of Gaussian noise differs from one modulation to another. For the case of the ideal receiver synchronization, they will be described below in separate subsections. The case where synchronization errors exist will be treated in the next section.

4.4.1 M-ary CPSK

4.4.1.1 General M-ary CPSK

It can be shown [23] that Gaussian random noise in narrow band channels can be represented by I and Q channel components as

$$n(t) = n_x(t)\cos\omega_c t + n_y(t)\sin\omega_c t \tag{4.14}$$

where $n_x(t)$ and $n_y(t)$ are independent and Gaussian. The statistics governing $n_x(t)$ and $n_y(t)$ are identical namely,

$$p(n_x) = \frac{1}{\sqrt{2\pi}\,\sigma} e^{-(n_x^2/2\sigma^2)} \tag{4.15}$$

$$p(n_y) = \frac{1}{\sqrt{2\pi}\,\sigma} e^{-(n_y^2/2\sigma^2)} \tag{4.16}$$

where σ^2 is the variance of the random variables n_x and n_y and equals the noise power.

When a narrow band signal is received by the receiver, I and Q components of the signal will result after it is coherently detected. The signal components are corrupted by the I and Q noise components. Thus, the resulting signal and noise has the form

$$s(t) = [s_x(t) + n_x(t)]\cos\omega_c t - [s_y(t) + n_y(t)]\sin\omega_c t \tag{4.17}$$

Figure 4.5 depicts a phasor diagram of the signal and noise. The resultant vector representing the signal plus noise in the phasor plane will have a certain probability of having its tip in a particular region in the phasor plane.

For M-ary PSK signals the phasor plane is divided into M equal sectors, each of which represents a region for correct detection of a symbol. The probability of a received symbol being in error is simply the probability that the resultant signal plus noise vector lies outside the given region.

The I and Q components of the signal plus noise may be considered as a random process. Define the random variables X(t) and Y(t) by

$$X(t) = s_x(t) + n_x(t) \tag{4.18}$$

$$Y(t) = s_y(t) + n_y(t). \tag{4.19}$$

The joint density function of X and Y, for independent noise components and fixed signal components is

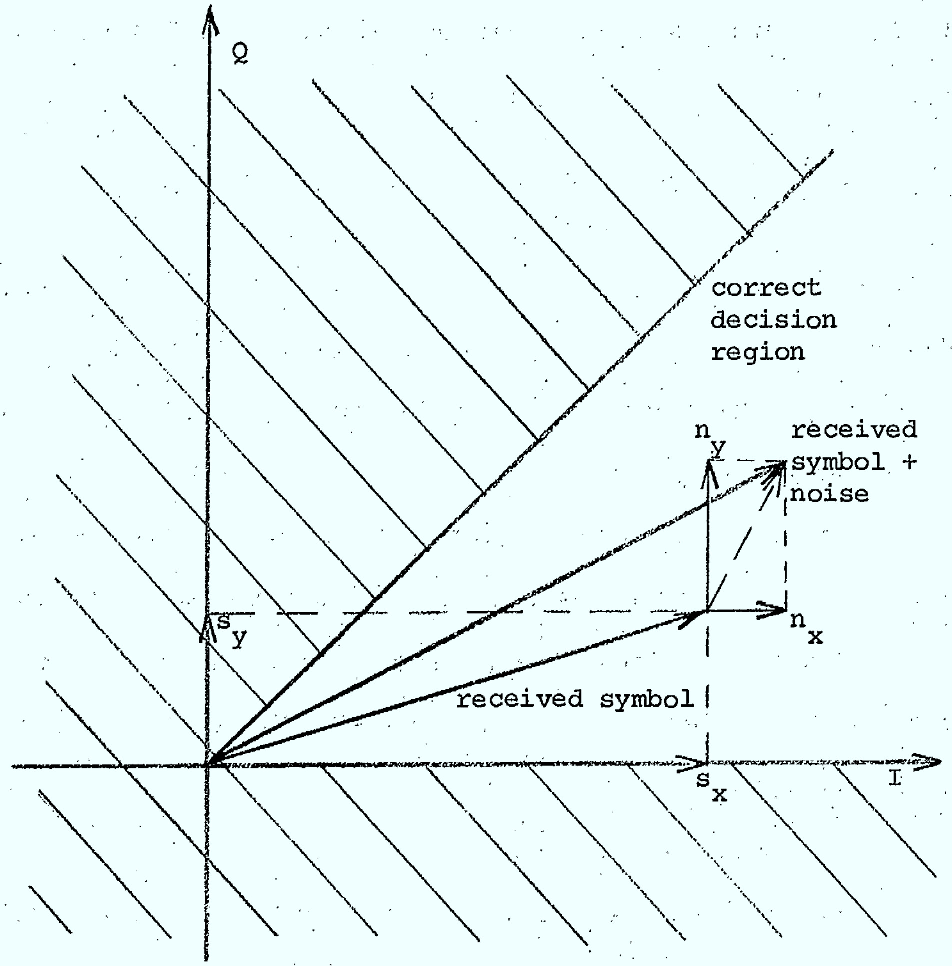

Fig. 4.5 General phasor representation of signal and noise.

$$p(X,Y) = p(X)p(Y)$$

$$= \frac{1}{2\pi\sigma^2} e^{-[(X-s_x)^2+(Y-s_y)^2]/2\sigma^2} \qquad (4.20)$$

The required phase density function is found by transforming Eq. (4.20) into polar coordinates, $p(X,Y) \to p(R,\theta)$, where

$$R(t) = \sqrt{X^2(t) + Y^2(t)} \qquad (4.21)$$

$$\theta(t) = \tan^{-1}[Y(t)/X(t)]. \qquad (4.22)$$

We may then rewrite Eq. (4.20) in the form

$$p(R,\theta) = \frac{R}{2\pi\sigma^2} e^{-[R^2+A^2-2RA\cos(\theta-\phi)]/2\sigma^2} \qquad (4.23)$$

where signal components are expressed as $s_x = A \cos \phi$ and $s_y = A \sin \phi$. The probability density function $p(\theta)$ of the random variable θ is obtained by integrating Eq. (4.23) from $R=0$ to $R=\infty$ to get

$$p(\theta) = \frac{e^{-\rho}}{2\pi} + \sqrt{\frac{\rho}{\pi}} \cos(\theta-\phi)\mathrm{erfc}[-\sqrt{\rho} \cos(\theta-\phi)] \qquad (4.24)$$

where erfc(•) is the complementary error function

$$\mathrm{erfc}(z) = \frac{2}{\sqrt{\pi}} \int_z^\infty e^{-u^2} du, \qquad (4.25)$$

and

$$\rho = E_B/N_o.$$

Due to intersymbol interference (ISI), the received symbol in the absence of noise will not lie exactly in the center of the correct region, but rather will be displaced by a certain distance from the center, as explained in the previous work [1]. It was also illustrated in [1] that in the case of severe ISI, some received symbols may be in error even in the absence of Gaussian random noise. In this case the probability of error is

$$1 - \text{Prob (the noise will swing the received symbol back to the correct region)} \tag{4.26}$$

4.4.1.2 The Special Case of 2- and 4-phase CPSK

The cases of 2 and 4 phase CPSK have some unique features which makes the computation of probability of error much simpler. It also applies in the cases of OPSK and FFSK. They are discussed in the next subsection. The case of 2-phase CPSK is treated, and the extension to the 4-phase case is straightforward.

In the 2-phase case, the received symbol can assume only two values. An error is committed if the noise has sufficient energy to swing the received symbol in the opposite direction so that the received symbol has a sign opposite to that of the transmitted symbol. The probability of error for the 2-phase CPSK is given by a well known results [23]

$$P_e = \frac{1}{2}\,\mathrm{erfc}(\sqrt{\rho}) \tag{4.27}$$

The probability of error for the 4-phase CPSK case is readily obtained from the 2-phase result [23].

4.4.1.3 The OPSK and FFSK

The calculation of probability of error for OPSK and FFSK is identical to the coherent 4-phase case. Once the symbol energy is estimated, the probability of error can be computed from Eq. (4.27).

In the OPSK case, the I and Q channel signals are obtained after coherent detection. An IDF is used in each channel to integrate the received I and Q signals for one symbol interval. At the end of every symbol interval, a sample is taken and its sign is used to determine the sign of the transmitted symbol.

In the FFSK case, a similar procedure is applied, except that the symbols are weighted by a half sine before an IDF is applied.

4.4.1.4 Differentially Encoded CPSK

As shown in subsection 2.1.2 the Differentially Encoded CPSK yields approximately twice the value of the probability of error of the corresponding coherently encoded modulation. In fact, the probability of error is given by Eq. (2.18).

$$P_e = 2P_e' - P_e'^2 \tag{4.28}$$

where P_e' is the probability of error for the corresponding CPSK. For very small P_e', $P_e \simeq 2P_e'$ and for larger value of P_e' it is somewhat less than $2P_e'$.

4.4.2 Differential PSK

The differential decoding requires the multiplication of the incoming signal by its delayed (by one symbol) replica. Hence, when considering probability of error, noise samples at two time instants are involved. The retrieval of information from DPSK signals may be considered as the process of evaluating the difference of the phase angles represented by two successive symbols. In the analysis of CPSK, it was noted that the vector representing the signal plus noise has a probability density given by Eq. (4.24). The tip of the vector representing the first symbol plus noise has a probability that it will lie anywhere on the phase plane. The same is true for the tip of the vector representing the second symbol. Therefore, the difference between these two vectors will have a definite probability of lying anywhere on the phase plane. This probability is described by a density function obtained by the convolution of the two phase density functions associated with the two symbols. Figure 4.6 depicts the two signal symbols plus noise in the phase plane.

For the two successive signal symbols, s_1 (delayed symbol) and s_2 with amplitudes A_1 and A_2, the probability density function for the phase differential

$$\Delta\theta = \theta_2 - \theta_1 \tag{4.29}$$

is given by the convolution integral [1]

$$P(\Delta\theta) = \int_{-\pi}^{\pi} \left[\frac{e^{-\rho_1}}{2\pi} + \sqrt{\frac{\rho_1}{\pi}}\cos\theta e^{\rho_1 \sin^2\theta} \operatorname{erfc}(-\sqrt{\rho_1}\cos\theta)\right]$$

$$\cdot\left[\frac{e^{-\rho_2}}{2\pi} + \sqrt{\frac{\rho_2}{\pi}}\cos(\theta+\Delta\theta) e^{-\rho_2 \sin^2(\theta+\Delta\theta)} \operatorname{erfc}(-\sqrt{\rho_2}\cos(\theta+\Delta\theta))\right]d\theta, \tag{4.30}$$

where

$\rho_i = A_i^2/2\sigma^2$, $i=1,2$

σ^2 = noise power.

The probability of error, is then given by [1]

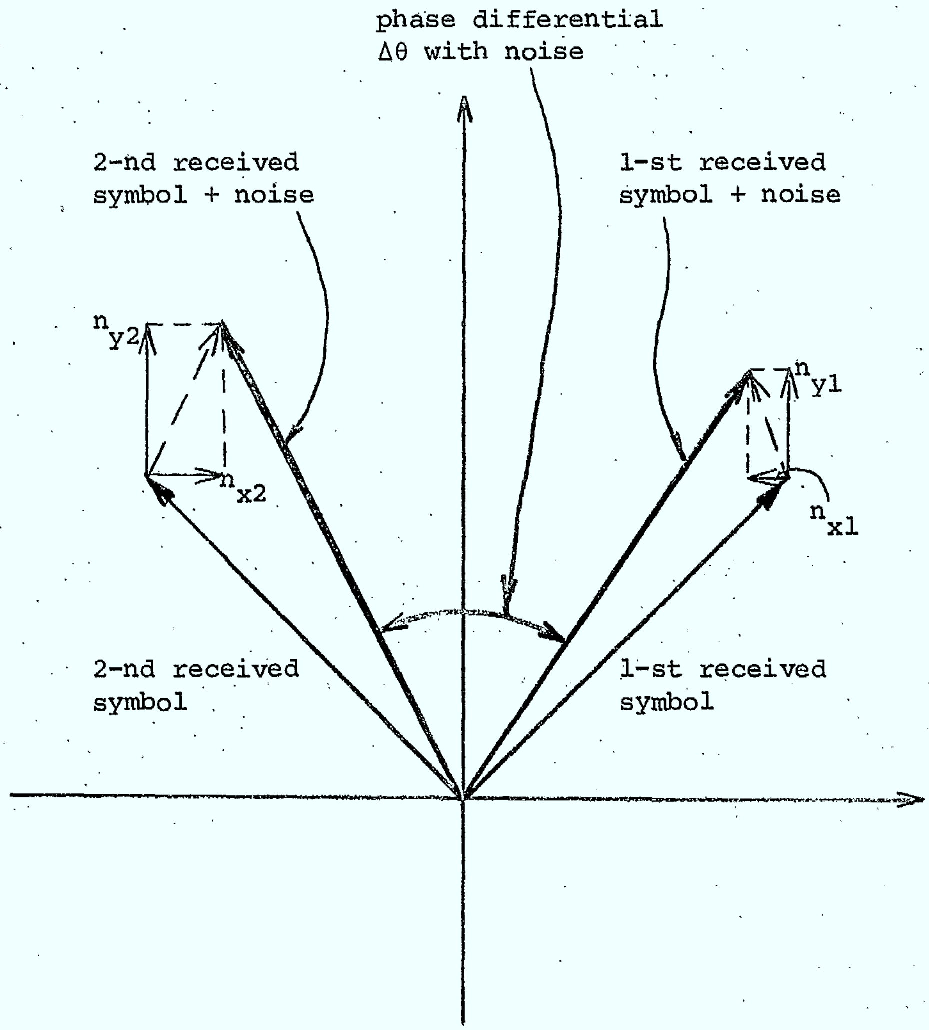

Fig. 4.6 DPSK signal space or phasor representation showing the effect of additive noise.

$$1 - \int_I P(\Delta\theta)d(\Delta\theta) \tag{4.31}$$

where I is the correct decision region.

4.5 Synchronization Considerations

The analysis of the coherently encoded CPSKs and FFSK, presented in the Section 4.4, assumed an ideally synchronized receiver. When this assumption is not justified, i.e., when the carrier/symbol synchronization is not perfect, additional degradation of the receiver performance occurs. In our analysis we shall treat carrier synchronization and symbol synchronization separately.

4.5.1 Carrier Recovery

Carrier recovery circuits for the coherent modulations consist of either the M-th power circuit or the Costas loop. For a binary CPSK, M=2, which yields a squaring circuit while for M=4 the filtered incoming signal is taken to the fourth power. The integral part of any carrier recovery circuit is a phase-locked oscillator (PLO). An example of the carrier recovery circuit for the 2-phase CPSK with square-law technique, is shown in block diagram form in Fig. 4.7 [30]. The incoming signal embedded in a white Gaussian noise is bandpass filtered and squared and passed through the PLO (bounded by a dashed rectangle in the figure). The PLO output is multiplied by the input signal, and the product is passed through a matched filter, after which the decision about the transmitted phase ϕ_n is made.

The squaring operation effectively removes the modulation $\pm A$ and creates a line component in the spectrum at double carrier frequency

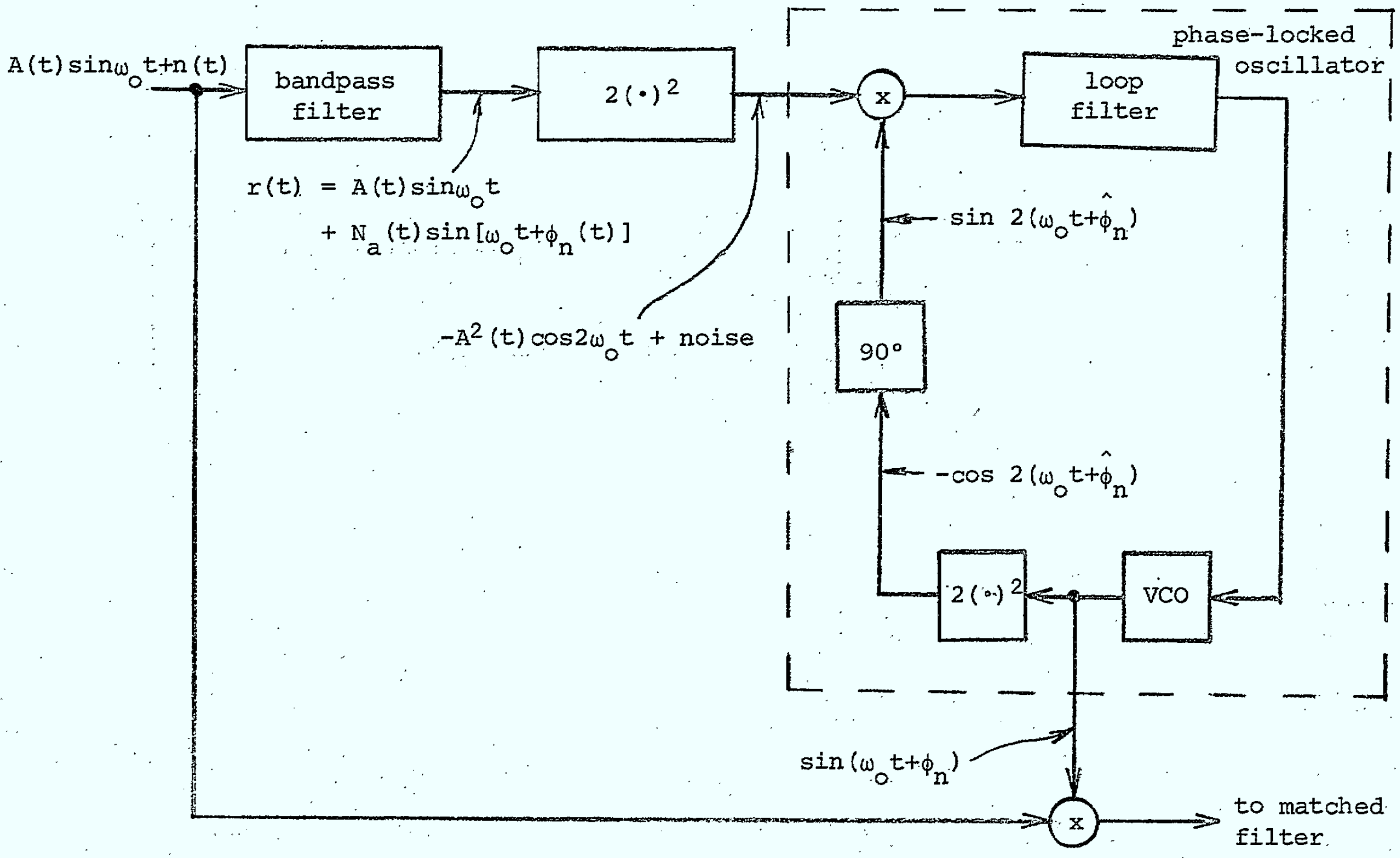

Fig. 4.7 Block diagram of the square-low carrier recovery technique.

$2\omega_o$. The squared output for an input r(t) can be represented as

$$2r^2(t) = 2\{A(t)\sin\omega_o t + N_a(t)\sin[\omega_o t + \phi_n(t)]\}^2$$

$$= -A^2(t)\cos 2\omega_o t - 2A(t)N_a(t)\cos[2\omega_o t + \phi_n(t)] \qquad (4.32)$$

$$= N_a^2(t)\cos[2\omega_o t + 2\phi_n(t)] + A^2(t) + N_a(t) + A(t)N_a(t)\cos\phi_n(t)$$

where $N_a(t)$ is the amplitude, and $\phi_n(t)$ phase of the bandpass filtered input noise component. The first term on the right hand side of Eq. (4.2) is the line component of the spectrum at $2\omega_o$ and the other terms are noise and DC biased terms. The PLO acts as a narrowband filter centered about carrier frequency ω_o. It attempts to track the input phase ϕ_n representing the pure carrier component at the output of the second (or fourth) power multiplier in the carrier recovery loop. During the tracking procedure, the estimate $\hat{\phi}_n$ of phase ϕ_n will be in error

$$\varepsilon \triangleq \phi_n - \hat{\phi}_n \qquad (4.33)$$

Depending on various factors, e.g., PLO loop filter order, PLO noise loop bandwidth, B_n, and others [30], the amount of error ε will remain even after the tracking is performed. The principle influence on the amount of ε is due to the finite loop noise bandwidth B_n. In fact, we can find theoretical degradation of performance caused by imperfect carrier synchronization, by specifying B_n and by knowing the probability distribution of the error ε.

The steady-state probability density function for the phase error for a PLO is given by the Tikhonov density function [30] as

$$p(\varepsilon) = (e^{\alpha\cos\varepsilon})/2\pi I_o(\alpha) \qquad (4.34)$$

where $I_o(\cdot)$ is the modified Bessel function of zero order, and α is the parameter related to the normalized output-noise bandwidth factor δ by

$$\alpha = \frac{E_b}{N_o} \cdot \frac{\delta}{4} \tag{4.35}$$

and δ is given by

$$\delta = \frac{1}{B_n T(1 + BTN_o/E_b)} \cdot \tag{4.36}$$

In Eq. (4.36) B_n is the noise loop bandwidth, B is the channel signal 3 dB bandwidth, T is symbol duration, and E_b/N_o is the bit energy to noise ratio. It is clear that the smaller the noise loop bandwidth B_n is, the larger the noise bandwidth factor δ becomes. Ideally, as $B_n \to 0$, $\delta \to \infty$, and $\varepsilon \to 0$. This would require, however, infinitely long tracking time.

For the 2-phase CPSK, the output-error probability is obtained by averaging the error probability for a given phase error ε over all $|\varepsilon| < \pi$ [30]

$$P_e(2) = \int_{-\infty}^{\pi} \frac{e^{\alpha\cos\varepsilon}}{2\pi I_o(\alpha)} \operatorname{erfc}\left(\sqrt{\frac{2E_b}{N_o}} \cos\frac{\varepsilon}{2}\right) d\varepsilon. \tag{4.37}$$

In the simulation, we specify the value δ which we want to use in the particular calculation and the probability of error is calculated by using Eq. (4.37) where all other quantities are already known.

For the 4-phase CPSK case, similar arguments yield the following expression for the probability of error [30].

$$P_e(4) = \int_{-\pi}^{\pi} \frac{e^{\alpha\cos\varepsilon}}{8\pi I_o(\alpha)} \left\{\operatorname{erfc}\left[\sqrt{\frac{2E_b}{N_o}} \cos\left(\frac{\pi-\varepsilon}{4}\right)\right] + \operatorname{erfc}\left[\sqrt{\frac{2E_b}{N_o}} \cos\left(\frac{\pi+\varepsilon}{4}\right)\right]\right\} d\varepsilon \tag{4.38}$$

where, in this case

$$\alpha \triangleq \beta \cdot \frac{E_b}{N_o} \tag{4.39}$$

and β is a quantity dependent on the E_b/N_o, the BT product, and the bandwidth ratio B/B_n [30]. Again, we specify z as our simulation parameter.

Since the OPSK and FFSK are generated in the same way as 4-phase CPSK, their error rate performances are computed in the same way, i.e., by using Eq. (4.38).

4.5.2 Symbol Synchronization

Power-efficient digital receivers generally require the existence of a digital clock synchronized to the receiver symbol stream to control the integrate-and-dump detection filters and/or to control otherwise the timing of the output symbol stream.

We shall briefly mention here four different classes of symbol/bit synchronizers. They are all self-synchronizing techniques applied to non-return-to-zero (NRZ) symbol streams [30].

(1) Nonlinear-filter synchronizer [34].

This open loop type of synchronizer functions by linearly filtering the received symbol stream to reduce the noise and to magnify the observability of the symbol transitions. The filter output is then passed through a memoryless even-law nonlinearity to produce a spectral line at the symbol rate. This synchronizer is commonly used in high bit rate links and links which normally operate at high SNR.

(2) Inphase/Midphase (IP/MP) synchronizer (also termed the data transition tracking synchronizer)[35].

This synchronizer operates in a closed loop and combines the operations of symbol detection and symbol synchronization. The symbol detector determines which symbols represent a change from the previous symbol and whether a (10) or a (01) transition has occurred. This transition information is then utilized to provide the correct sign to a tracking error channel. The IP/MP synchronizer can be employed even at low SNR and medium data rates. It also operates well even in the presence of relatively long times between transitions.

(3) Early-late bit synchronizer [36].

This type of bit synchronizer is similar to the IP/MP technique. It too involves a closed loop system but has a somewhat different method of obtaining the bit-timing error estimate.

(4) Optimum (maximum-likelihood) synchronizer [34].

This type of synchronizer uses an optimal means for searching for the correct synchronization time cell during acquisition. This synchronizer is an open-loop system rather than a tracking technique. This approach is generally not practical; nevertheless it does represent a bound on obtainable performance.

We see that a variety of symbol/bit synchronizing techniques exist in digital communications systems. The above mentioned techniques are only a few, and they are restricted to a particular signalling type. It is impractical to examine the different synchronization schemes in the simulation. It is more practical to analytically examine the influence of the bit synchronization error on the bit error rate; the same approach we adopted for carrier synchronization. This way the comparative analysis of various modulation schemes is possible, and performance prediction is obtainable.

The probability density function of the clock timing error, normalized to the symbol duration, $\varepsilon_n = \varepsilon/T$ is given by the Tikhonov density function [15] as

$$p(\varepsilon_n) = \frac{e^{\cos(2\pi\varepsilon_n)/(2\pi\sigma_\varepsilon)^2}}{I_o[1/(2\pi\sigma_\varepsilon)^2]} . \quad (4.40)$$

The bit error probability for a given clock timing error ε_n is [15]

$$P_e(\varepsilon_n) = \frac{1}{4}\,\mathrm{erfc}\{\sqrt{\frac{E_b}{N_o}} \circ \frac{R_s(\varepsilon_n) + R_s(1-\varepsilon_n)}{R_s(0)}\}$$

$$+ \frac{1}{4}\,\mathrm{erfc}\{\sqrt{\frac{E_b}{N_o}} \circ \frac{R_s(\varepsilon_n) - R_s(1-\varepsilon_n)}{R_s(0)}\} \quad (4.41)$$

where $R_s(\varepsilon_n)$ is the autocorrelation function of the input waveform. For random NRZ input we have

$$R_s(\varepsilon_n) = \begin{cases} 1 - |\varepsilon_n| , & |\varepsilon_n| < 1 \\ 0, & |\varepsilon_n| \geq 1 \end{cases} \quad (4.42)$$

By substituting Eq. (4.42) into (4.41) we obtain for the bit error probability for a given ε_n

$$P_e(\varepsilon_n) = \frac{1}{4}\,\mathrm{erfc}(\sqrt{\frac{E_b}{N_o}}) + \frac{1}{4}\,\mathrm{erfc}[\sqrt{\frac{E_b}{N_o}}\,(1-2|\varepsilon_n|)] \quad (4.43)$$

The expected bit error probability is obtained by averaging $P_e(\varepsilon_n)$ over ε_n to obtain

$$P_e = \int_{-1}^{1} P_e(\varepsilon_n)\, p(\varepsilon_n)\, d\varepsilon_n, \tag{4.44}$$

where $p_e(\varepsilon_n)$ is given by Eq. (4.40).

In the simulation, we specify the normalized standard deviation σ_e in Eq. (4.40) as an input parameter, and with this value, we compute Eq. (4.44) by numerical integration. All other quantities involved in Eqs. (4.40), (4.43) and (4.44) are known or previously computed. That way we directly obtain the bit error rate will specified clock timing errors.

5. IMPLEMENTATION OF THE SIMULATION PACKAGE

5.1 Introduction

The simulation package consists of the main program and the subroutine modules which perform the simulation of signal at various points along the channel. The general block diagram is given in Fig. 1.1.

A more detailed flow diagram is shown in Fig. 5.1. The main part of the simulation program is composed of three groups of subroutines, namely

(a) signal generating subroutines

(b) filtering and nonlinear amplifying subroutines

(c) signal decoding and probability of error computation subroutines.

There are also other supplementary subroutines necessary for the simulation. They are

(d) integration subroutines

(e) function subroutines

(f) parameter computation subroutines.

5.2 Operation of the Simulation Package

The simulation package is organized to operate with the set of input parameters stored in input file. The whole simulation can be repeated NLOOP times within one program run. Accordingly, NLOOP is the first parameter in the input file, followed by NLOOP sets of other parameters.

It is possible to bypass certain portions of the program at will.

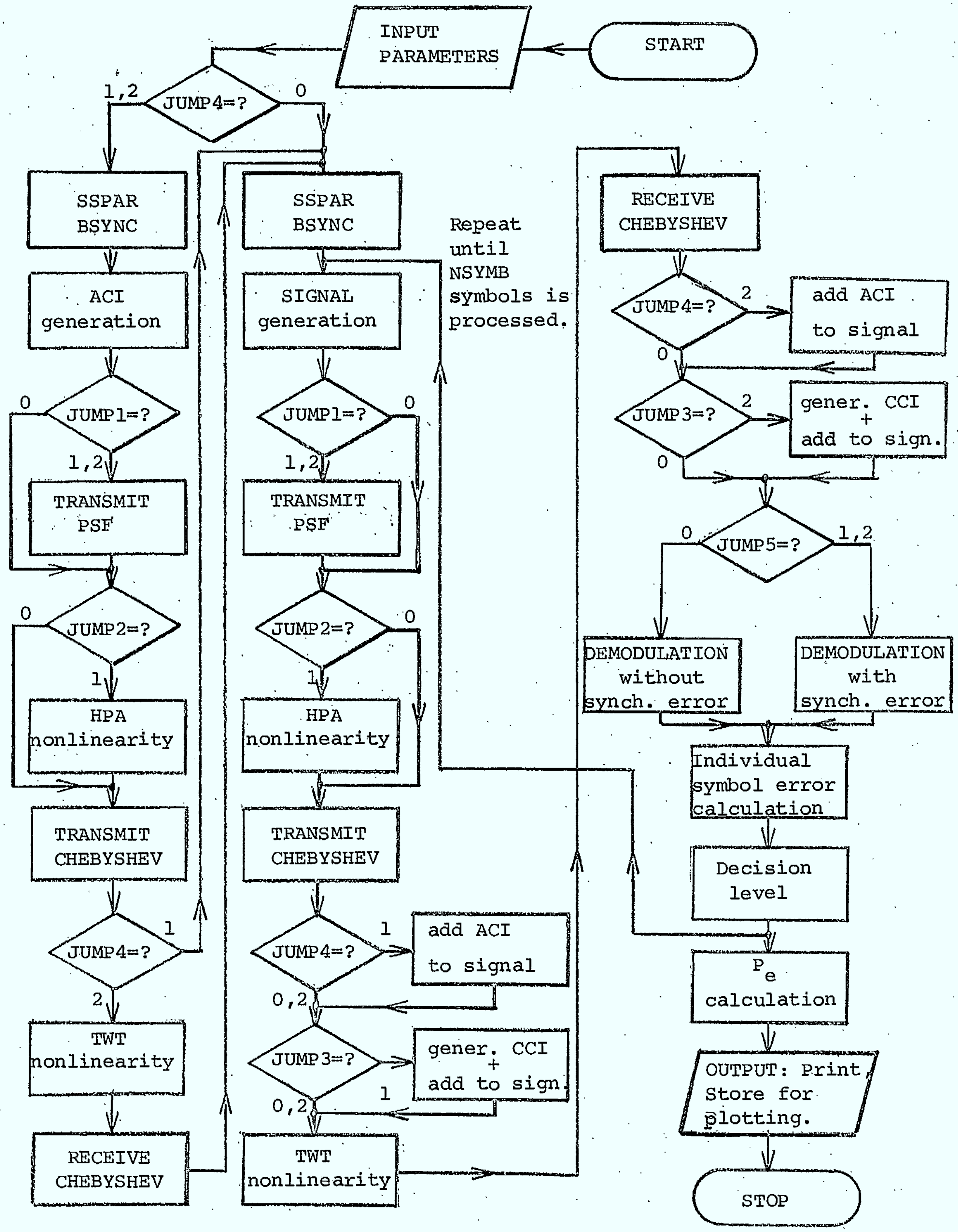

Fig. 5.1 Detailed flow - diagram of the satellite channel simulation package

This can be done by assigning corresponding values to "JUMP" parameters. As can be seen in Fig. 5.1 there are five of these parameters. The role of these parameters and their particular values are described in Table 5.1. With such an organization of the program, it is easy to analyze the influence of the particular channel impairments either separately or in any desired combination, thereby providing a very flexible simulation program.

The main output results of the program are the probability of bit error and the probability of symbol error, both as a function of the receiver filter output bit energy to noise energy ratio (E_b/N_o). The array of specified E_b/N_o values is given in terms of initial E_b/N_o, denoted SNR1, the SNR increment DSNR, and NSNR, the number of points for which the probability of error is to be computed.

Other input parameters are TWIDB and HPIDB, the input operating points of the TWT transponder and high-power output amplifier, respectively. They are specified in decibels of input backoff. The value of 0 dB (saturating point) corresponds to 4.3 mV input voltage for the 261-H TWT transponder and to 10 mV for the Varian Helix TWT-VTC 6660 C2 HPA.

The particular modulation scheme is selected by a particular value for the parameter ITYPE. Correspondence between the value of ITYPE and the modulation scheme is given in Table 5.2. Although types 4 and 5 (16-phase CPSK and 4-phase DPSK) were not included in the proposal, they are retained from the original simulation package [1], and can be used if need arises. An important parameter in the simulation is the product of the filter 3 dB bandwidth and the symbol duration, BT. It alleviates the need to specify both 3 dB bandwidth and the channel symbol rate

Table 5.1 Values of JUMP Parameters

PARAMETER	FUNCTION	VALUE	PARTICULAR FUNCTION
JUMP1	PULSE SHAPING FILTER SWITCH	0	BYPASS P.S.F.
		1	NYQUIST + G. DELAY EQUALIZER
		2	NYQU. + x/sin(x) + G. DEL. EQUAL.
JUMP2	HPA SWITCH	0	BYPASS HPA
		1	HPA PROCESSING
JUMP3	CCI SWITCH	0	BYPASS CCI
		1	CCI AT INPUT OF UPLINK FILTER
		2	CCI AT OUTPUT OF DOWNLINK FILTER
JUMP4	ACI SWITCH	0	BYPASS ACI
		1	ACI AT INPUT OF UPLINK FILTER
		2	ACI AT OUTPUT OF DOWNLINK FILTER
JUMP5	SYNCH. SWITCH	0	NO SYNCHRONIZATION ERROR
		1	CARRIER SYNCHRONIZATION
		2	SYMBOL SYNCHRONIZATION

separately, and makes the comparative analysis more general. Presently, only one value of BT is specified for all the filters in the satellite link, so as to minimize the number of input parameters. However, it is a simple matter to specify separate BT products, if it becomes necesary.

ITYPE	1	2	3	4	5	6	7	8	11	12	13	18
Mod. Schem	2-ϕ	4-ϕ	8-ϕ	16-ϕ	4-ϕ	2-ϕ	offset		2-ϕ	4-ϕ	8-ϕ	FFSK
	CPSK	CPSK	CPSK	CPSK	DPSK	DPSK	PSK	FFSK	differential encoding			

As mentioned in Section 4.3, two types of detectors are used. It was mentioned that the IDF is the optimum filter when the PSF is not present, and that the PVD yield somewhat better performance when the PSF is included. To allow any combination of filters and detectors, a separate input parameter is included, which gives the option between two types of detectors. When ISYNC = 0, the IDF is selected while the value of 1 selects the PVD, independent of the value of JUMP1. Also, when the PSF is included in the link, the presence of the non-minumum phase all-pass network causes time advance of the signal. It is therefore necessary to introduce an intentional delay to compensate for this advance, and it can be done by giving a number of delayed symbols as a value for the input parameter IDELAY. The value of 4 or 6 will suffice for any value of the PSF rolloff factors ALPHT (for transmitter PSF) and ALPHR (for receiver PSF).

Rolloff factors ALPHT and ALPHR are used only when the option with PSF is chosen (JUMP1 = 1 or 2). They should be specified (as dummies), however, even where this is not the case, so that the input file is correctly read by the program. This is also true for the other optional parameters, such as HPIDB mentioned before, and for the parameters of the CCI and ACI signals, and synchronization parameters. For the CCI, we specify the input signal-to-CCI-ratio in dB, SCCIR, number of CCI tones, KCC (up to 10) and the array FCC(KCC) which specify the positions of the tones on the frequency-scale in terms of percentage power of the useful signal. The program computes these positions in terms of FFT array indices and outputs these indices. When the ACI is included in the simulation, AATNDB is the signal-to-ACI-power ratio in dB before the ACI is filtered through the main channel filters. The corresponding ratio, after filtering is performed, is the programs output result. We also specify the separation, CHSEP, between the carriers, as indicated in Fig. 3.7. The maximum value for CHSEP (=2.0) corresponds to the separation equal to the total FFT length, i.e., to 4096 complex frequency samples. The actual value for CHSEP is given in fractions of this length. An option is also provided for the separate BT product for the adjacent channel filters, and is specified by the parameter BTINT.

Finally, two parameters determine the phase-locked-loop (PLL) bandwidths, for the calculation of synchronization erros. When the carrier synchronization is treated (JUMP5 = 1), BTL2 is the PLL bandwidth factor for the BPSK, and BTL4 is the corresponding factor for the QPSK. As noted before, both BTL2 and BTL4 are used for the offset PSK and FFSK. In the symbol synchronization case (JUMP5 = 2) BTL2 is the standard deviation for the symbol synch error normalized with respect to the symbol duration, and BTL4 is a dummy.

Since the plotting of the simulation results is dependent on the actual computer system, being used, it was decided that plotting not be included in the main simulation program. Instead, the arrays to be plotted are written in binary format on the separate output files, so that the separate programs read these arrays, process them, and plot them. It is particularly convenient to do so on the HP 1000 minicomputer, because its plotting software requires a significant amount of storage and cannot be incorporated in the simulation package which, by itself, is memory consuming.

Besides the arrays of probability of error versus E_b/N_o, program also stores for plotting the signal spectra at various points in the channel. These spectra are identified by a value of the parameter IDENT which is also written on the output file, thus enabling the identification of the written spectra when they are read off by the plotting program. Chapter six will provide examples of the various types of results which can be obtained from the program.

Note: The user's package for plotting signal power spectra should provide the following two parameters:

NPOINT: number of complex spectral points for drawing (maximum 4096). This way, only the desired portion of spectrum will be plotted, instead of the whole spectrum, enabling the user to truncate small sidelobes toward the end points, and to emphasize the main lobe and the first few sidelobes.

NSMOOT = number of spectral points averaged. If, for example, NSMOOT=9, then the k-th plotted spectral value is the average of 9 neighbouring values, k-4, k-3, ..., k, ... k+3, k+4. This way, spectral plots become less peaky.

6. SIMULATION RESULTS

6.1 General

In this chapter we shall discuss the results of the simulation of digital modulation schemes for communication over satellite channels using the program described in the preceding chapters.

Unless otherwise specified, all simulations were performed using four-pole 1/2 dB ripple Chebyshev filters in both the uplink and downlink channels. As an approximation to Nyquist cosine rolloff filters, Butterworth filters of order four are used in both transmitter and receiver as pulse-shaping filters (PSF) combined with second-order all-pass delay equalizers. Inclusion of an x/sin(x) amplitude equalizer is optional. The satellite TWT transponder was modelled as a Hughes 261-H tube, and a Varian Helix TWT-VTC 6660 C2 ser. 106 was used as a transmitter earth station high-power amplifier (HPA). For most of the simulations, the pulse-shaping rolloff factor was set to $\alpha = 0.3$ in both transmitter and receiver pulse-shaping filters, while the operating points of the TWT and HPA were set to 0 dB and 6 dB of input backoff, respectively.

When the PSF's are not included in the simulation, detection is performed by using an integrate- and- dump filter (IDF), whereas when they were included, a peak value detector (PVD) was used. With the PSF-s present in the simulation, the signal stream must be delayed by IDELAY symbols in order to compensate for the advance introduced by an all-pass network. Usually, a delay of 2-3 symbols is sufficient, and a value of 4 is chosen for all simulations, so as to compensate for all possible cases. Any value larger than that and smaller than LSKIP (=20) yields identical simulation results.

When the simulation includes only the Chebyshev filters and the transponder TWT nonlinearity, the case encompassed in the previous simulation reported in [1], we refer to it as the basic channel case. The "JUMP" parameters, described in the previous chapters, are all equal to zero in that case.

The effects of various channel improvements on the system performance are illustrated for the coherent QPSK modulation scheme, since it is the most frequently used in satellite communications. The other modulation types are simulated for some selected channel parameters, and comparisons are made with the QPSK case. Performance evaluations were primarily made using probability of bit error, P_{be} versus bit-energy-to-noise ratio, E_b/N_o. Another form of evaluation used is the presentation of the signal spectra at various points in the channel. In the P_{be} vs. E_g/N_o diagrams, E_b/N_o was varied from 0 dB to 20 dB in 0.5 dB steps. The minimum P_{be} is limited to 10^{-6} in these diagrams, although smaller values are displayed in the output printed results. For convenience, the power spectral densities are plotted versus the normalized frequency, $(f-f_c)T$, which ranges from -2.0 to +2.0. Magnitudes of the spectra are plotted in dB, normalized to the peak value.

6.2 Coherent 4-phase CPSK

6.2.1 Basic Channel

Simulation runs were performed for various BT products. Figure 6.1 shows the probability of bit error versus bit energy-to-noise ratio, E_b/N_o, for the basic channel, when the TWT transponder is in saturation. Performance degradation increases steadily with decreasing BT. Similar behaviour is noticed from the curves in Fig. 6.2 where the probability of bit error is plotted for the case where the TWT transponder operates at 14 dB input backoff, and is essentially in the linear region. However, as the BT product approaches unity, the performance of the system at saturation when E_b/N_o is high is seen to be slightly better than the performance of the system in the linear region. One reason is that at saturation, the incidental modulation phase due to amplitude variation is not as severe as when the TWT is operating linearly.

6.2.2 Pulse Shaping Filters and HPA Nonlinearity

Figures 6.3 and 6.4 show the transmitted power spectral densities (PSD), and the PSD's at the receive filter outputs for 0 dB and 14 dB TWT input backoff, respectively. We see that the saturated system tends to regenerate higher sidelobes than the system operating in the linear region.

The effects of the PSF on the system performance is illustrated in Fig. 6.5 where BT=1, and the TWT transponder is operating in the linear region. The solid curve (A) shows the performance of the basic channel for comparison. When the PSF only is included in transmitter and receiver, the performance improves by about 1 dB (B). By adding an HPA nonlinearity in the channel, the performance degrades only by a fraction

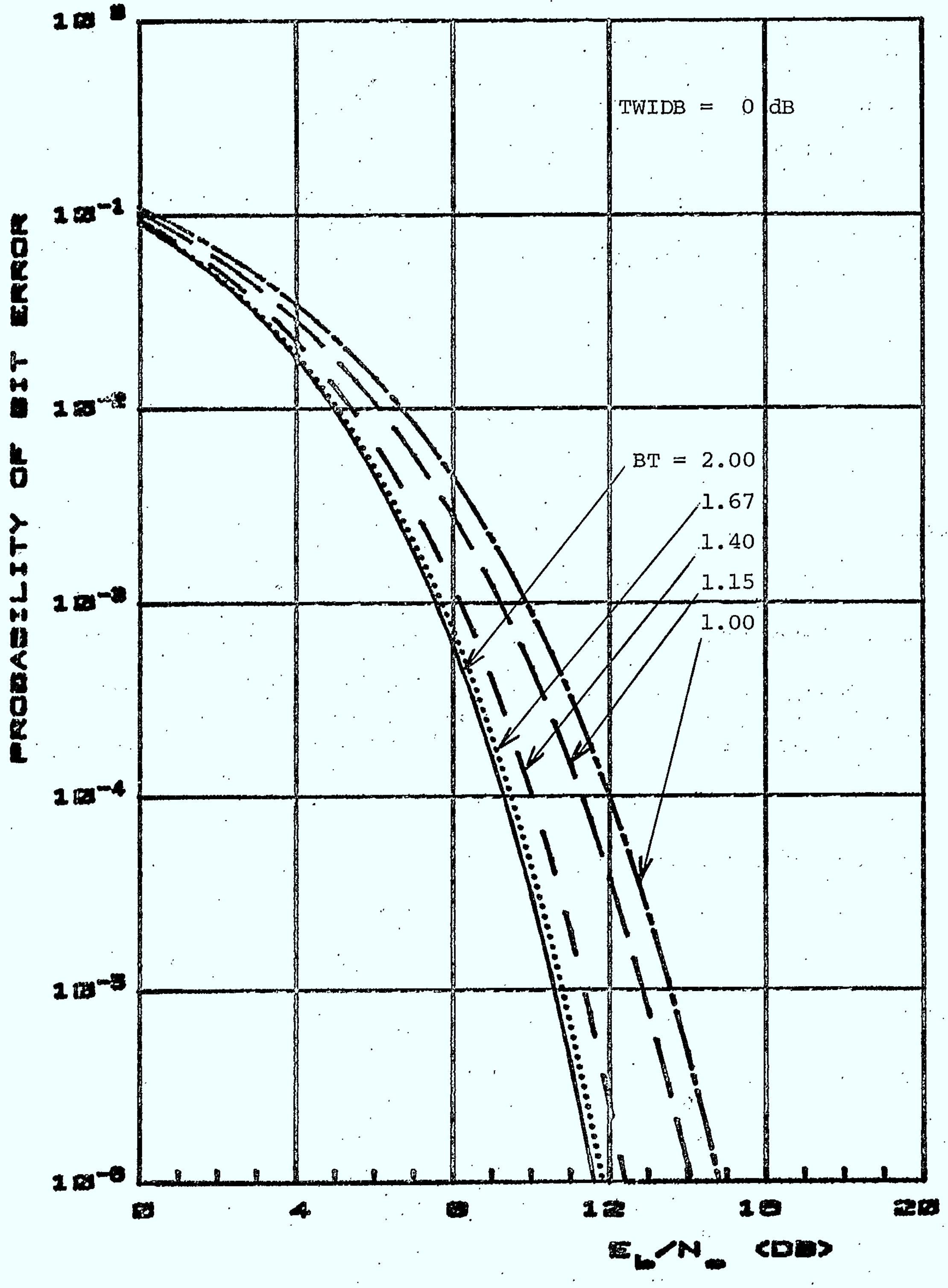

Fig. 6.1 P_e versus E_b/N_o for 4-phase CPSK. Basic channel, TWIDB = 0 dB.

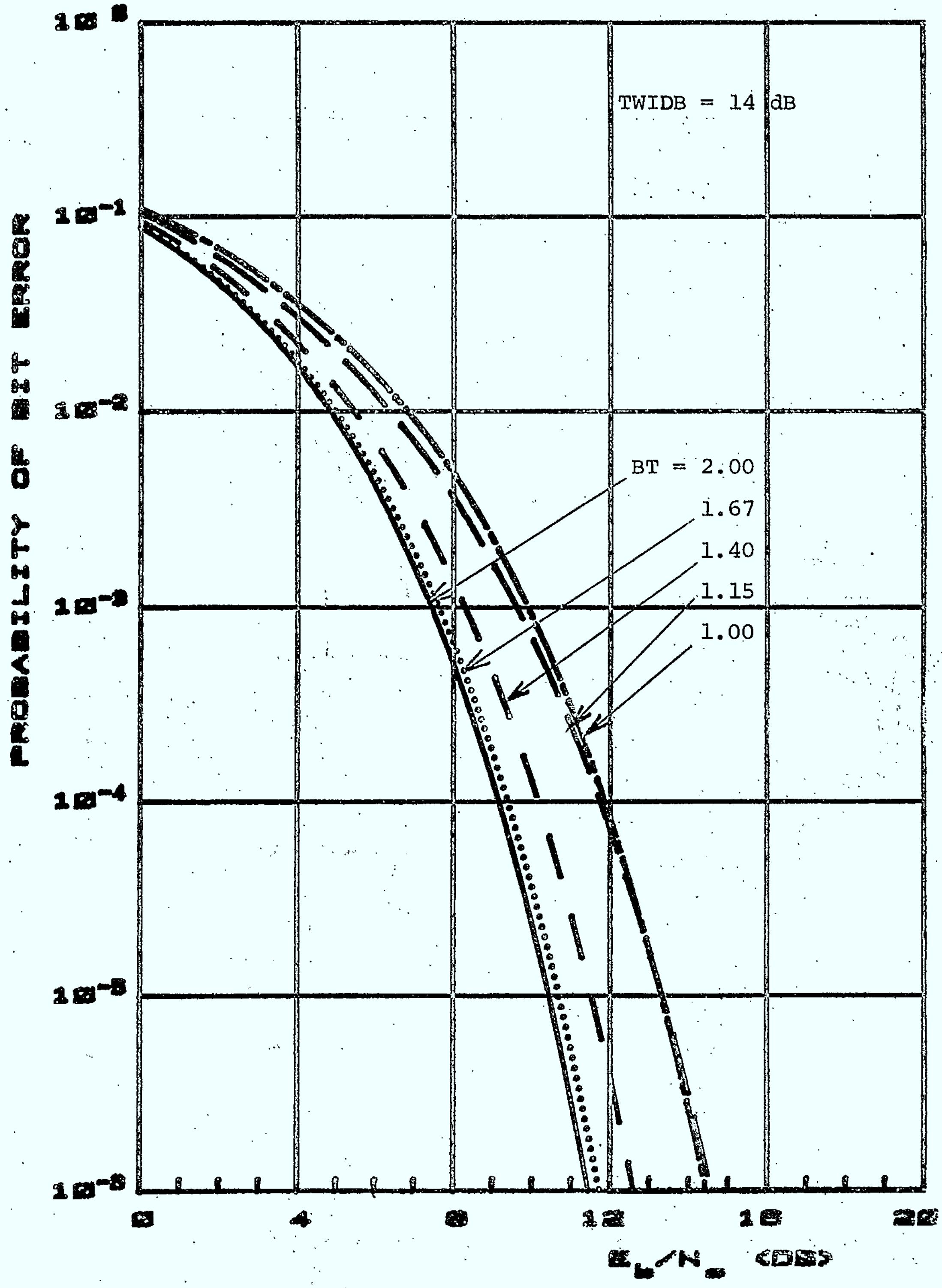

Fig 6.2 P_e versus E_b/N_o for 4-phase CPSK. Basic channel, TWIDB = 14 dB.

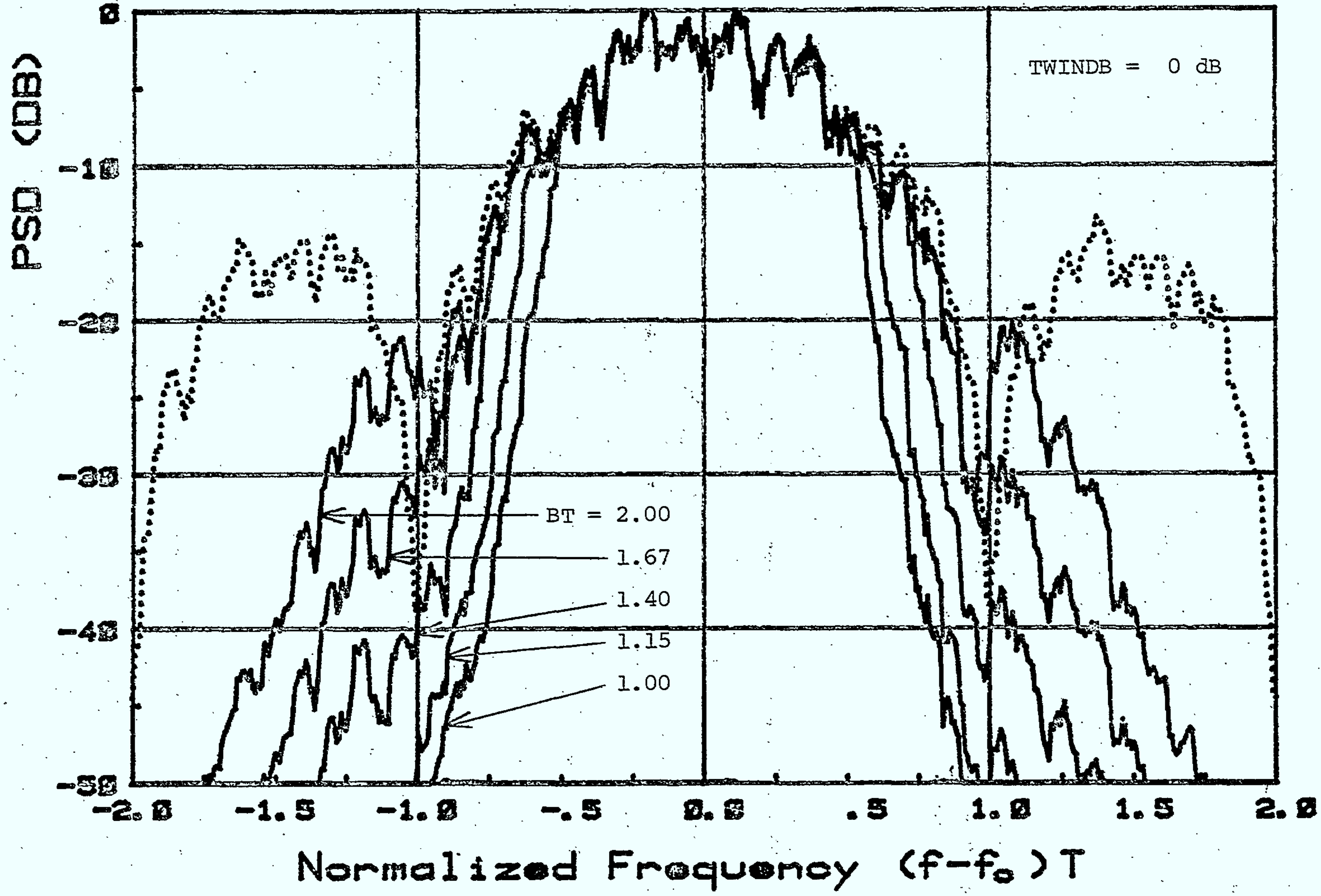

Fig 6.3 Transmitted signal PSD (•••••), and PSDs at the receive filter output for 4-phase CPSK. Basic channel, TWIDB = 0 dB.

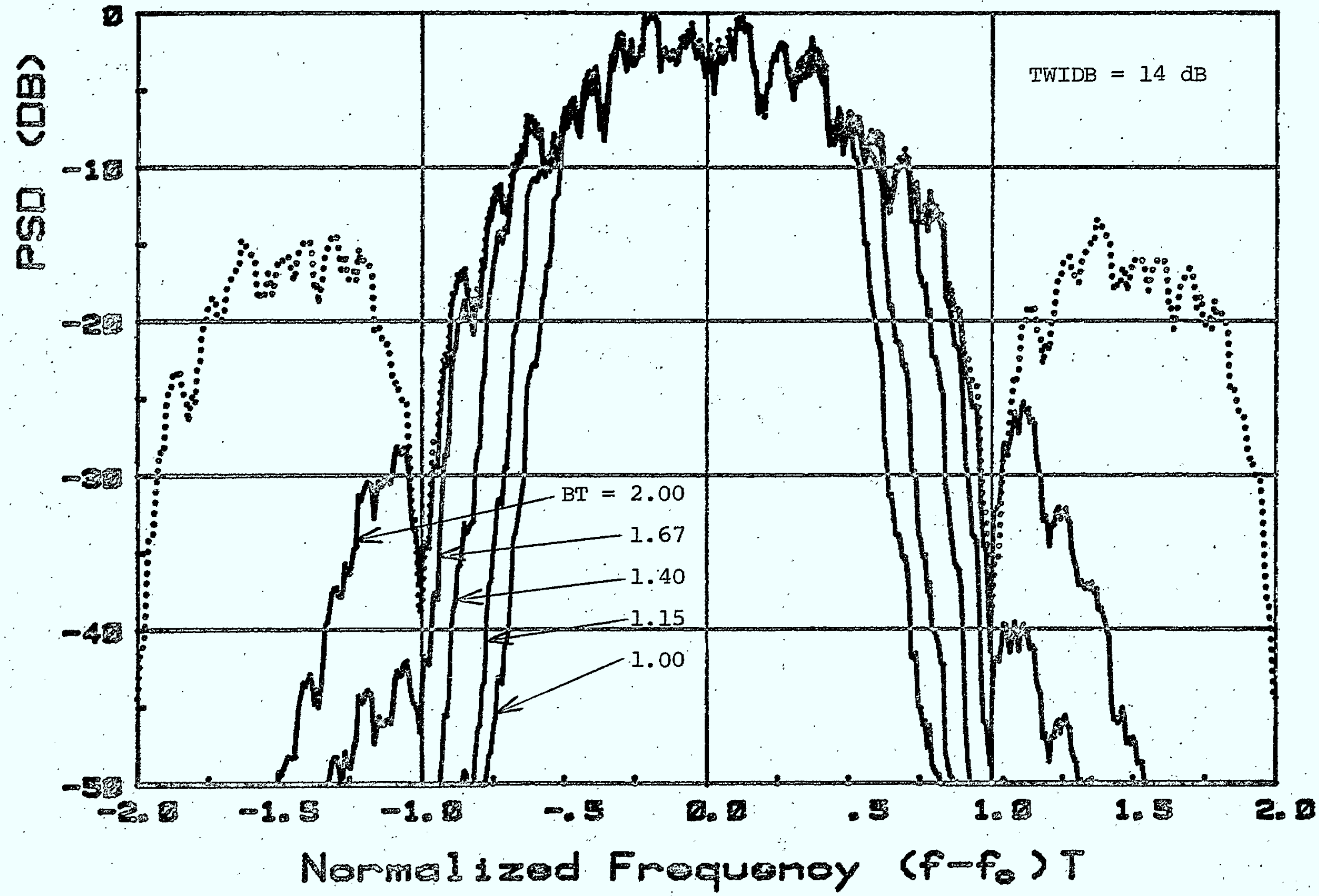

Fig 6.4 Transmutted signal PSD (•••••), and PSDs at the receive filter output for 4-phase CPSK. Basic channel, TWIDB = 14 dB.

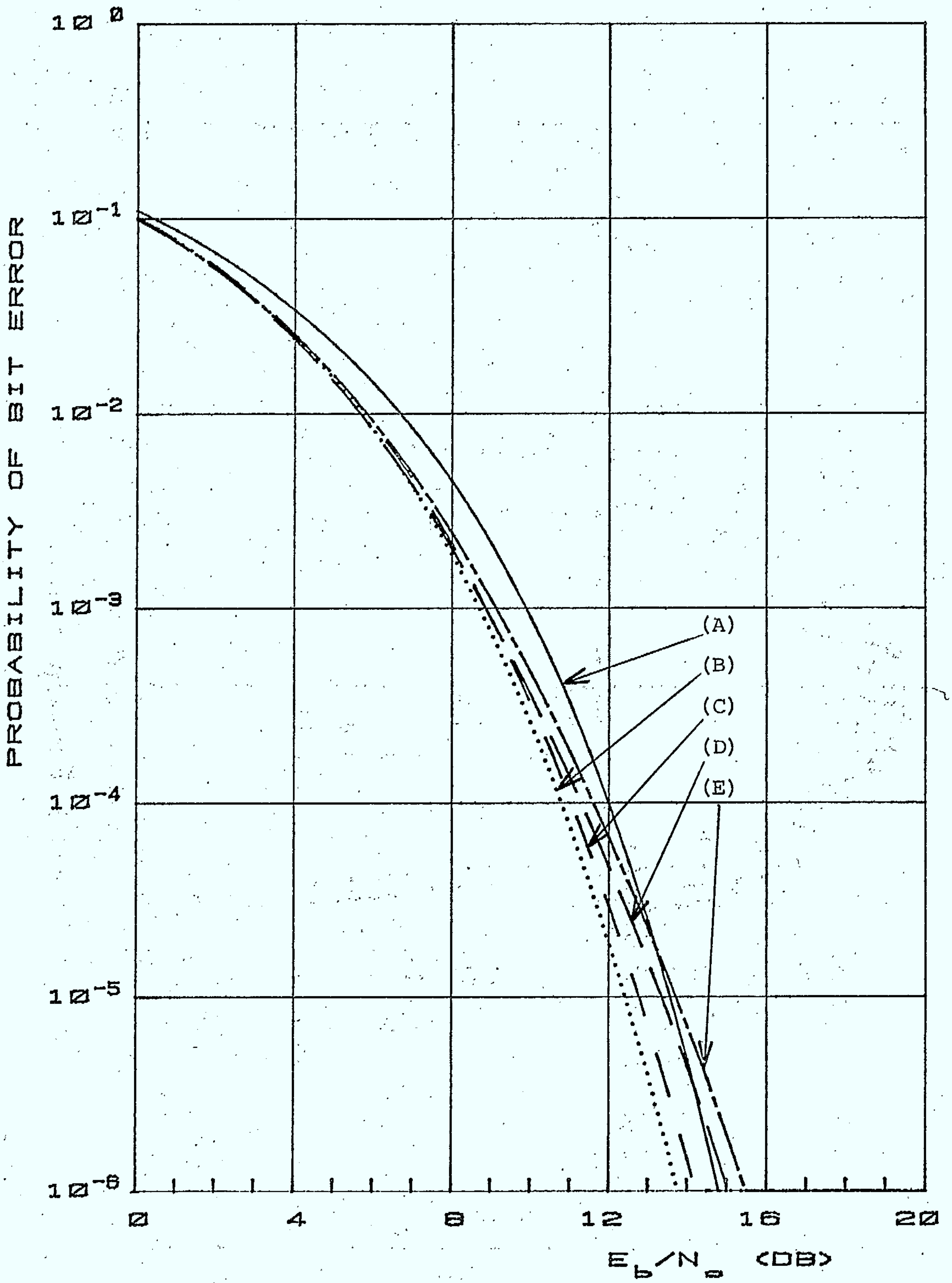

Fig 6.5 P_e versus E_b/N_o for 4-phase CPSK, BT=1., TWIDB = 14 dB.
(A) basic channel; (B) PSF, no x/sin(x), PVD;
(C) HPA (HPIDB = 6 dB) + PSF, no x/sin(x), PVD;
(D) HPA (HPIDB = 6 dB) + PSF, with x/sin(x), PVD;
(E) HPA (HPIDB = 6 dB) + PSF, with x/sin(x), IDF.

of a dB (C). Cascading of the x/sin(x) amplitude equalizer to a PSF slightly worsens the performance at high values of E_b/N_o (D). One reason is that the peak of the x/sin(x) equalizer emphasises the spectral content in the vicinity of the carrier frequency. Finally, we included the probability of error curve (E) for the case when the IDF is used for symbol detection instead of the PVD. The comparison of curves (D) and (E) shows that the latter one is slightly less than 0.5 dB worse than the former, when E_b/N_o is high.

The transmitted (T) and the received (R) spectra for the above cases are shown in Fig. 6.6. We see that, when the PSFs are included in the channel, the received spectra are practically independent of the presence of the x/sin(x) equalizer and the HPA nonlinearity; curves (B,C,D and E) for the receiver overlap almost completely.

The influence of the HPA operating point is presented in Figs. 6.7 and 6.8. Figure 6.7 shows the probability of bit error for the channel with PSF and HPA with 14 dB input backoff (solid curve) and 0 dB input backoff (dotted curve). The corresponding PSDs are shown in Fig. 6.8. We see that the performance of the system with a saturated HPA is practically the same as that of the system with linear operating point.

Figure 6.9 shows the probability of bit error vs. E_b/N_o with HPA and PSF for various values of the rolloff factor α. The value of 0.3 for the rolloff factor in both transmitter and receiver PSFs gives somewhat better performance than the other values. However, the total change in the performance degradation, for the examined range of α, does not exceed 1 dB. The transmitted signal PSD (dotted curve) and the received signal PDSs for the values of α used in Fig. 6.9 are shown in Fig. 6.10. Gradual decreasing of spectral width with increasing α is

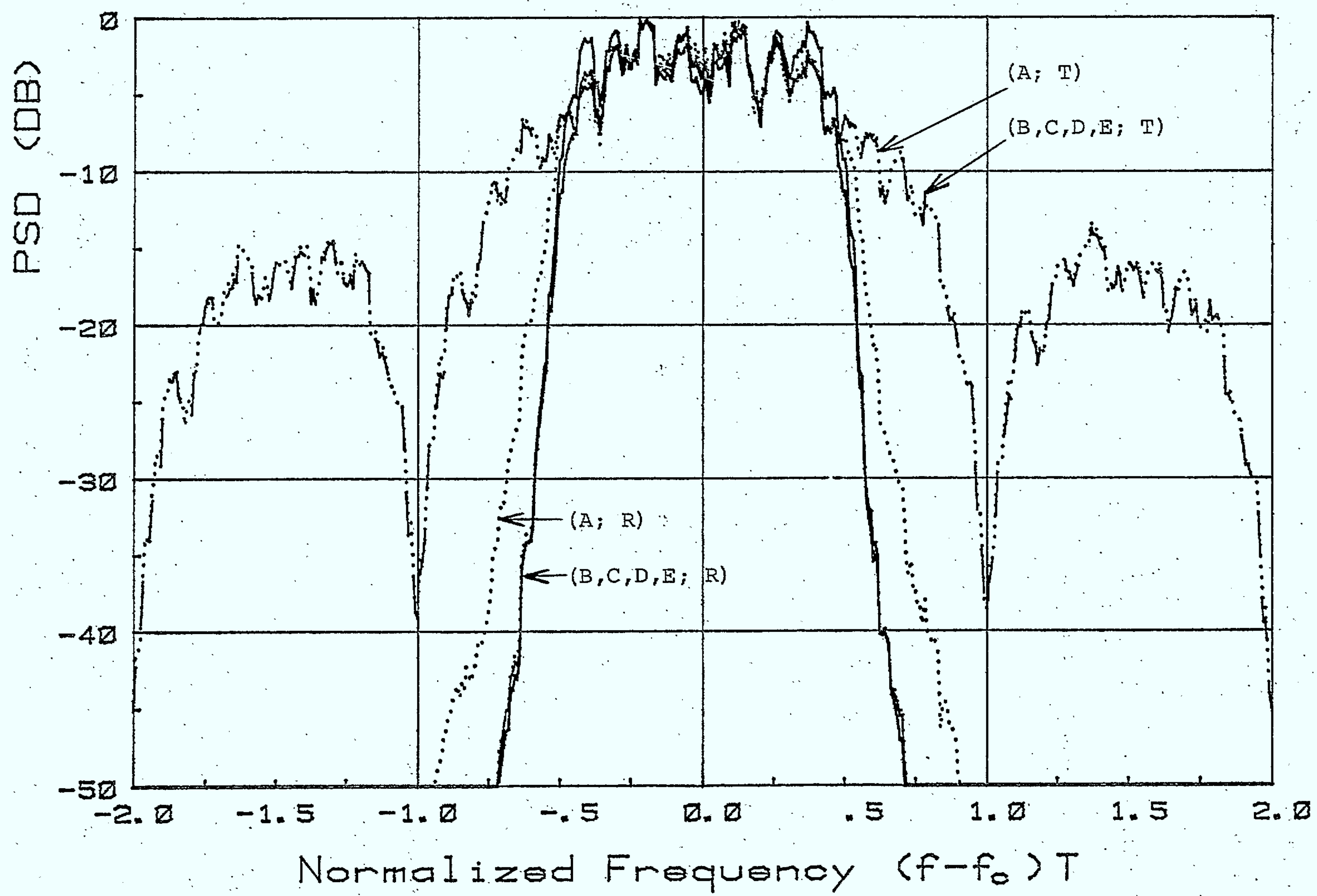

Fig. 6.6 Transmitted signal PSDs (T), and PSDs at the receive filter output for 4-phase CPSK (R); the cases (A), (B), (C), (D), and (E) correspond to those in Fig. 6.5.

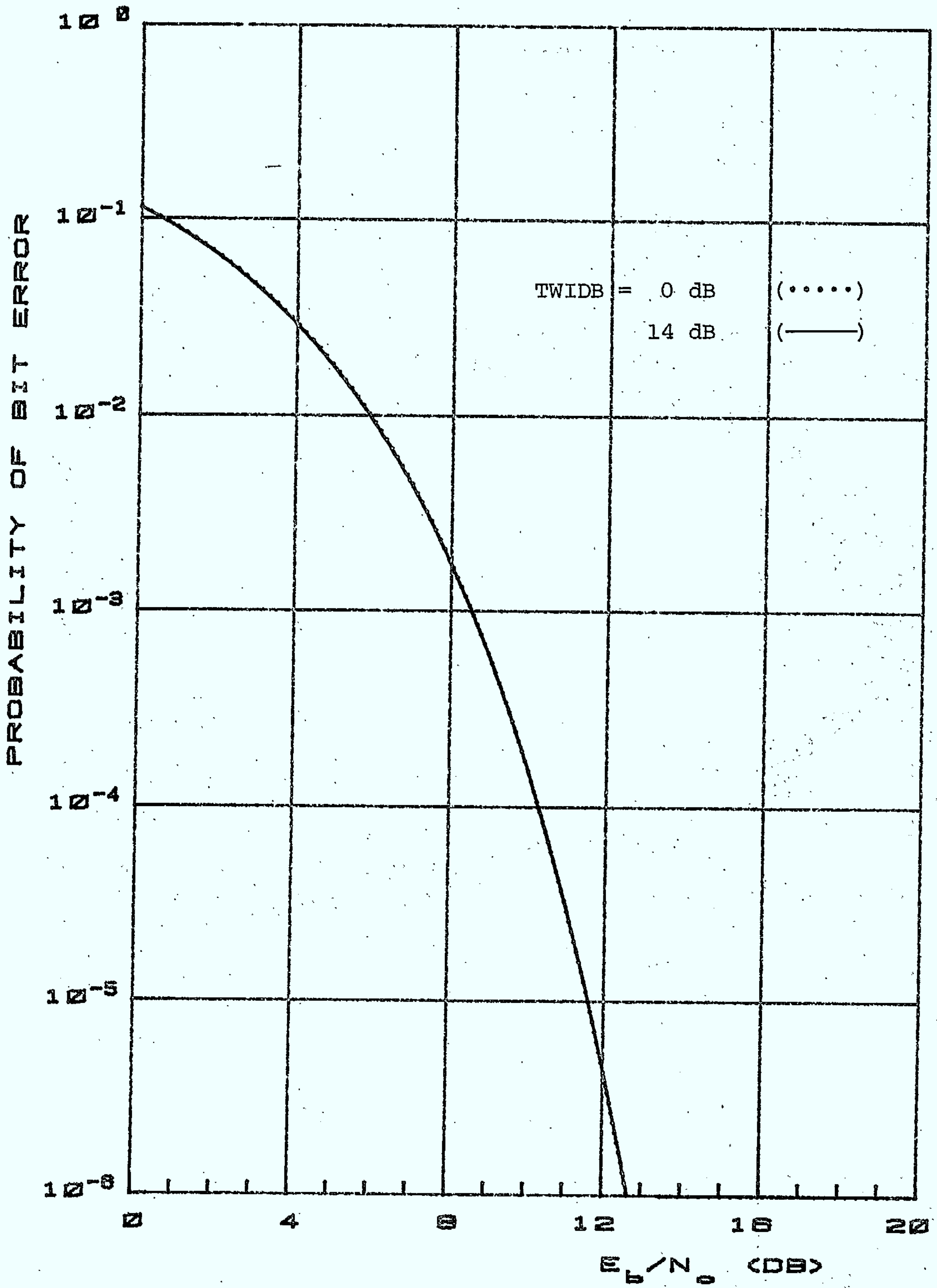

Fig. 6.7 P_e versus E_b/N_o for 4-phase CPSK with HPA and PSF;
(———) HPIDB = 14 dB;
(••••••) HPIDB = 0 dB.

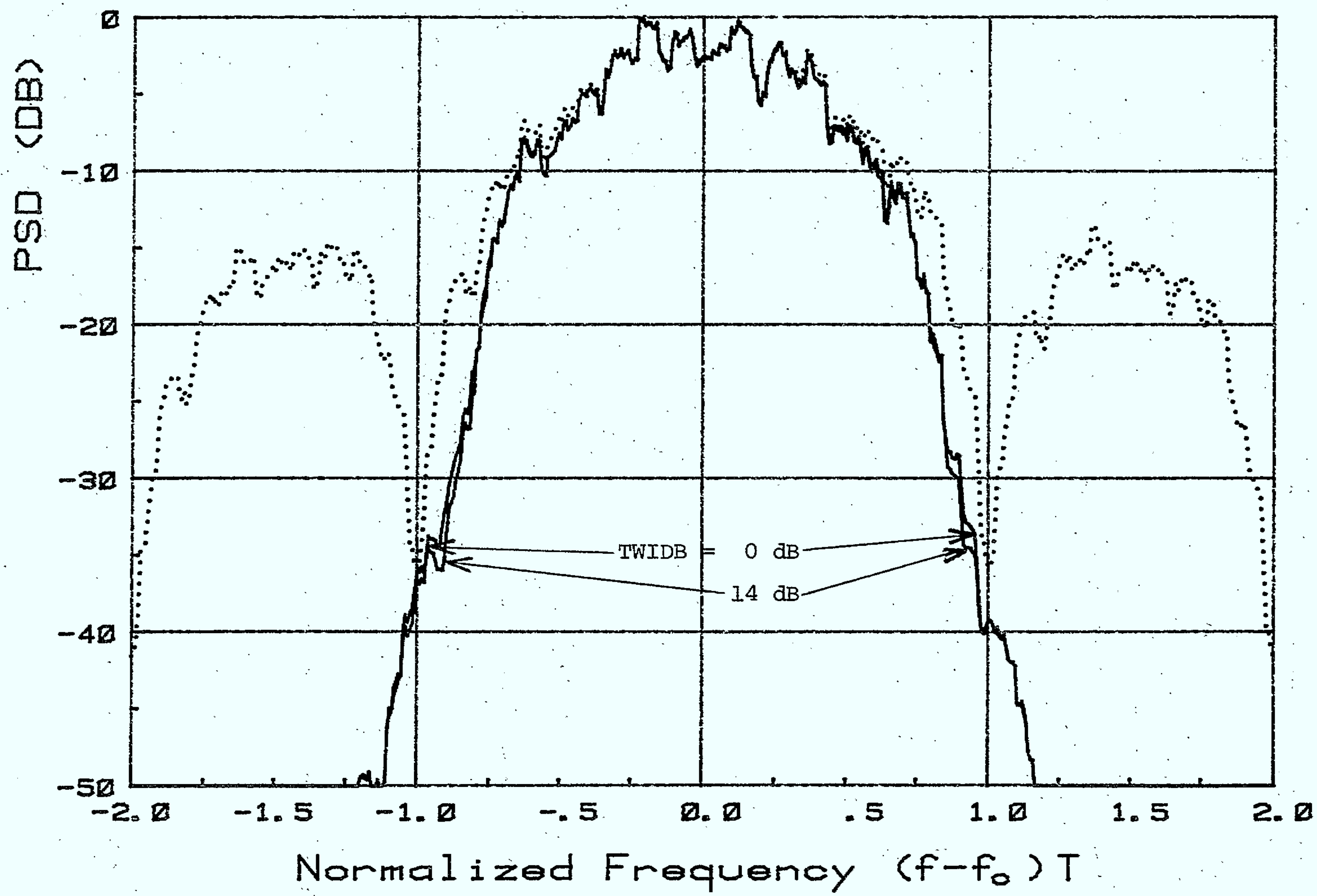

Fig. 6.8 Transmitted signal PSD (·····), and PSDs at the receive filter output for 4-phase CPSK with HPA and PSF.

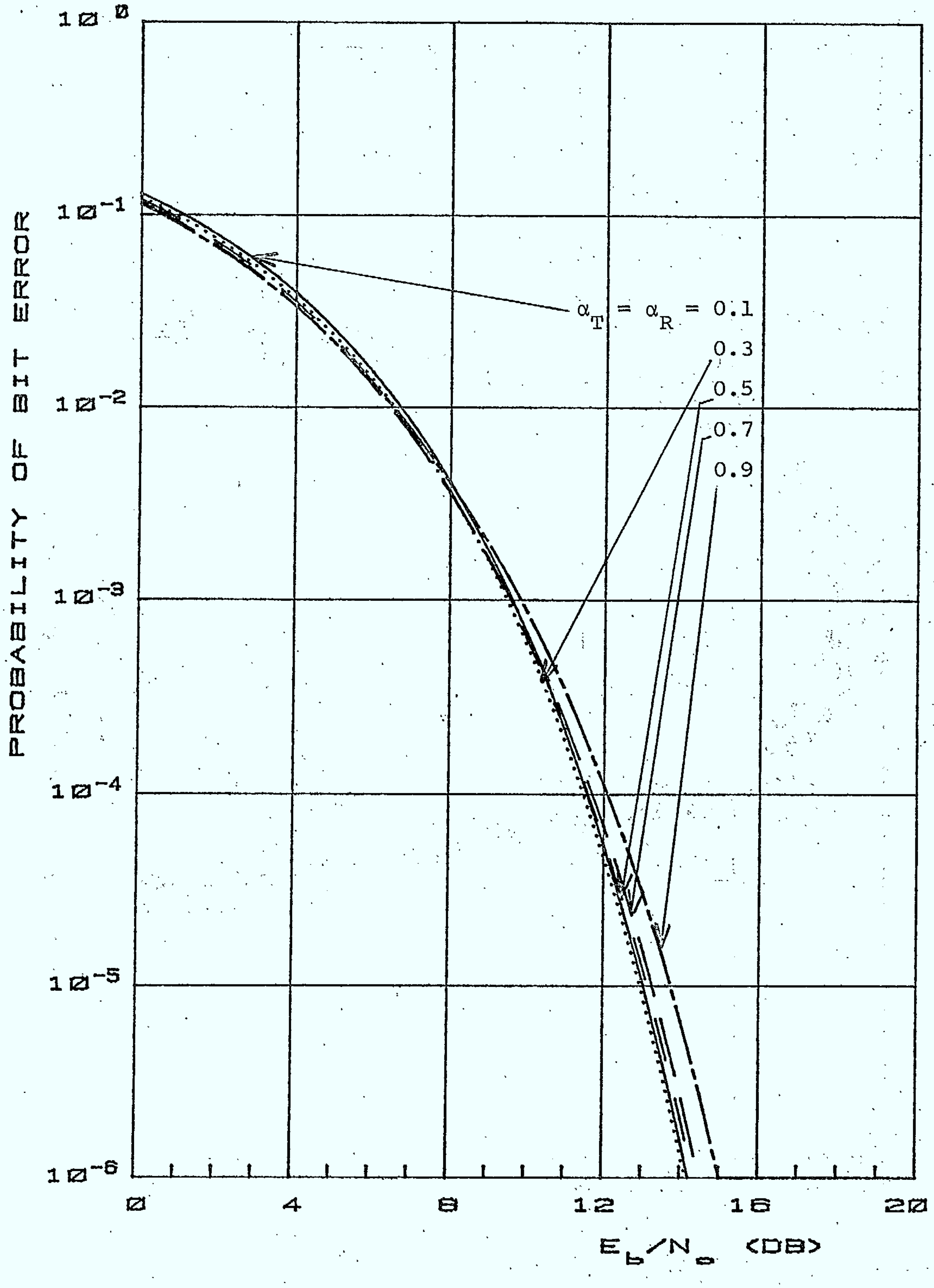

Fig. 6.9 P_e versus E_b/N_o for 4-phase CPSK with HPA and PSF with 5 values for rolloff factor α_T $(=\alpha_R)$.

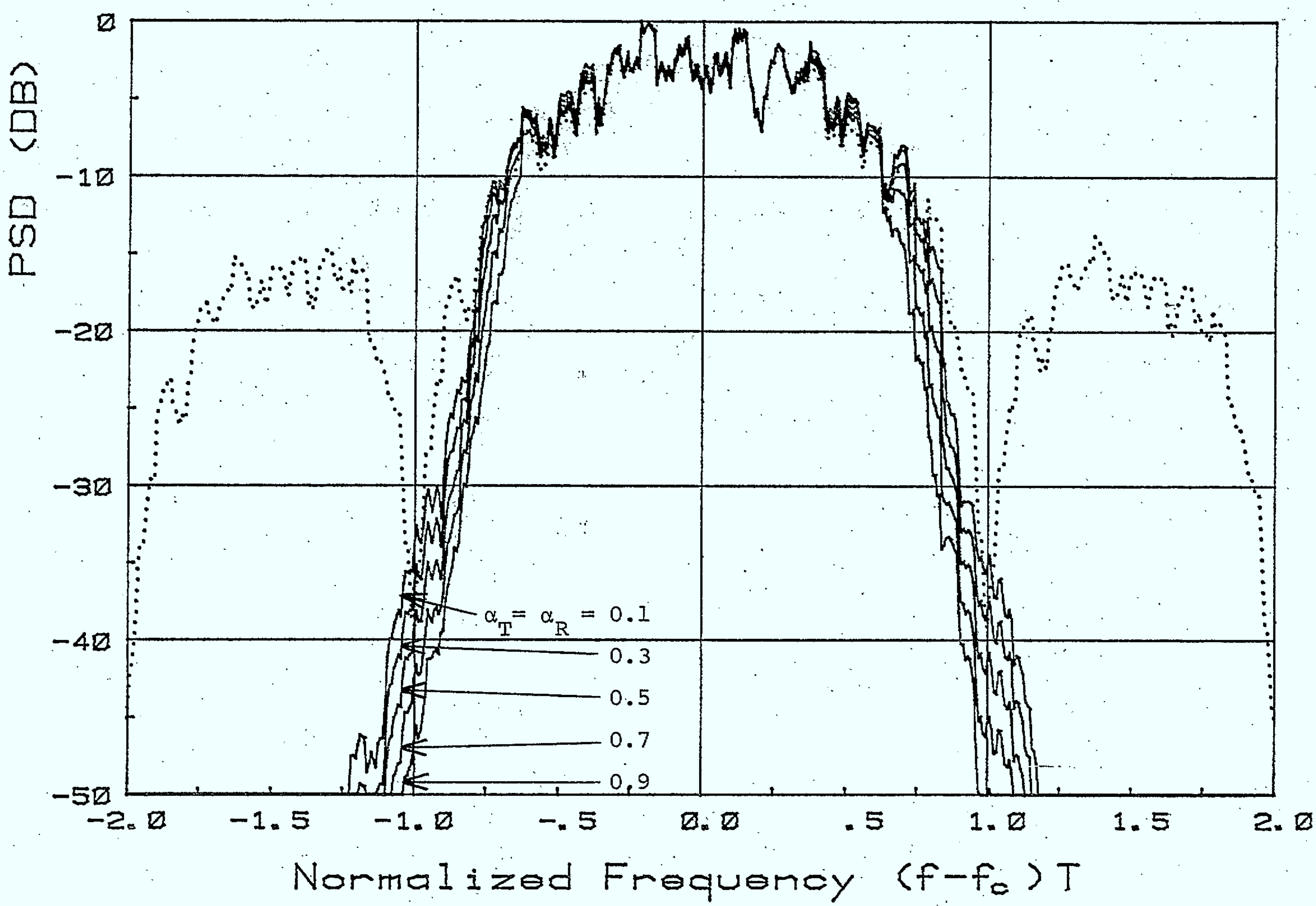

Fig. 6.10 Transmitted signal PSD (•••••), and PSDs at the receive filter output for 4-phase CPSK with HPA and PSF with 5 values for rolloff factor α_T $(=\alpha_R)$.

apparent.

6.2.3 Cochannel and Adjacent Channel Interferences

Cochannel Interference (CCI) is modeled by one or more sinusoidal tones added to the channel signal. The number of CCI tones is specified by the parameter KCC (maximum 10) and the overall signal-to-CCI ratio is specified by SCCIR. The power of each CCI tone is then 1/KCC times the total interference power. The input array FCC contains the positions of the CCI tones, normalized to the fraction of the total signal power. For example, the value of FCC(1) = 0.15 places the first CCI tone at that frequency f_1 of the signal spectrum, which has the property that the energy contained in the region between carrier frequency f_c and the frequency $f_c + f_1$ is 15 percent of the total signal energy.

The effect of one CCI tone positioned at FCC = 0.25 with various strengths relative to the transmitted signal, incorporated in the channel with the PSFs and HPA, is given in Fig. 6.11. We see that the performance degrades rapidly when the CCI tone is less than 10 dB below the signal. When the SCCIR is 0 dB the probability of error is determined solely by the intersymbol interference, Figure 6.12 shows the received spectra for the same CCI conditions. With the value of SCCIR = 0 dB the CCI tone is easily distinguishable. The finite width of the CCI spectral line in Fig. 6.12 is due to the 9 point averaging used in the PSD plotting.

Figure 6.13 shows the system performance in the presence of several CCI tones. In each case, the total SCCIR is equal 10 dB, so that with the increasing KCC, the individual CCI tone powers decrease. We observe that the worst performance is obtained when the number of CCI tones is

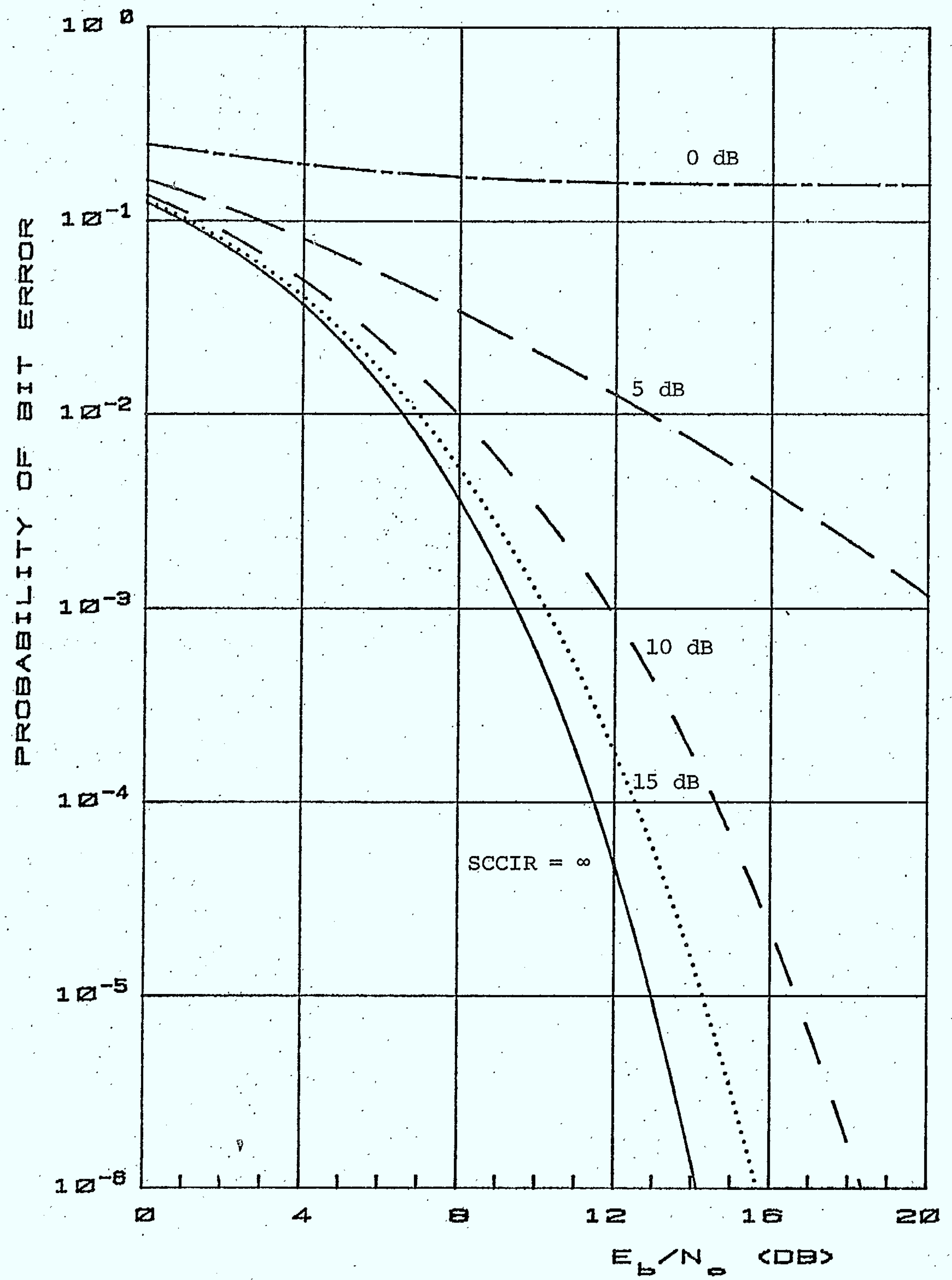

Fig. 6.11 P_e versus E_b/N_o for 4-phase CPSK with one CCI tone added. Solid curve is for case of no CCI.

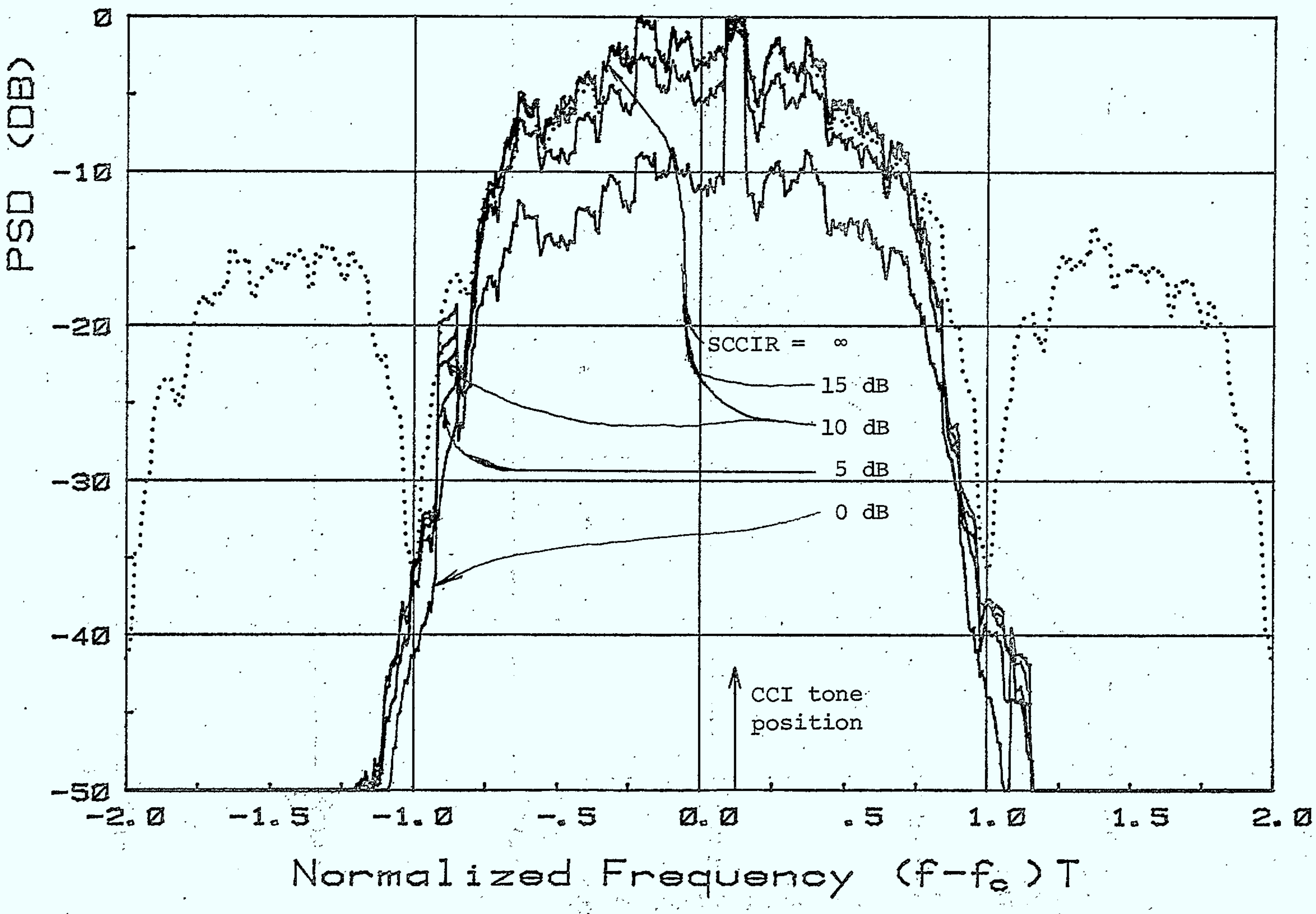

Fig. 6.12 Transmitted signal PSD (•••••), and PSDs at the receive filter output for 4-phase CPSK with one CCI tone (position indicated bu an arrow).

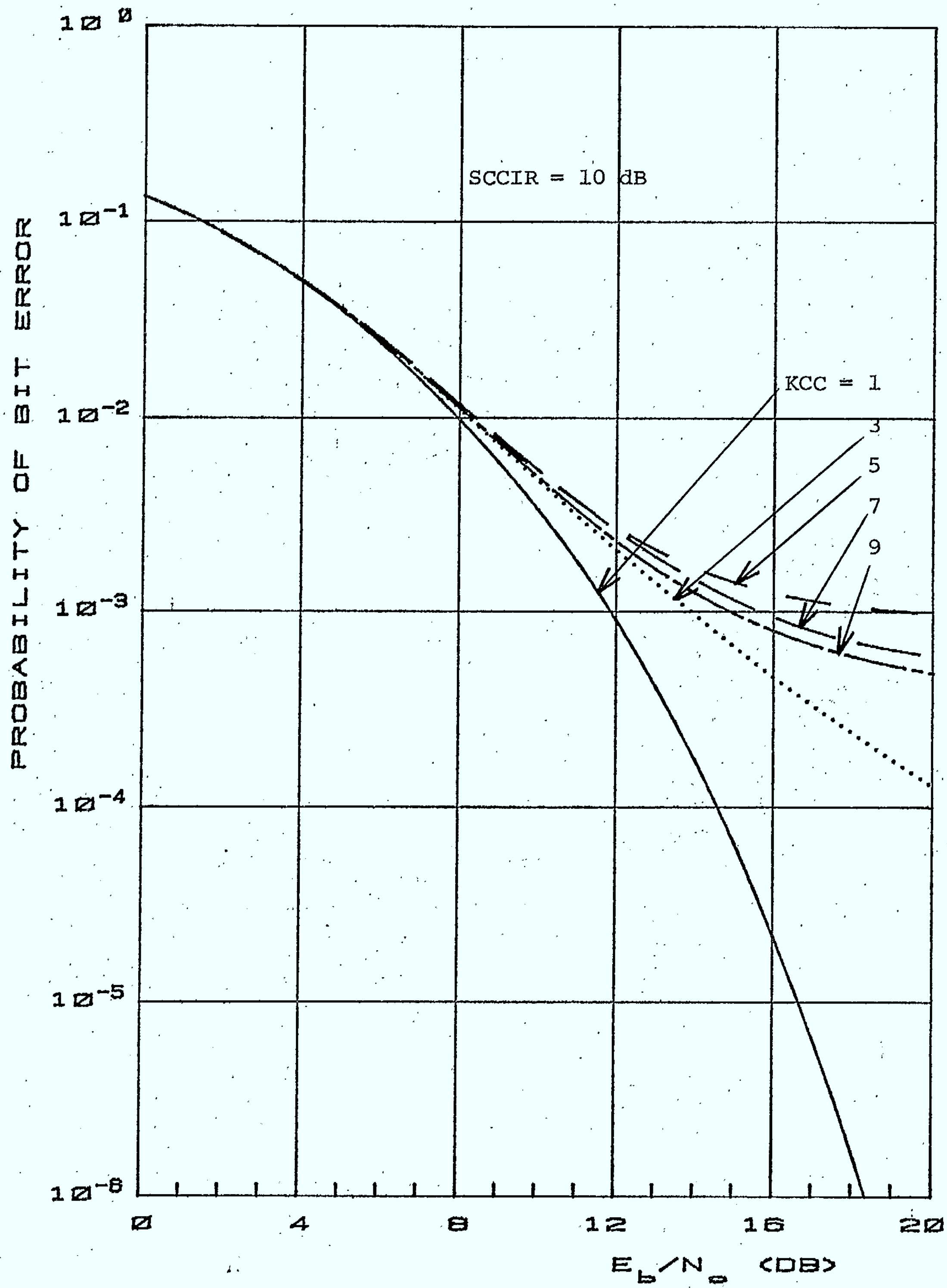

Fig. 6.13 P_e versus E_b/N_o for 4-phase CPSK with different numbers of CCI tones added.

somewhere in the middle of the tested range, i.e., when KCC = 5. Variations in the receiver output PSDs are not significant in this case, as can be seen in Fig. 6.14.

Addition of adjacent channel interference (ACI) further degrades the channel performance. Simulations are run with both CCI and ACI present, the only CCI tone being positioned at 25% of the total signal energy with SCCIR=15 dB. Separation between the useful and interfering channel is held at 0.1, and the attenuation of the ACI with respect to the signal is varied. Curve (A) in Fig. 6.15 (solid curve) shows the performance with the CCI tone only. The remaining curves show the performance degradation when the ACI is attenuated by 6 dB (A), 3 dB (C) and 0 dB (D). The overall degradation is not significant due to the efficient filtering of the ACI. The signal-to-ACI ratios at the receiver filter output for the cases (B), (C), and (D) in Fig. 6.15 are 34.7, 28.9 dB, and 22.9 dB, respectively.

The solid curve in Fig. 6.16 shows the shape of the tails of the ACI PSD with respect to the main channel (dotted curve). Since each curve is individually normalized to its maximum value, the two curves are not on the same scale. Figure 6.17 shows the PSDs of the transmitted signal (A) and ACI (B), together with the PSD of the signal at the receiver filter output (C) and the combined signal plus ACI PSD at the output of the downlink Chebyshev filter (D).

6.2.4 Carrier and Symbol Synchronization

The effect of carrier synchronization error is illustrated in Fig. 6.18, where the solid curve shows the channel performance without phase error for comparison. The remaining curves are obtained by varying

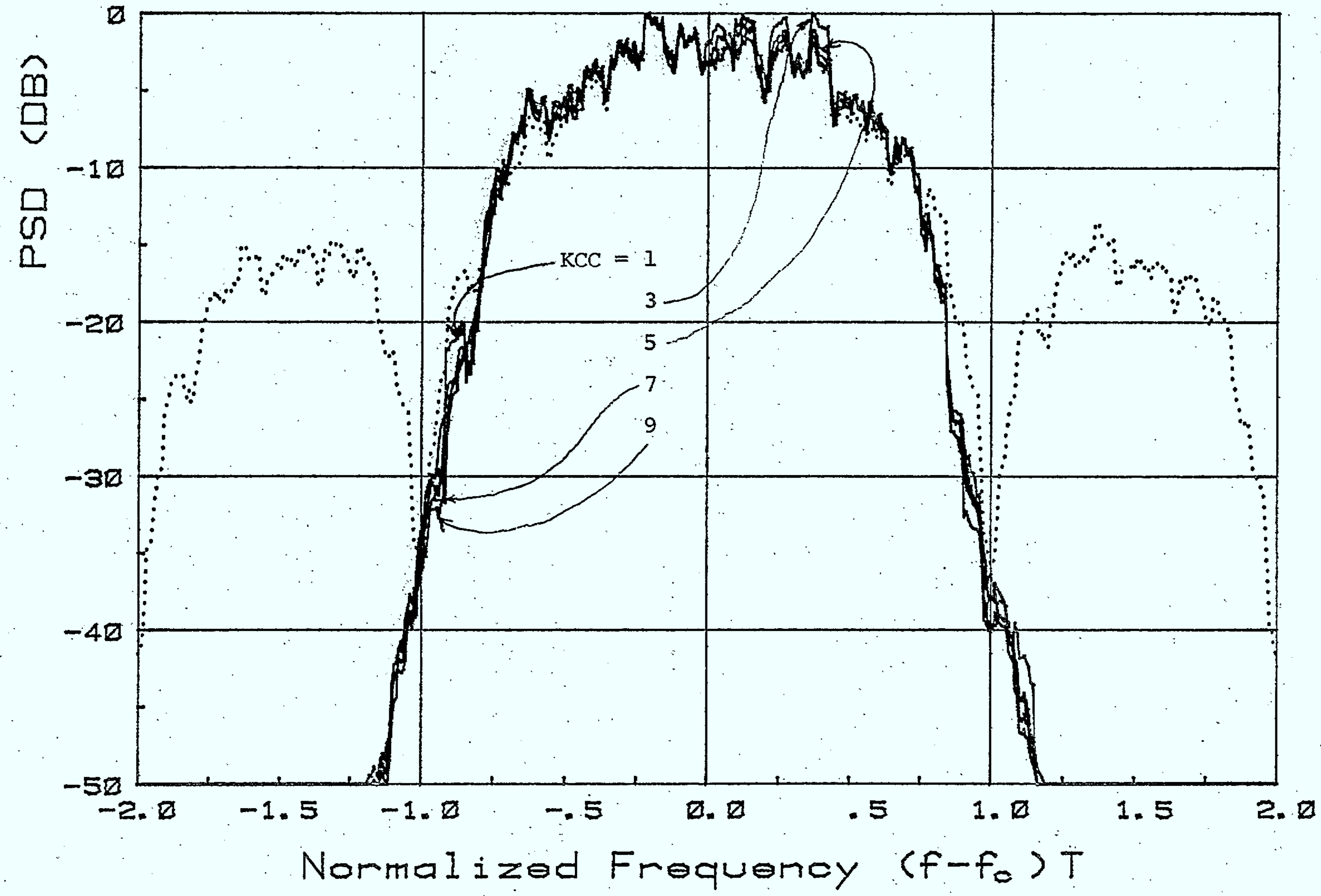

Fig. 6.14 Transmitted signal PSD (•••••), and PSDs at the receive filter output for 4-phase CPSK with different numbers of CCI tones added.

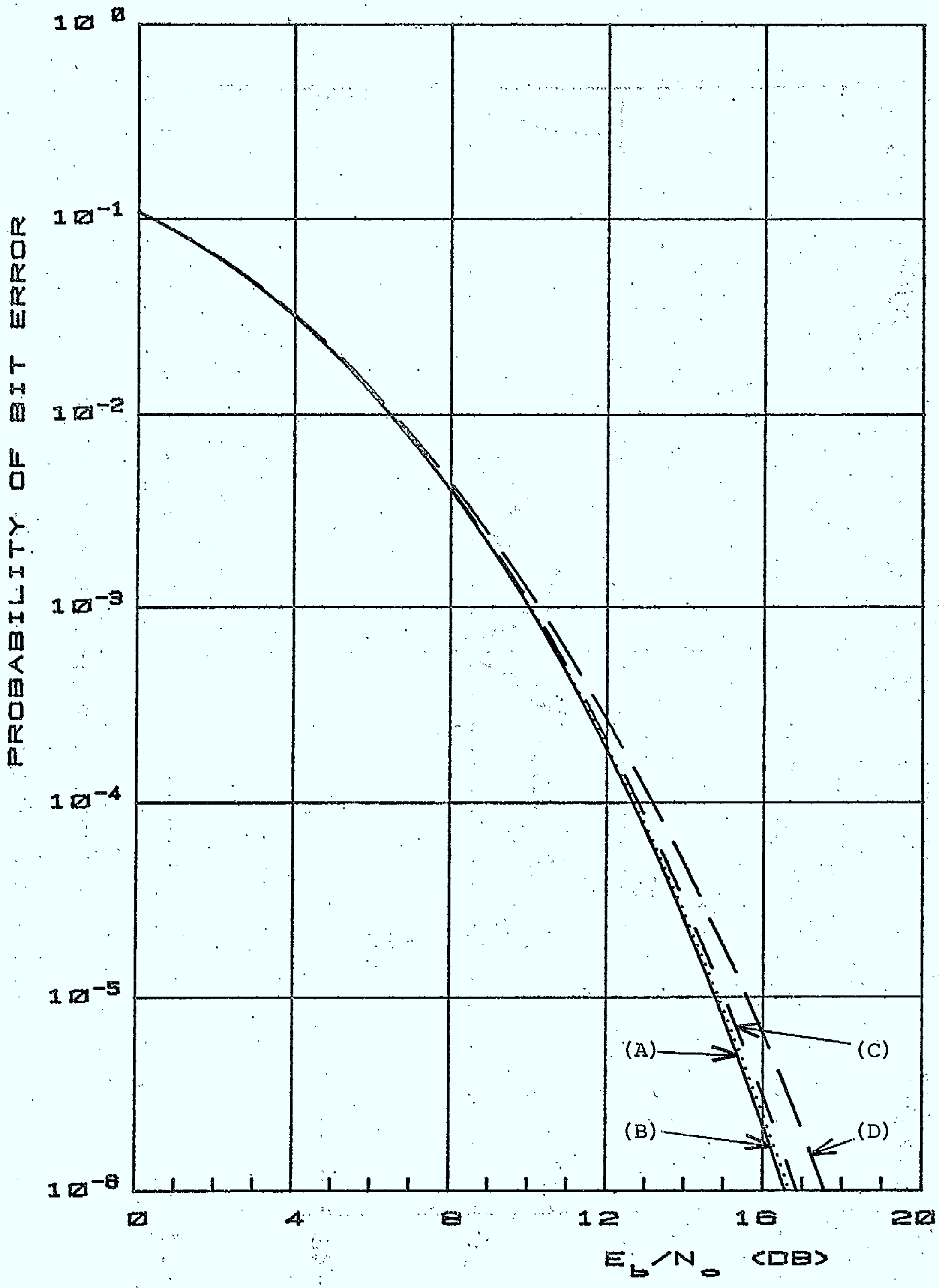

Fig. 6.15 P_e versus E_b/N_o for 4-phase CPSK with one CCI tone and an ACI with interchannel separation CHSEP = 0.1, and AATNDB: (A) (CCI only); (B) 6 dB; (C) 3 dB; and (D) 0 dB.

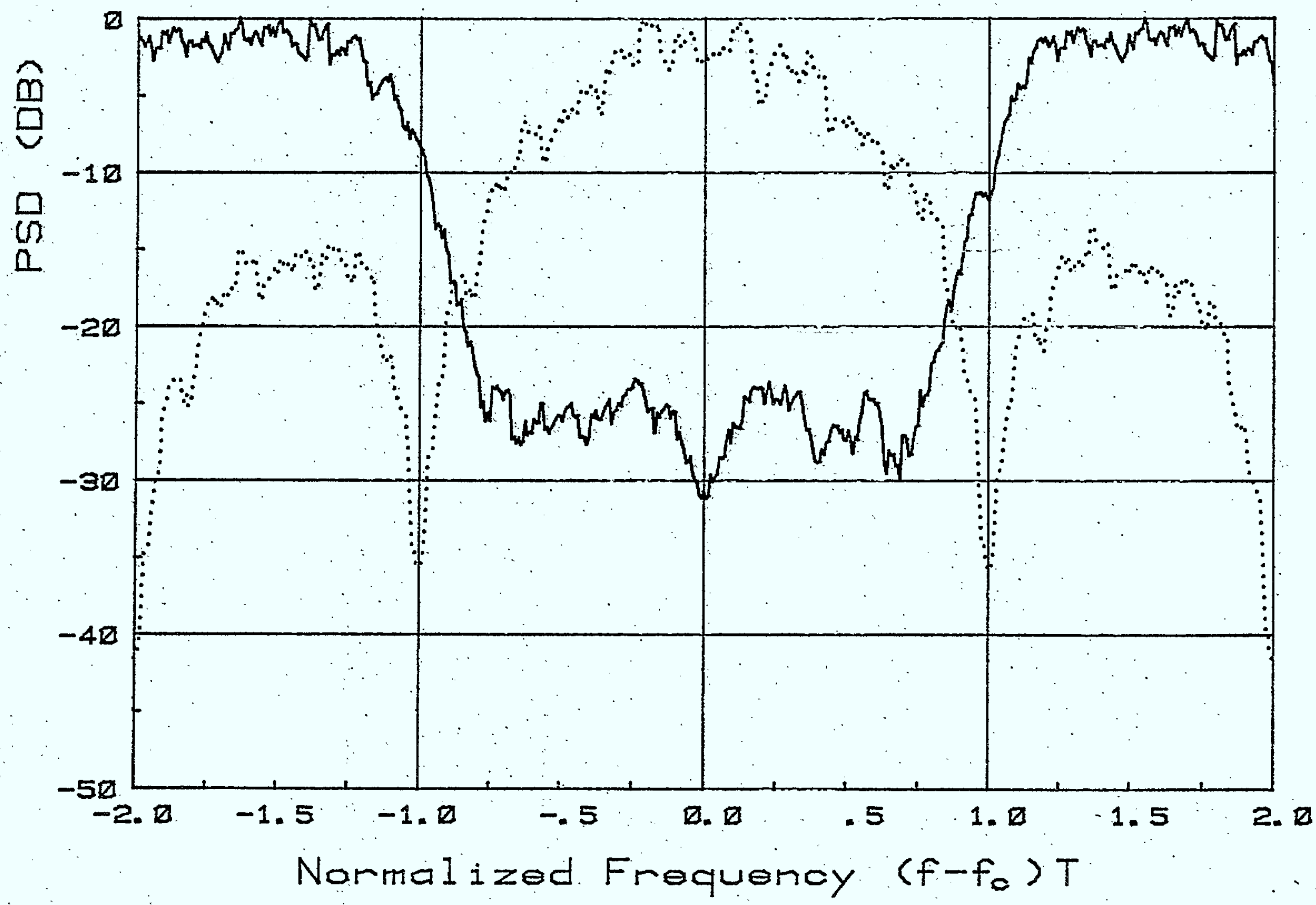

Fig. 6.16 Transmitted signal PSD (••••••), and the ACI PSD (———) at the output of the uplink Chebushev filter (not on the same scale).

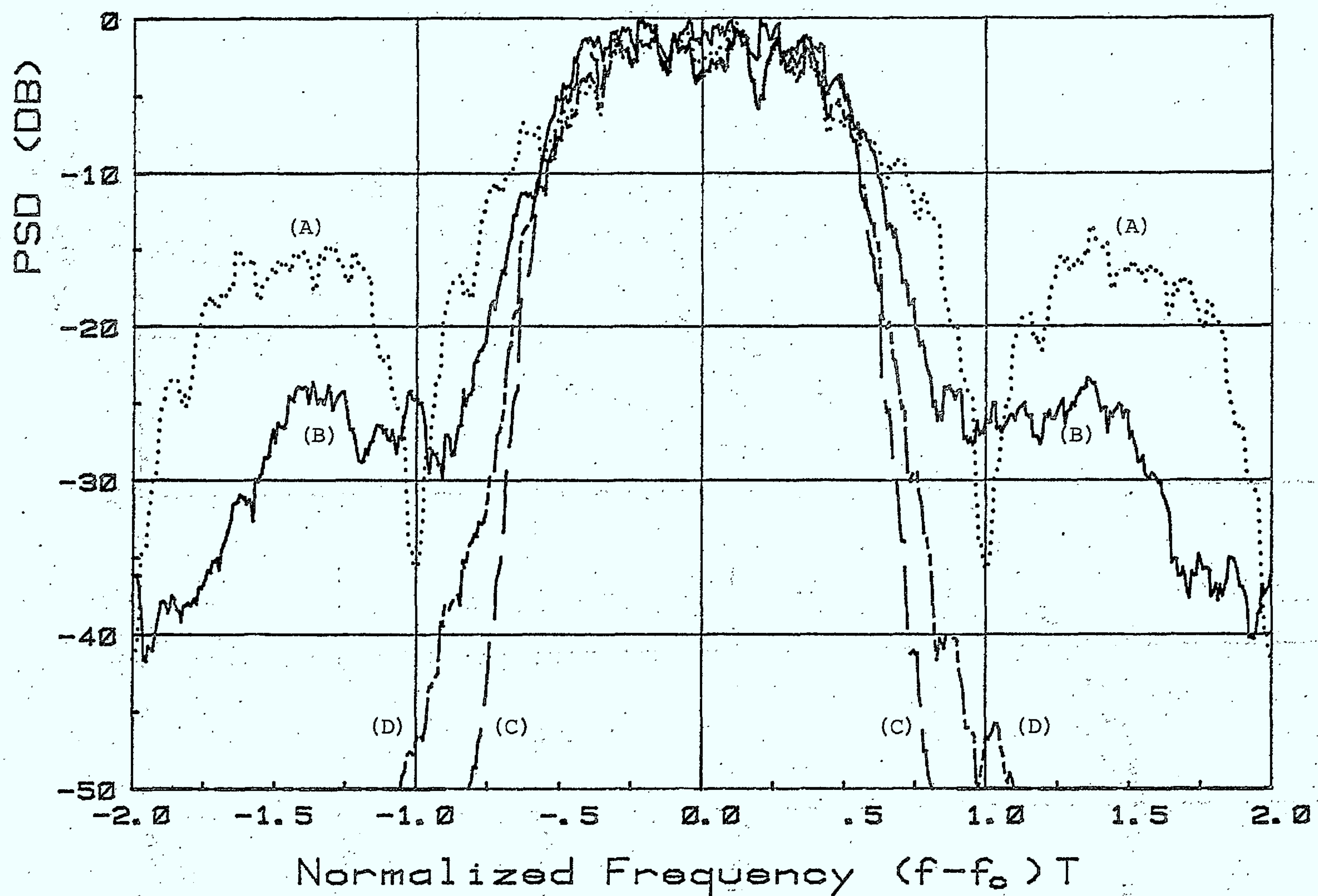

Fig. 6.17 PSDs of the transmitted signal (A) and ACI (B), receiver signal PSD (C), and the combined (signal + ACI) PSD at the output of the downlink Chebushev filter.

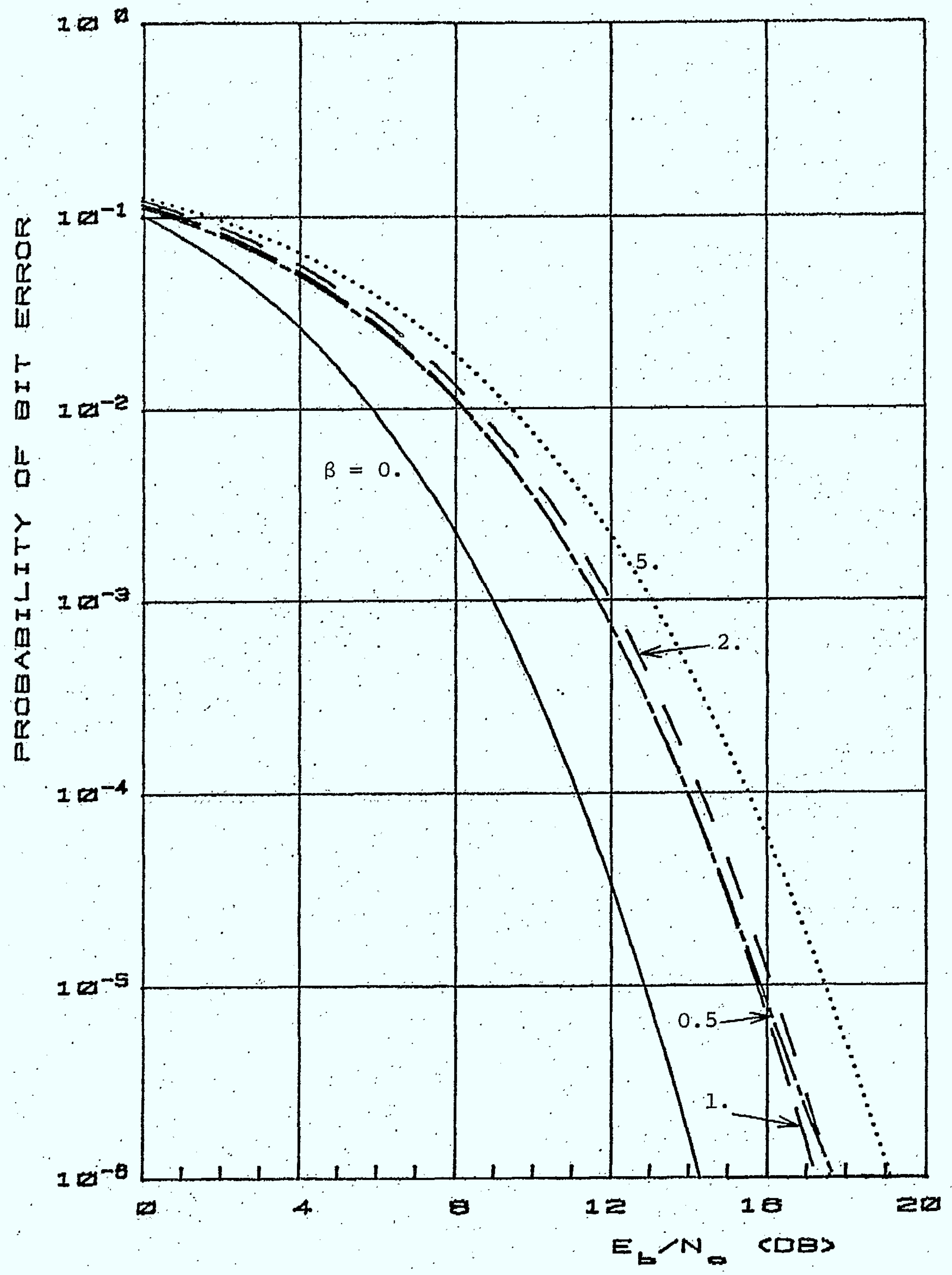

Fig. 6.18 P_e versus E_b/N_o for 4-phase CPSK showing the effects of imperfect carrier syncronization.

parameter BTL4 (β in Eq. (4.39)). As can be seen in Fig. 6.18, the higher the bandwidth ratio B/B_n, the larger the performance degradation.

By varying the normalized standard deviation BTL2 (ε_n in eq. 4.40), we obtain the set of curves in Fig. 6.19. These curves show the effect of symbol timing error on system performance. It is apparent from the results that, when ε_n increases to more than 10 percent of the symbol duration, the performance is drastically degraded. In fact, we found that the probability of error is governed by intersymbol intereference only.

6.3 Other Modulation Schemes

All the results presented so far, illustrate performance for the quadrature (4-phase) shift keying type of modulation. This type is the most frequently used in actual satellite communications channels and, consequently, the majority of the results published in the literature, refers to this type. In this subsection we present some illustrative examples using other types of modulation which are also available in the simulation package.

Figure 6.20 shows the channel performance when the 2-phase CPSK is used. The dotted curve represents P_e versus E_b/N_o, for the channel which includes pulse-shaping filters with x/sin(x) compensations in both transmitter and receiver. The solid curve in Fig. 6.20 shows the channel performance with 4-phase CPSK under the same conditions as 2-phase CPSK, for comparison.

It can be seen that for the value of 1.15 for BT, the performance of the 2-phase CPSK is about 1 dB better than that of the 4-phase CPSK at $P_e = 10^{-5}$. The dashed curve shows the performance for the 2-phase

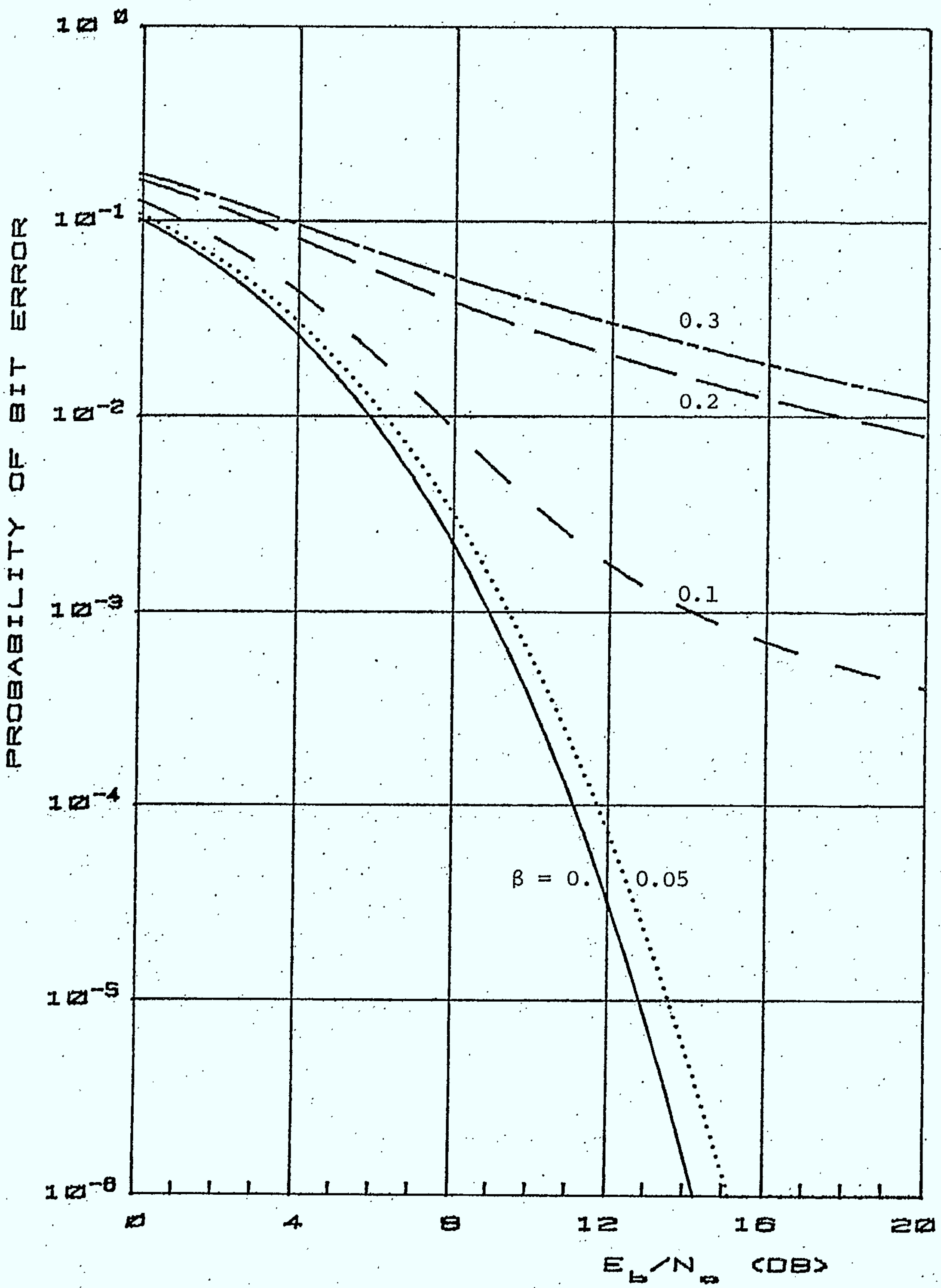

Fig. 6.19 P_e versus E_b/N_o for 4-phase CPSK showing the effects of symbol synchronization error.

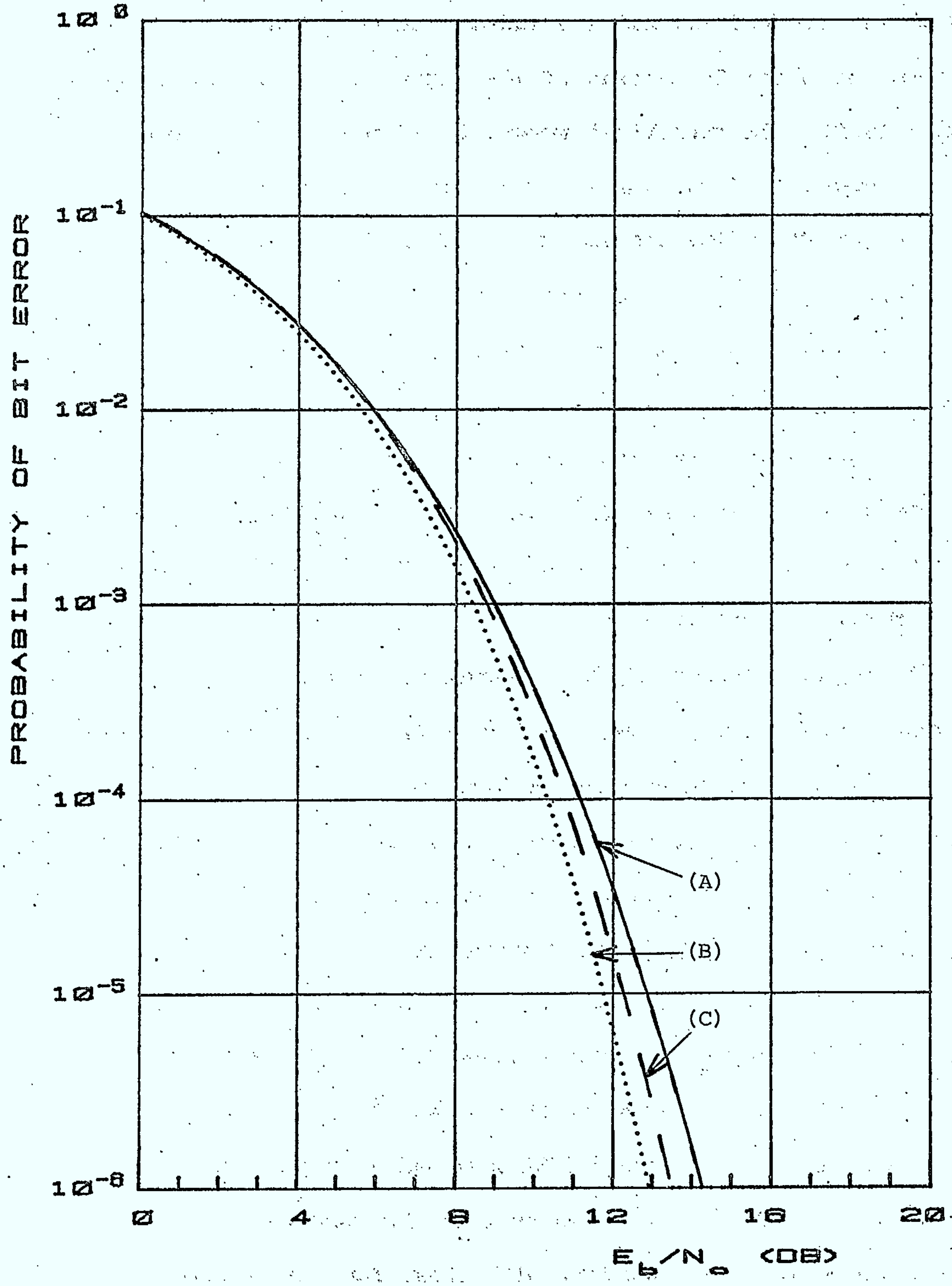

Fig. 6.20 P_e versus E_b/N_o for 4-phase CPSK (A), for 2-phase CPSK (B), both with the PSFs, and for 2-phase CPSK with CCI and ACI added (C).

CPSK where both CCI and ACI are added. There is one CCI tone at the frequency at which 25 percent of the signal energy is contained, with SCCIR = 15 dB. The normalized separation of the adjacent channel is 0.1 and its energy is 3 dB smaller than the signal energy (before filtering). Degradation does not exceed 0.5 dB in the case shown.

Figures 6.21 and 6.22 show the effects of carrier and symbol synchronization errors on the 2-phase CPSK, respectively. The solid curve in Fig. 6.21 shows the channel performance in the absence of carrier synch error for comparison. The remaining curves are obtained by varying parameter BTL2 (β in eqs. (4.35) and (4.36)). As in the 4-phase CPSK case (Fig. 6.18), the higher the PLL bandwidth, the larger the performance degradation.

By varying the normalized standard deviation BTL2 (ε_n in Eq. 4.40), we obtain the set of curves in Fig. 6.22, which show the effect of symbol timing error on system performance. It is apparent from the results that, when ε_n increases over 10 percent of the symbol duration, the performance is drastically degraded, since the probability of error is governed by intersymbol interference only.

Channel performance with the 8-phase CPSK is illustrated with the same set of parameters as for 2-phase CPSK. Figure 6.23 shows the results. The solid curve is for the 4-phase CPSK case (for comparison). The dotted curve is for the 8-CPSK with pulse-shaping filters, and the dashed curve is for the case where both CCI and ACI are added. All running parameters are identical with those for the 2-phase CPSK case, presented in Fig. 6.20. System performance is governed by the intersymbol interference since 1.15 is too small BT product for the 8-phase CPSK (here, T refers to a symbol duration).

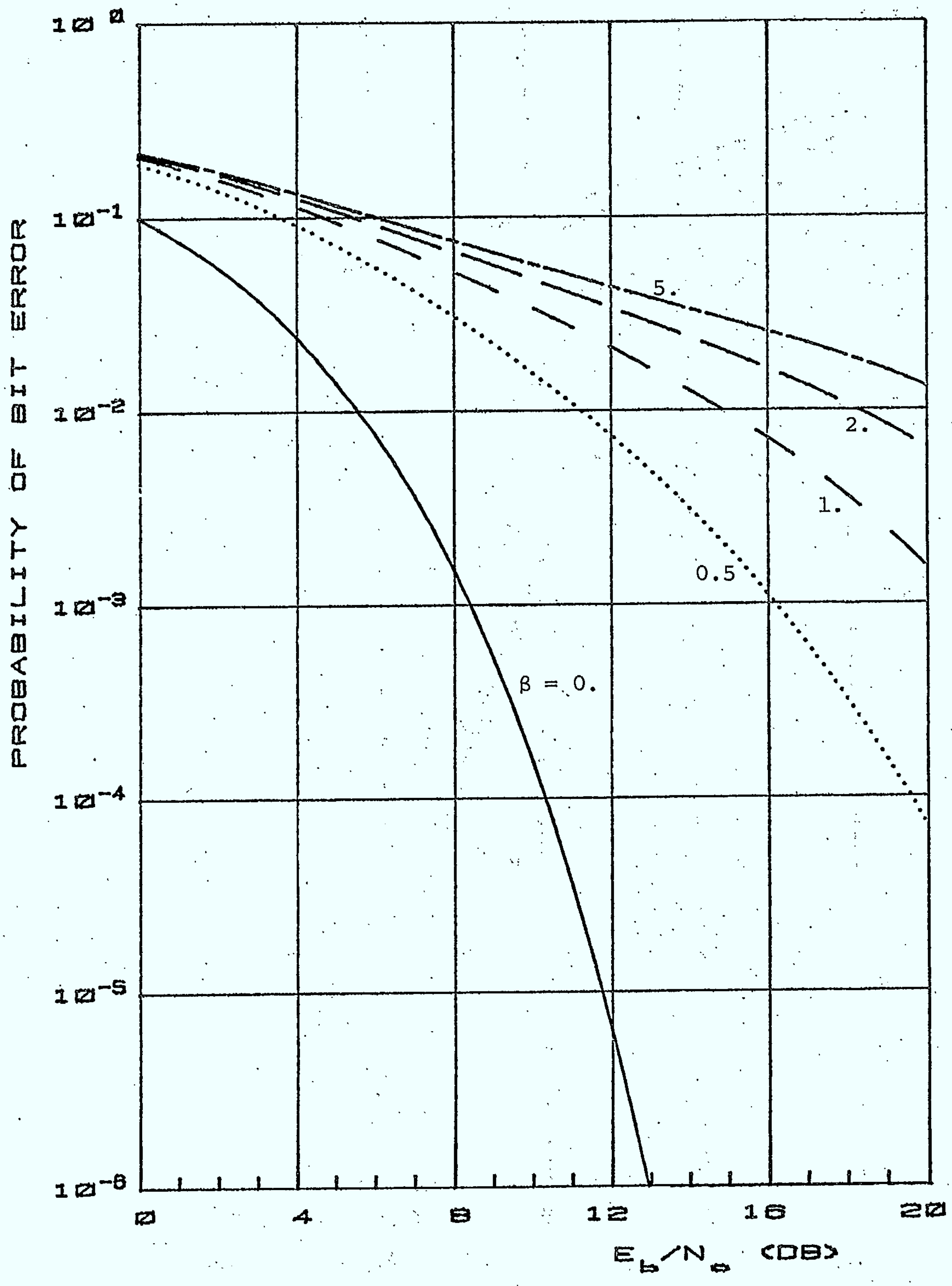

Fig. 6.21 P_e versus E_b/N_o for 2-phase CPSK with the effects of carrier synchronization.

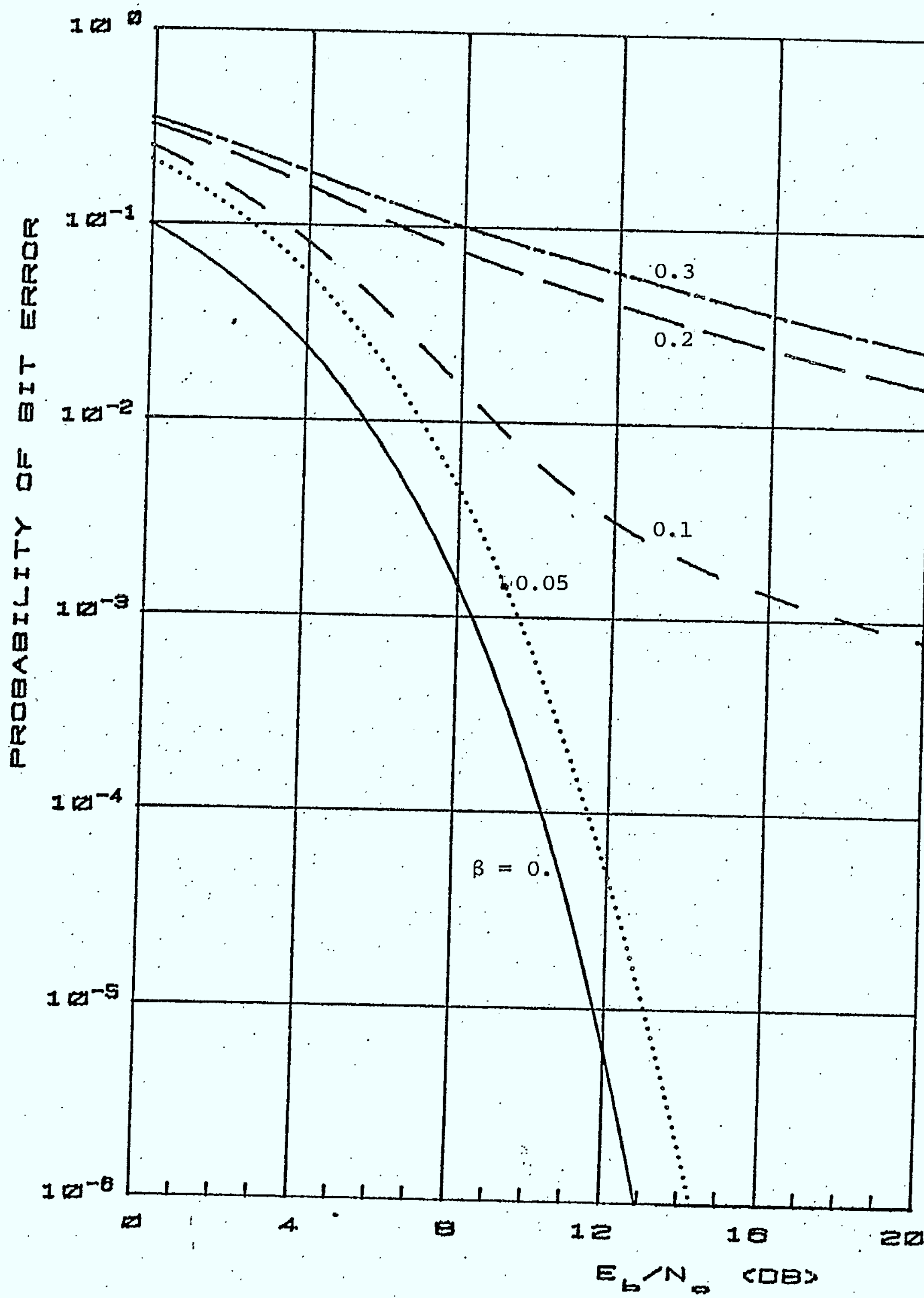

Fig. 6.22 P_e versus E_b/N_o for 2-phase CPSK with the effects of symbol synchronization.

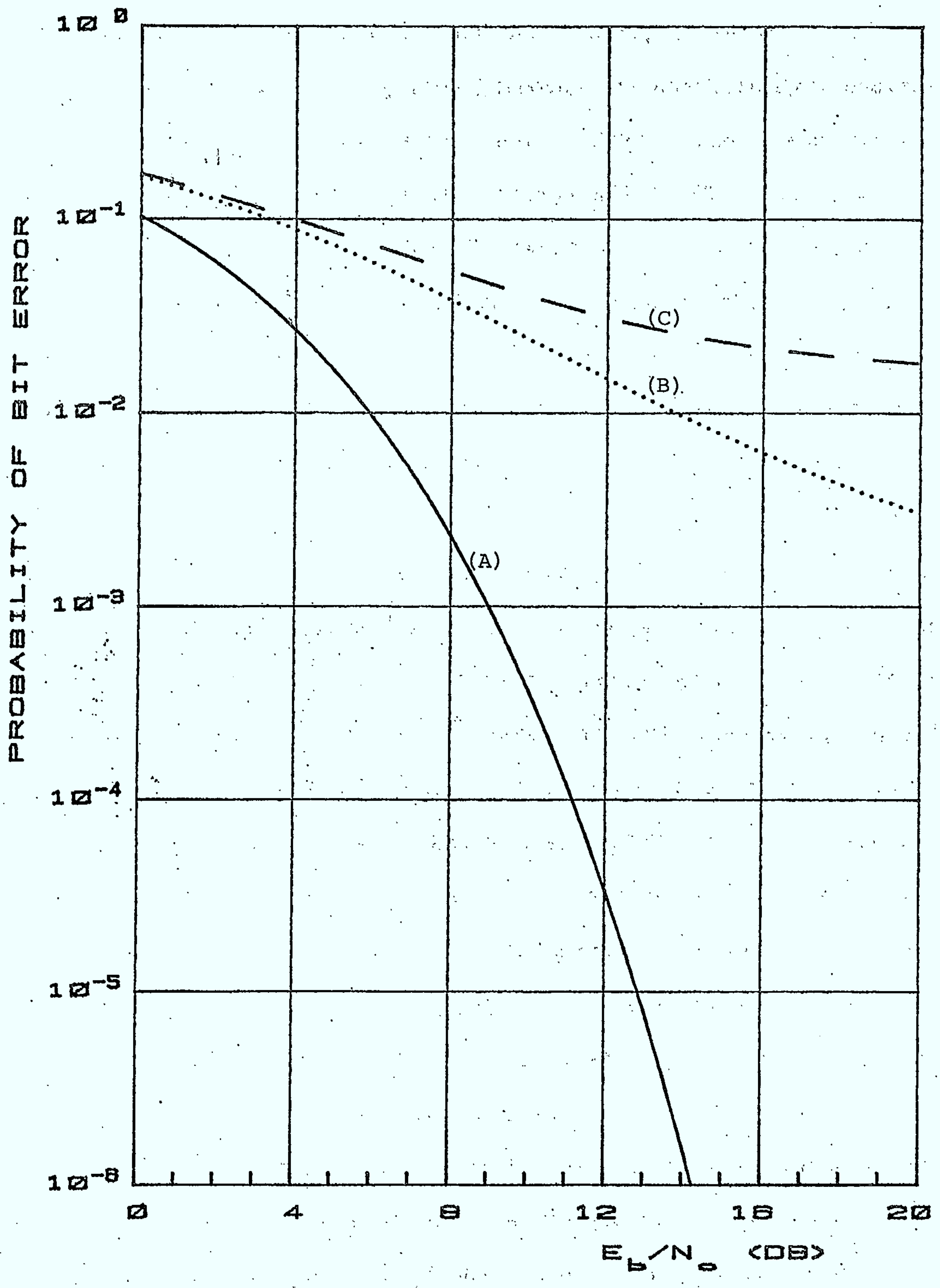

Fig. 6.23 P_e versus E_b/N_o for 4-phase CPSK (A), for 8-phase CPSK (B), both with the PSFs, and for 8-phase CPSK with CCI and ACI added (C).

The next three figures show the simulation results for CPSK modulations with differential encoding employed. Figure 6.24 shows four curves for the 2-phase CPSK. The curve (A) illustrates the basic channel, the curve (B) is the result when the PSFs are included in both transmitter and receiver, the curve (C) (with shorter dashes) shows the case when one CCI tone is added, and the curve (D) (with long dashes) shows the performance when the ACI is added. The simulation parameters are the same as those used in Figs. 6.21 and 6.23. We note that the overall degradation in performance from curve (A) to curve (D) is less than 1 dB.

Figures 6.25 and 6.26 present the results for 4-phase CPSK and 8-phase CPSK, respectively, both with differential encoding. Curves (A) to (D) in these figures correspond to the curves in Fig. 6.24, and the simulation parameters are the same. As in the case of coherent encoding, adding of one CCI tone to 4-phase PSK, degrades the channel performance by about 2 dB, whereas adding ACI does not increase P_e singificantly. In the 8-phase case, the value of BT = 1.15 is again too small as in the coherent encoding case.

Figure 6.27 shows the performance of the satellite channel when 2-phase differential phase shift keying (DPSK) is used. The solid curve is for the channel with both transmitter and receiver PSFs included, and the dotted curve shows the probability of error when CCI and ACI are added. The simulation parameters are the same as in previous figures. The number of E_b/N_o values for which the P_e was calculated is reduced in this case because of long computation time needed for each point on a diagram. The curve for the basic channel was not drawn for the same reason. We see that, in the presence of the PSFs, channel performance

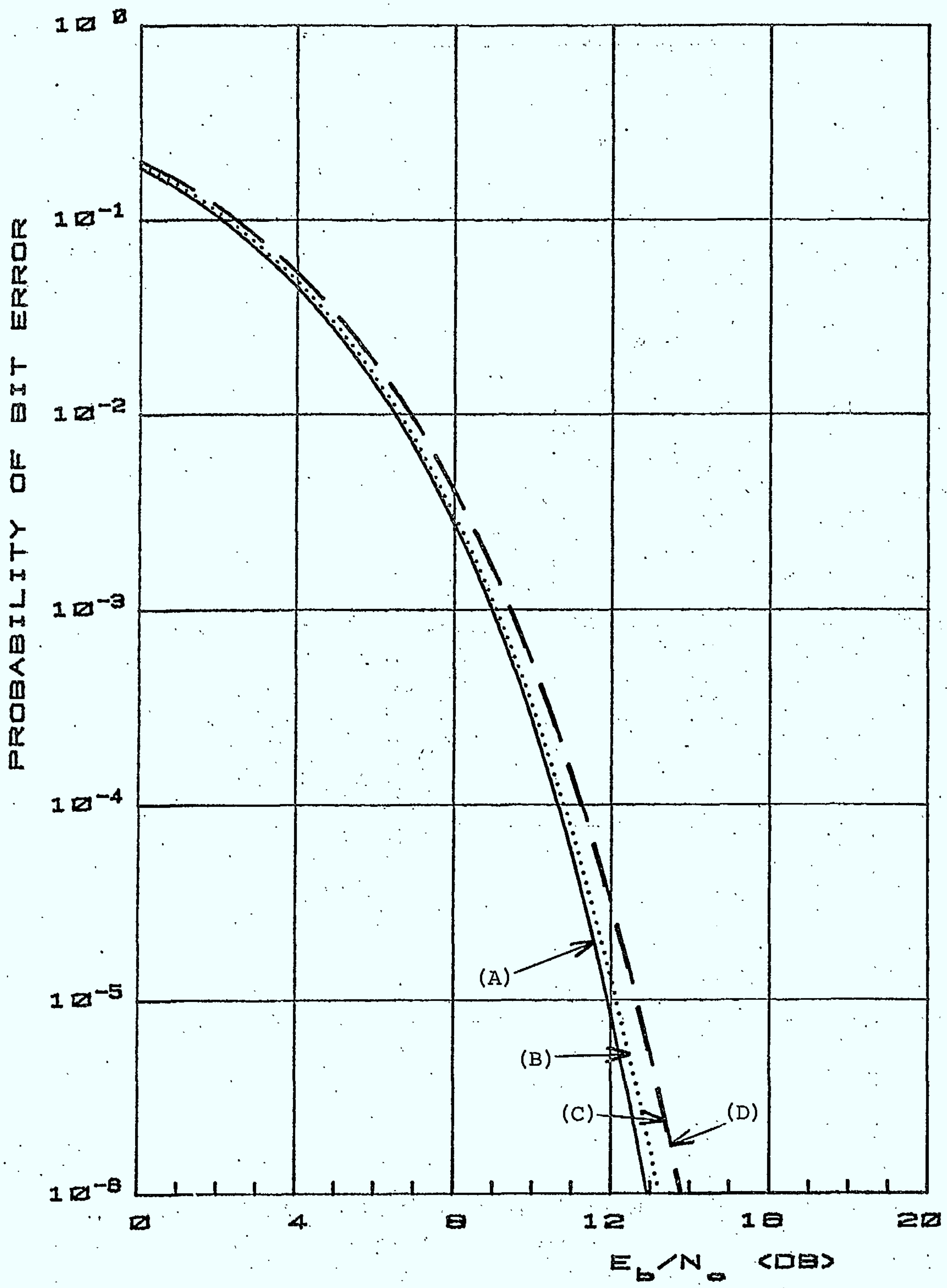

Fig. 6.24 P_e versus E_b/N_o for 2-phase CPSK, differential encoding. Basic channel (A), with PSFs (B), with CCI tones added (C), and with ACI (D).

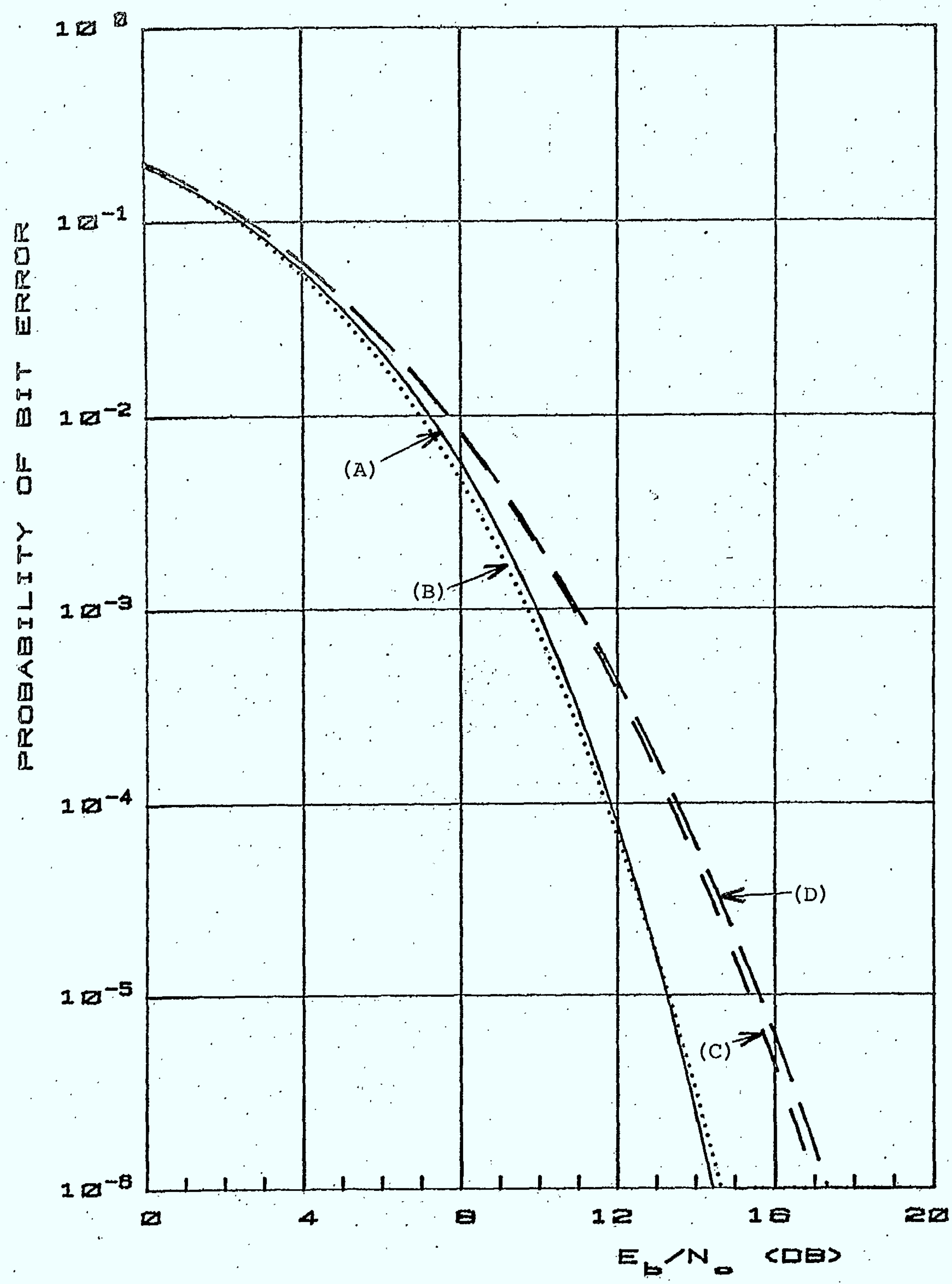

Fig. 6.25 P_e versus E_b/N_o for 4-phase CPSK, differential encoding. Basic channel (A), with PSFs (B), with CCI tones added (C), and with ACI (D).

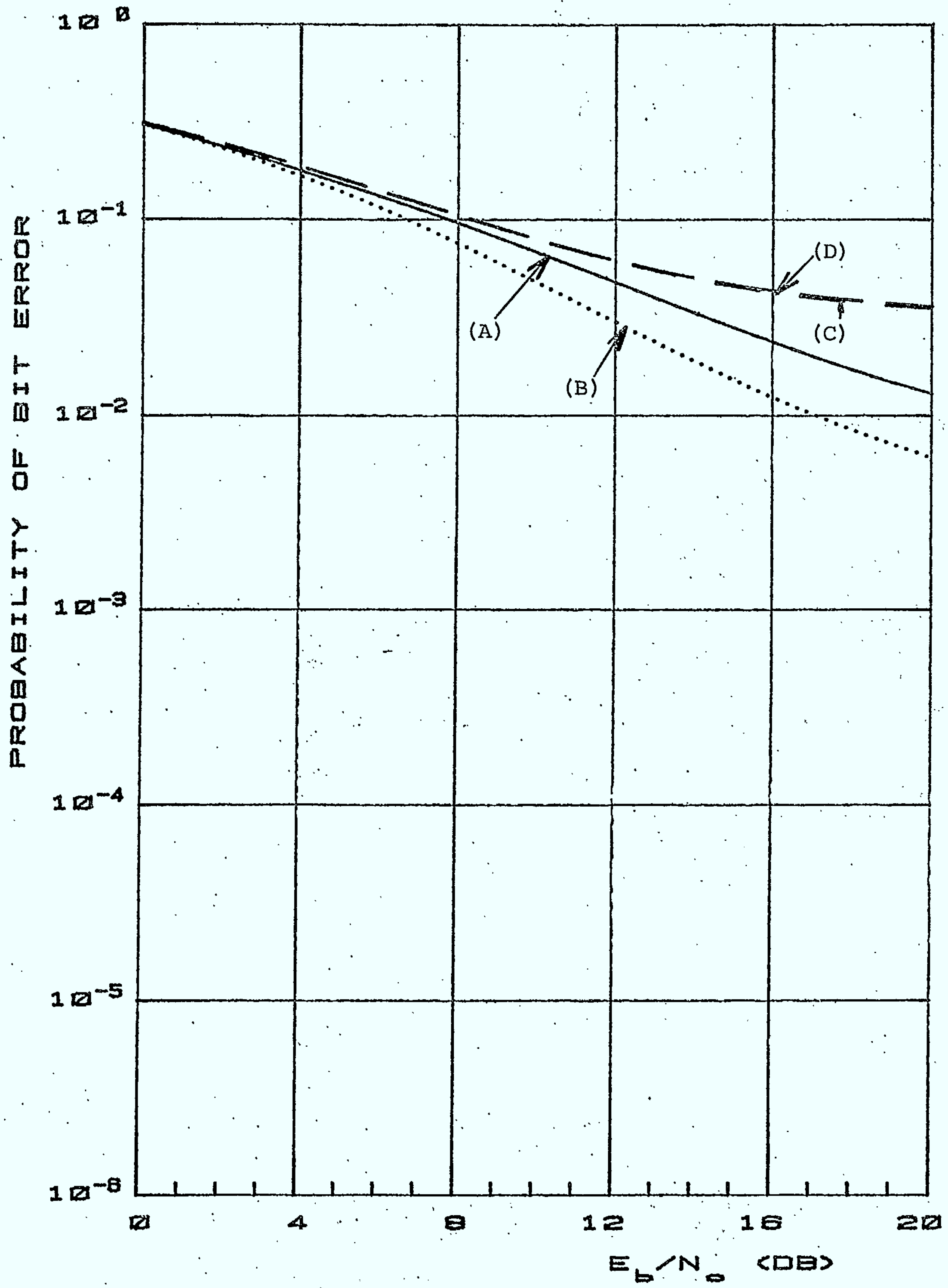

Fig. 6.26 P_e versus E_b/N_o for 8-phase CPSK, differential encoding. Basic channel (A), with PSFs (B), with CCI tones added (C), and with ACI (D).

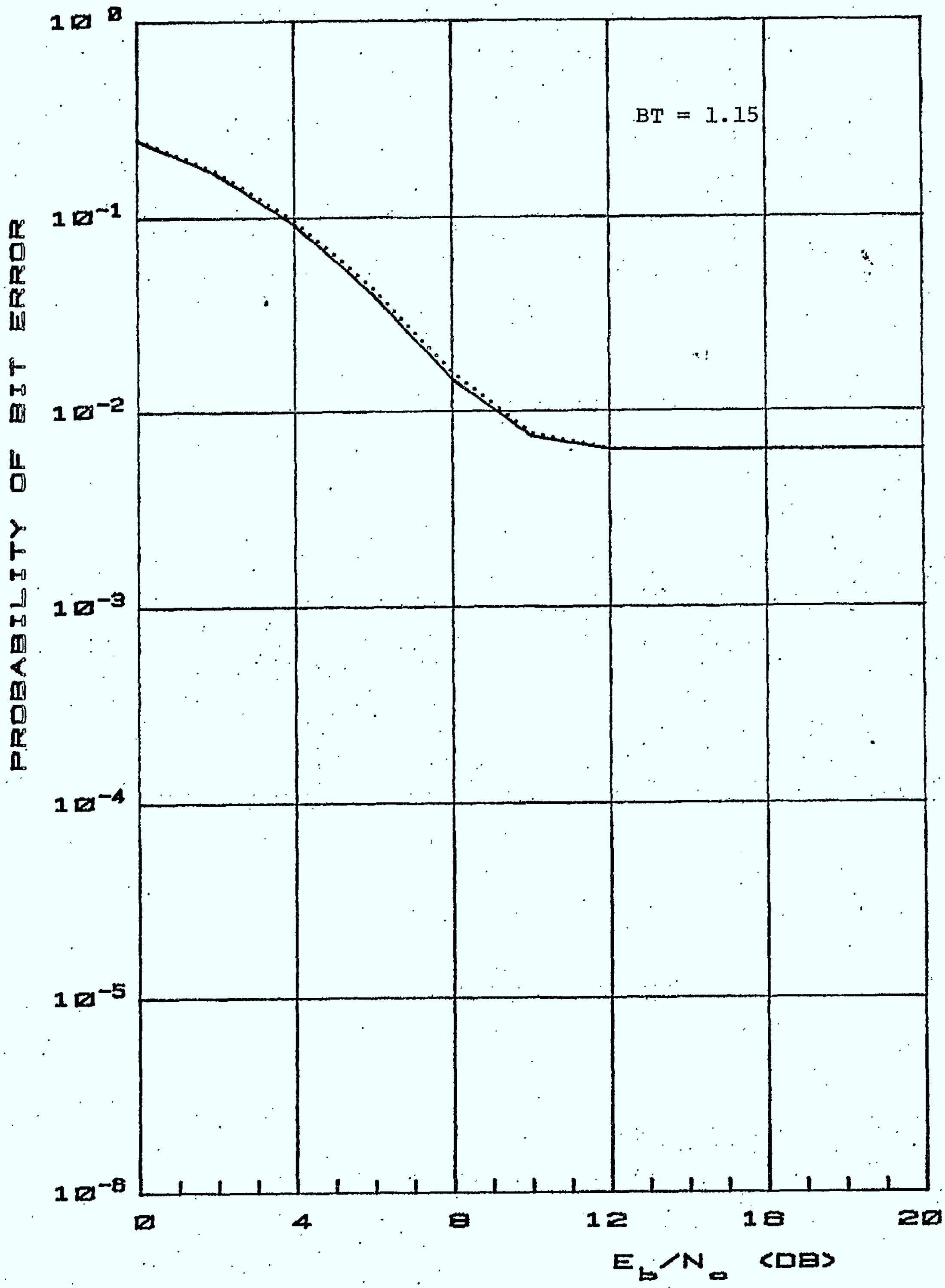

Fig. 6.27 P_e versus E_b/N_o for 2-phase DPSK with PSFs included (solid curve), and with CCI and ACI added in the uplink path (dotted curve).

degrades, and is leveled off for higher values of SNR due to large intersymbol intereference. The addition of the CCI and ACI does not degrade the performance significantly. The two curves in Fig. 6.27 almost overlap.

The last set of diagrams shows the channel performances when the offset-PSK and FFSK modulations are employed.

Figure 6.28 contains 4 curves. The solid curve (A) is the case of 4-phase CPSK in the basic channel case shown for comparison. Curve (B) is for the offset CPSK case, again for the basic channel, curve (C) shows the performance when the PSFs and the HPA are included, while the curve (D) depicts the performance when both CCI and ACI are added in the uplink path. Performance degrades significantly with the addition of the PSFs and the HPA, while CCI and ACI further increase the probability of error.

The set of diagrams for the FFSK case is shown in Fig. 6.29. All the curves in this figure have exactly the same set of parameters as those in Fig. 6.28. Again, as in the offset CPSK case, the performance degrades rapidly with PSFs, HPA, and interfering signals.

Figures 6.30 and 6.31 show the effects of carrier synch error (curve (B)) and symbol synch error (curve (C)) for the offset CPSK and FFSK, respectively. Curve (A) in these figures is the performance without synchronization errors, with the same set of simulation parameters.

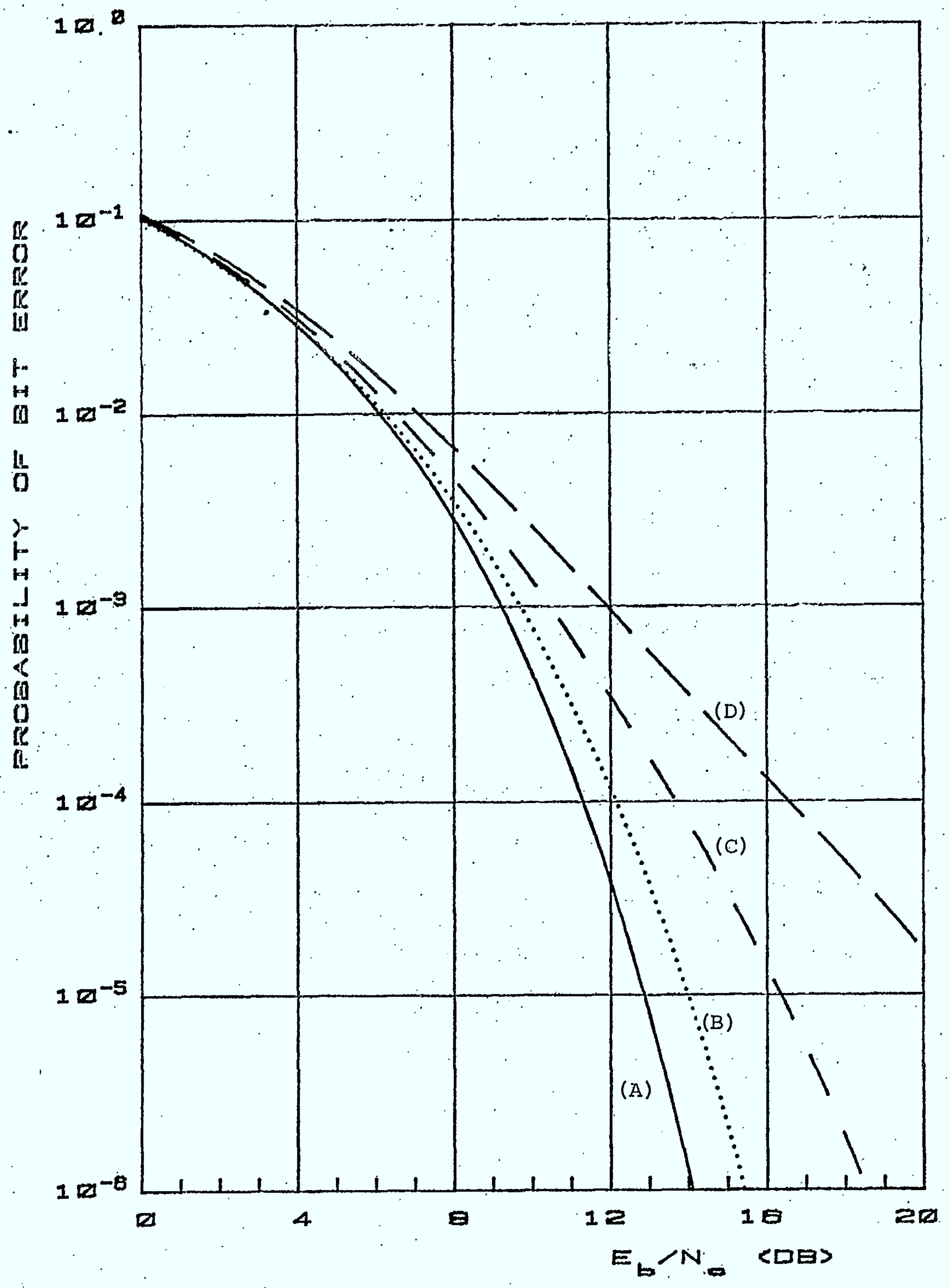

Fig. 6.28 P_e versus E_b/N_o for offset CPSK with 4-phase CPSK (A) for comparison. Curve (B) is for the basic channel, same as (A), curve (C) for the case when PSFs are in the channel, and curve (D) for the CCI and ACI included in the uplink path.

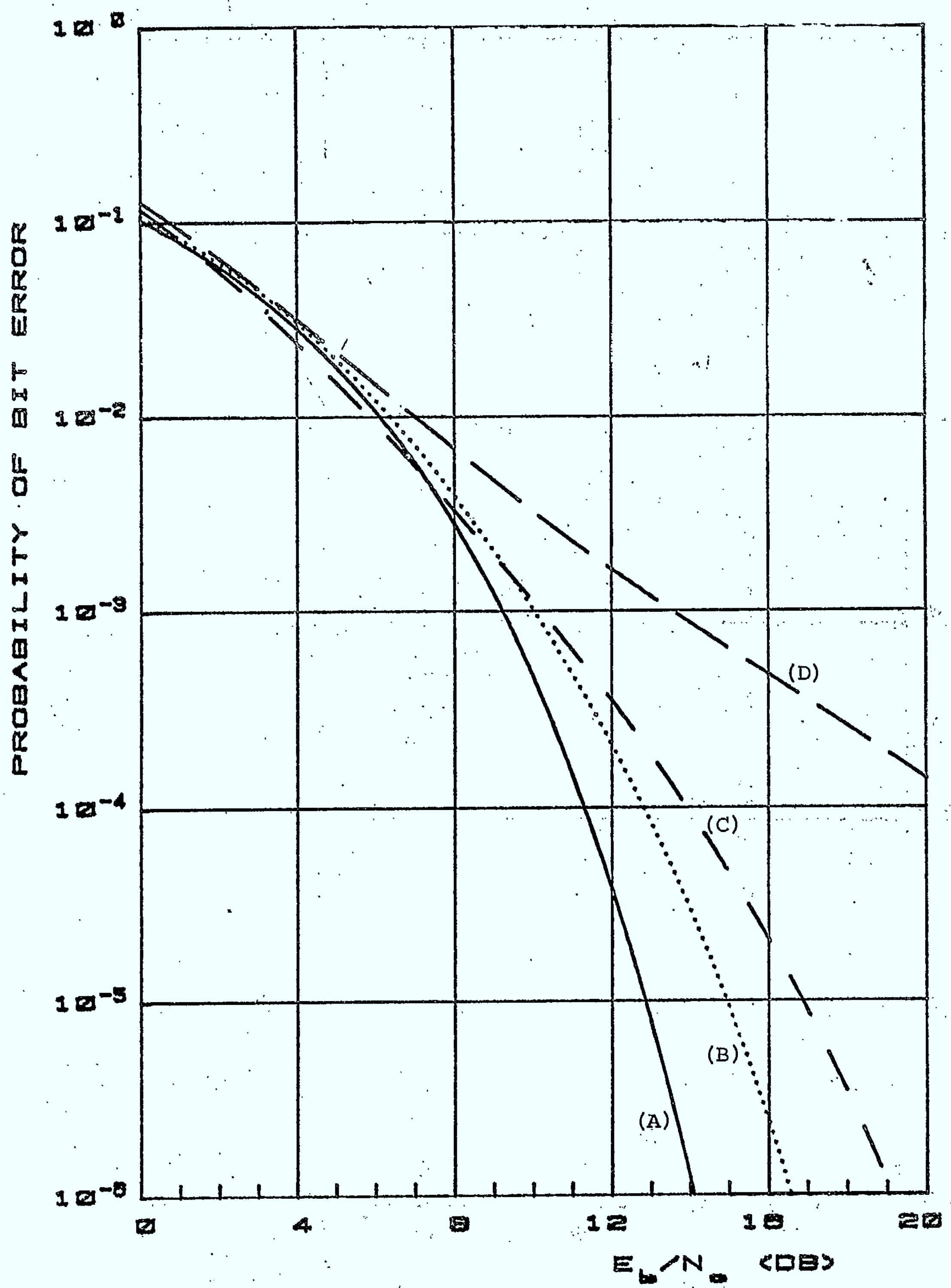

Fig 6.29 P_e versus E_b/N_o for FFSK with 4-phase CPSK (A) for comparison. Curve (B) is for the basic channel, same as (A), curve (C) for the case when PSFs are in the channel, and curve (D) for the CCI and ACI included in the uplink path.

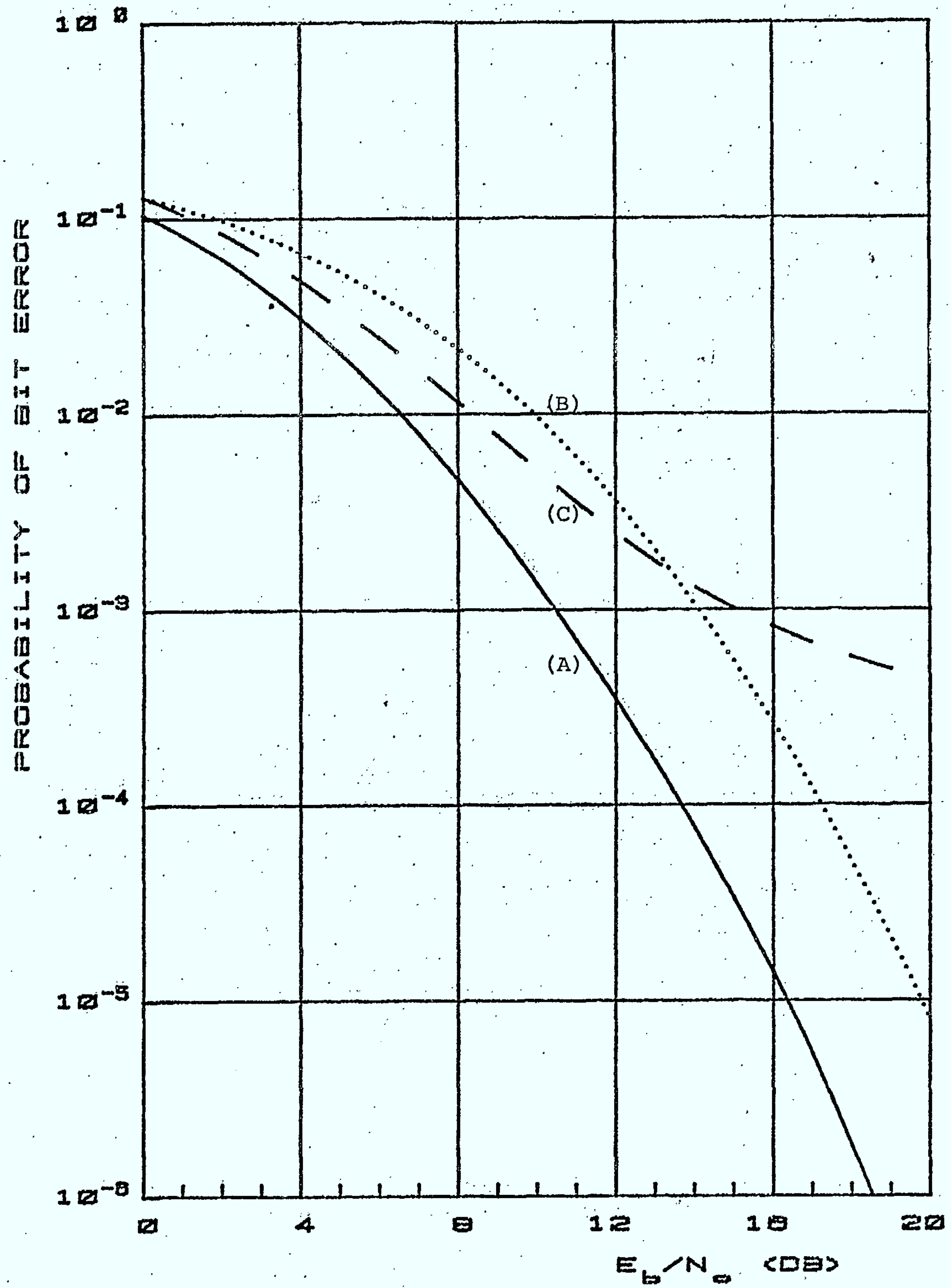

Fig. 6.30 P_e versus E_b/N_o for offset CPSK with PSFs: without synchronization error (A), with the carrier synch error (B), and with the symbol synch error (C).

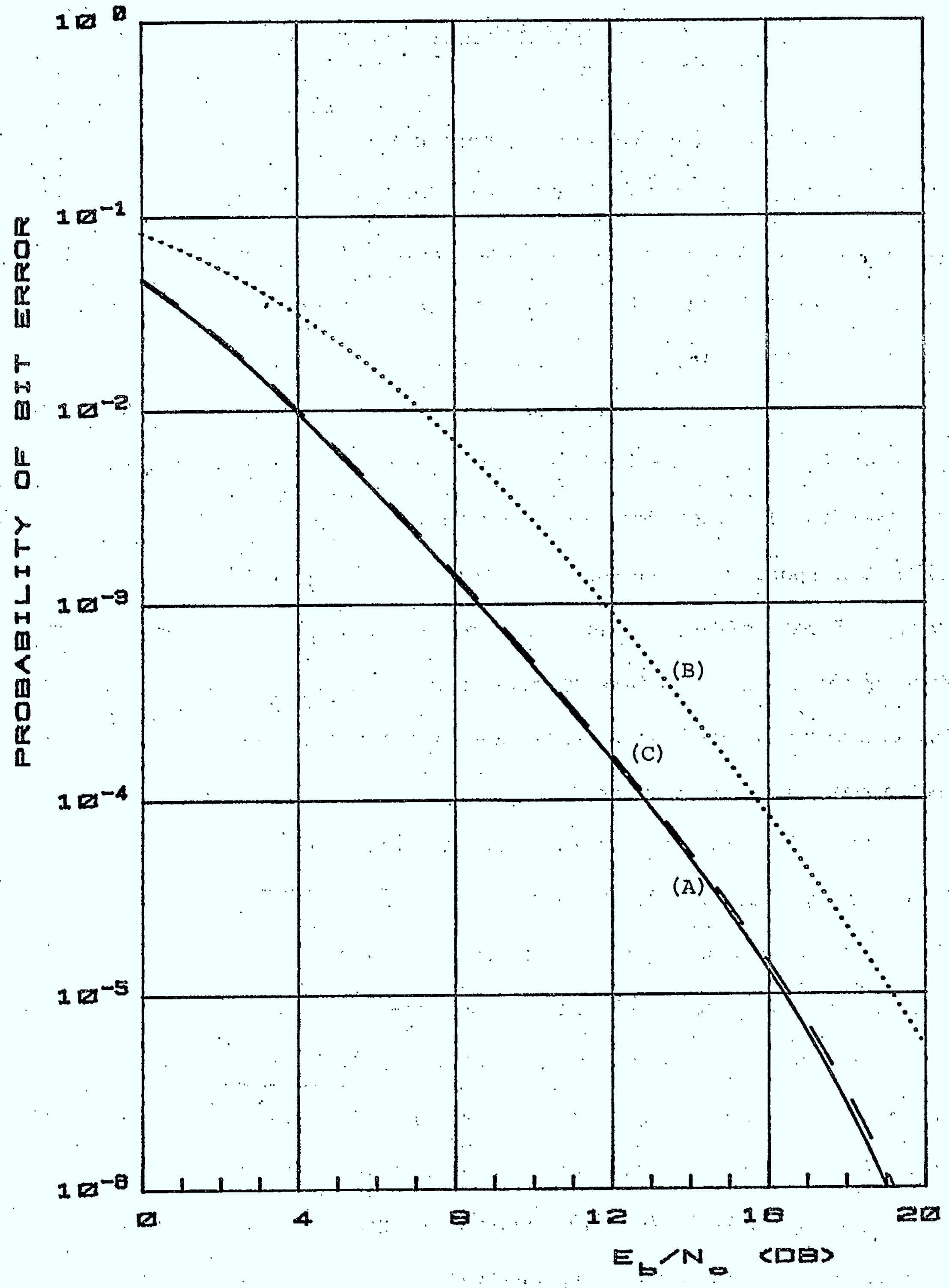

Fig. 6.31 P_e versus E_b/N_o for FFSK with PSFs: without synchronization error (A), with the carrier synch error (B), and with the symbol synch error (C).

7. SUMMARY AND CONCLUSIONS

The primary purpose of the investigation reported here was to develop and demonstrate a sophisticated computer simulation package for predicting the performance of digital satellite transmission systems. It provides a useful tool for the design and optimization of satellite communications systems and their components.

In a previous study, a computer simulation package was developed which included the primary sources of system performance degradation; namely intersymbol interference and nonlinear distortion due to the satellite transponder. However, a number of other effects were not included. These effects tend to be secondary when assessing the relative performance of different modulations, but become very important when attempting to predict the actual performance level of a given modulation on a satellite channel.

A number of these secondary effects were included in the study presented in this report. These are:

(1) The effect of cascaded nonlinearities, when the transmit earth station's high-power amplifier is included.

(2) The effect of pulse-shaping filters in both transmitter and receiver. Each such filter here consists of a Nyquist cosine rolloff filter (approximated by a fourth-order Butterworth) cascaded with an x/sin(x) amplitude equalizer and an all-pass network for group-delay compensation.

(3) The effects of cochannel interference, in either the uplink or downlink path, are represented by a number of sinusoidal tones (up to 10) distributed over the frequency band of interest.

(4) The effect of adjacent channel interference in either the uplink or downlink path, represented by signals having the same properties as the useful signal, and separated in frequency end by a specified amount.

(5) The effect of errors in carrier and clock recovery algorithms.

Inclusion of the above effects makes it possible to evaluate the performance of the satellite communication channel with greater flexibility than by using the original simulation package.

Some of the modulation schemes had proved earlier to be quite inadequate for satellite transmission systems, notably amplitude-phase-shift keying [1]. They are, therefore, excluded from this study. On the other hand, some additional modulation types were included, such as differentially encoded 2, 4 and 8-phase coherent phase-shift keying. Furthermore, the offset phase-shift keying and the fast frequency-shift keying were redesigned so as to be consistent with the modern approach which treats them as a special case of the 4-phase PSK, rather than the binary PSK.

Simulation results presented in this report, confirm the conclusions that, in general, the 2 and 4-phase PSKs as well as the offset PSK and FFSK are more robust modulation types under the conditions of the basic channel than the 8-phase PSK and the DPSK. Under the conditions of added nonlinearities and pulse shaping filters, the 2 and 4-phase PSKs remain more robust than the offset PSK and FFSK modulations. The latter two, however, are still useful under the nominal satellite channel conditions. On the other hand, the sensitivity of the 8-phase PSK and DPSK to the channel nonlinearity is even more emphasized when an additional cascaded nonlinearity is present, and they appear to be generally inappropriate for use in satellite communications if the HPA and TWT are operated in the nonlinear region.

The simulation results presented in this report are only a representative sample of what it is possible to obtain. Many different combinations of channel parameters can be used and their effects on any one of the various modulation types can be evaluated. Because of the detailed nature of the included effects, the simulation package should be useful as a system design tool, and we envisage some future work in this area.

In particular, we feel that it should be a most useful tool for developing optimal filtering strategies for both present and future generations of communications satellites. As an increasing percentage of the communications traffic in satellite systems becomes digital modulations, it will be necessary to develop improved filtering systems. For example, digitally modulated signals are much more sensitive to nonlinear group delay characteristics than their analog predecessors, and it therefore becomes necessary to design filter systems which are carefully group delay equalized. Another area which warrants considerable work is that of the transmit and receive pulse shaping filters (PSF's). In the current study, we have used fourth order Butterworth filters to approximate Nyquist raised cosine rolloff filters, which are optimal for linear channels. However, in the nonlinear satellite channel there is no guarantee that such filters are optimum, and it would be worthwhile to investigate the effects of using other filter types for pulse shaping. Computer simulation is possibly the only viable means for doing this. We, therefore, see that considerable work is possible on the development of filtering systems and which have been optimized for a digital signalling environment, rather than for the analog environment for which all present satellite systems have been designed.

The other major area into which the present work should be extended is to consider the effects of uplink noise. These effects have not been included in the present work because to date the only proven method of doing so is by means of Monte Carlo simulation. Such simulations are inherently very time-consuming and expensive. In most satellite systems in use today, uplink noise effects are of secondary importance because transmit earth stations have large high gain antennas and high power outputs. However, the trend today, particularly in the 11-14 GHz band is toward much smaller earth stations using lower gain antennas and smaller power amplifiers. Systems using them can quite conceivably be uplink noise limited, and it is therefore of considerable importance to develop means for handling uplink noise effects. The simulation package in the present work uses so-called analytic simulation techniques in which signal and deterministic interference effects are simulated and downlink noise effects are calculated. It is highly desirable that similar techniques be developed for handling uplink noise. The problem here is caused by the satellite transponder nonlinearity which causes the uplink noise to become non-Gaussian, and also causes interactions between signal and noise.

REFERENCES

[1] H.C. Chan, D.P. Taylor, and S.S. Haykin, "Comparative Evaluation of Digital Modulation Techniques", Communications Research Laboratory Internal Report Series No. CRL-18, Parts I, II, and III, Communications Research Laboratory, McMaster University, Hamilton, Ontario, Canada, April 1974.

[2] D.P. Taylor, H.C. Chan and S.S. Haykin, "A Simulation Study of Digital Modulation Methods for Wide-Band Satellite Communications", IEEE Trans. Comm., Vol. COM-24, No. 12, pp. 1351-1354, December 1976.

[3] H.C. Chan, D.P. Taylor and S.S. Haykin, "A Comparative Study of Digital Modulation Techniques for Single-Carrier Satellite Communications", Proc. Third International Conference on Digital Satellite Communications, Kyoto, Japan, November 11-13, 1975, pp. 56-64.

[4] R.F. Fang and O. Shimbo, "Unified Analysis of a Class of Digital Systems in Noise and Interference", IEEE Trans. Comm., Vol. COM-21, No. 10, pp. 1075-1091, October 1973.

[5] V.K. Prabhu, "Error Probability Performance of M-ary CPSK Systems With Intersymbol Inteference", IEEE Trans. Comm., Vol. COM-21, No. 2, pp. 97-109, February 1973.

[6] S. Benedetto, E. Biglieri and V. Castellani, "Combined Effects of Intersymbol, Interchannel and Co-channel Interference in M-ary CPSK Systems", IEEE Trans. Comm., Vol. COM-21, No. 9, pp. 997-1008, September 1973.

[7] R.G. Lyons, "The Effect of a Bandpass Nonlinearity on Signal Detectability", IEEE Trans. Comm., Vol. COM-21, No. 1, pp. 51-61, January 1973.

[8] P. Hetracul, D.P. Taylor, and S.S. Haykin, "Effect of a Soft Limiter on the Error-Rate of an M-ary CPSK System", Conference Record, International Communications Conf., ICC'74, pp. 36-22 to 36-26, Minneapolis, Minn., June 17-19, 1974.

[9] T. Muratani, I. Matsushita, Y. Tsuji, and T. Hara, "Simulation of a PSK Transmission System Including the Nonlinear Satellite Channel", 2nd International Symposium on Digital Satellite Communication, pp. 184-192, Paris, France, November 1972.

[10] D.L. Hedderly and L. Lundquist, "Computer-Simulation of a Digital Satellite Communications Link", IEEE Trans. Comm., Vol. COM-21, No. 4, pp. 321-325, April 1973.

[11] M.I. Celebiler and G.M. Goupe, "Effects of Thermal Noise, Filtering and Co-Channel Interference on the Probability of Error in Binary Coherent PSK", IEEE Trans. Comm., Vol. COM-26, No. 2, pp. 257-267, February, 1978.

[12] C.M. Chie and W.R. Brown, "Performance Simulation of a TDMA Satellite Communication Link in the Presence of Adjacent Channel Interference", Conference Record, International Communications Conf., ICC'79, pp. 16.2.1-16.2.5, Boston, Mass., June 10-14, 1979.

[13] M.E. Jones and M.R. Wachs, "Optimum Filtering for QPSK in Bandwidth-Limited Nonlinear Satellite Channels", COMSAT Technical Review, Vol. 9, No. 2A, pp. 465-507, Fall 1979.

[14] F. Assal and K. Betaharon, "Computational Method for the Performance Evaluation of 4-phase PSK Transmission Through Linear and Nonlinear Channels", in H.L. Van Trees (ed.), Satellite Communications, IEEE Press Book, pp. 248-255, Wiley, NY, 1979.

[15] W.C. Lindsey and M.K. Simon, "Telecommunications System Engineering", Prentice-Hall, Inc., Englewood Cliffs, NJ, 1973.

[16] D. Middleton, "An Introduction to Statistical Communication Theory", McGraw-Hill Book Co., New York, NY, 1960.

[17] J.J. Stiffler, "Theory of Synchronous Communications", Prentice-Hall, Inc., Englewood Cliffs, NJ, 1971.

[18] S. Benedetto and E. Biglieri, "Performance of M-ary PSK Systems in the Presence of Intersymbol Interference and Additive Noise", Alta Frequenca, Vol. XLI, pp. 225-239, 1972.

[19] T.S. Koubanitsas and L.F. Turner, "Simple Bound to the Error Probability in Coherent Multi-Phase Phase-Shift-Keyed Systems with Intersymbol Interference and Guassian Noise", Proc. IEE, Vol. 120, pp. 725-732, July 1973.

[20] O. Shimbo, R.J. Fang, and M. Celebiler, "Performance of M-ary CPSK Systems in Gaussian Noise and Intersymbol Interference", IEEE Trans. Information Theory, Vol. IT-19, No. 1, pp. 44-58, January 1973.

[21] M.J. Eric, "Intermodulation Analysis of Non-linear Devices for Multiple-Carrier Inputs", CRC Report No. 1234, Communications Research Centre, Ottawa, November, 1972.

[22] C.L. Devieux and M.E. Jones, "A Practical Optimization Approach for QPSK/TDMA Satellite Channel Filtering", IEEE Trans. Comm., Vol. COM-29, No. 5, pp. 556-566, May 1981.

[23] R.W. Lucky, J. Salz, and E.J. Weldon, "Principles of Data Communication", McGraw-Hill, NY, 1968.

[24] G. Szentirami, "The Problem of Phase Equilization", IRE Trans. Circuit Theory, Vol. CT-6, pp. 272-277, September 1959.

[25] K.S. Hall, "Simple Series for Phase Angle, Delay and Group Delay", IEEE Trans. Circuits and Systems, Vol. CAS-26, No. 8, pp. 662-663, August 1979.

[26] A.S. Rosenbaum, "Binary PSK Error Probabilities with Multiple Cochannel Interference", IEEE Trans. Comm. Tech., Vol. COM-18, No. 3, pp. 241-253, June 1970.

[27] F.E. Glave and A.S. Rosenbaum, "An Upper Bound Analysis for Coherent Phase-Shift Keying with Cochannel, Adjacent-Channel and Intersymbol Interference, IEEE Trans. Comm., Vol. COM-23, No. 6, pp. 586-597, June 1975.

[28] J. Goldman, "Multiple Error Pelformance of PSK Systems with Cochannel Interference and Noise", IEEE Trans. Comm. Tech., Vol. COM-19, No. 4, pp. 420-430, August 1971.

[29] J.M. Aein and R.D. Turner, "Effect of Co-Channel Interference on CPSK Carriers", IEEE Trans. Comm., Vol. COM-21, No. 7, pp. 783-790, July 1973.

[30] J.J. Spilker, Jr., "Digital Communications by Satellite", Prentice-Hall, Inc., Englewood Cliffs, N.J., 1977.

[31] D.P. Taylor and C.H. Chan, "A Simulation Study of Two Bandwidth-Efficient Modulation Techniques", IEEE Trans. Comm., Vol. COM-29, No. 3, pp. 267-275, March 1981.

[32] R. deBuda, "Coherent Demodulation of Frequency-Shift Keying with Low Deviation Ratio", IEEE Trans. Comm., Vol. COM-20, No. 6, pp. 429-435, June 1972.

[33] S.A. Rhodes, "Effect of Noisy Phase Reference on Coherent Detection of Offset-QPSK Signals", IEEE Trans. Comm., Vol. COM-22, No. 8, pp. 1046-1055, August 1974.

[34] P.A. Wintz and E.J. Luecke, "Performance of Optimum and Suboptimum Synchronizers", IEEE Trans. Comm. Tech., Vol. COM-17, No. 3, pp. 380-389, June 1969.

[35] W.J. Hurd and T.O. Anderson, "Digital Transition Tracking Symbol Synchronizer for Low SNR Coded Systems", IEEE Trans. Comm. Tech., Vol. COM-18, No. 2, pp. 141-146, April 1970.

[36] M.K. Simon, "Nonlinear Analysis of an Absolute Value Type of an Early-Late Gate Bit Synchronizer", IEEE Trans. Comm. Tech., Vol. COM-18, No. 5, pp. 589-596, October 1970.

DATE DUE
DATE DE RETOUR

LOWE-MARTIN No. 1137

ΤΑ ΠΑΝΤΑ ΕΝ ΧΡΙΣΤΩΙ ΣΥΝΕΣΤΗΚΕΝ